Julius-Maximilians-
UNIVERSITÄT
WÜRZBURG

UNIVERSITÄT WÜRZBURG
PHYSIKALISCHES INSTITUT
epVI

Optical Accessible Spin Defects in Hexagonal Boron Nitride: Identification, Control and Application of the Negatively Charged Boron Vacancy V_B^-

Dissertation zur Erlangung des
naturwissenschaftlichen Doktorgrades
der Julius-Maximilians-Universität Würzburg

vorgelegt von

Andreas Paul Gottscholl

aus Schweinfurt

Würzburg 2021

Eingereicht am: 02.09.2021
bei der Fakultät für Physik und Astronomie

1. Gutachter: Prof. Dr. Vladimir Dyakonov
2. Gutachter: Prof. Dr. Sven Höfling
3. Gutachter: Prof. Dr. Christoph Becher
der Dissertation.

Vorsitzender: Prof. Dr. Giorgio Sangiovanni
1. Prüfer: Prof. Dr. Vladimir Dyakonov
2. Prüfer: Prof. Dr. Sven Höfling
3. Prüfer: Prof. Dr. Björn Trauzettel
im Promotionskolloquium.

Tag des Promotionskolloquiums: 04.05.2022

Doktorurkunde ausgehändigt am:

Contents

1 Introduction

"A scientist in his laboratory is not a mere technician:
he is also a child confronting natural phenomena that
impress him as though they were fairy tales."

Marie Curie, 1933

23rd October 2019, for the first time, the supremacy of a quantum computer over a classical system can be demonstrated. Based on 53 superconducting qubits, physicists from Google can solve a problem within 200 seconds, which would take 10000 years for a classical present-day supercomputer[1]. It is probably a matter of definition whether the moment of quantum superiority has really already taken place, since the solved problem was perfectly designed for the quantum computer and thus no universally usable device is yet available. However, the enormous progress in applied quantum physics in recent years is indisputable.

Besides superconducting qubits, spin-bearing color centers in solid state systems are of great interest for applied quantum physics[2,3]. These are less suitable for quantum computing due to the limited scalability, but more attractive for quantum communication, quantum memory and especially quantum sensing[4–7]. A major advantage over superconducting qubits and spin centers based on ion traps or quantum dots[8] are excellent coherence properties available at room temperature with comparably little effort. It has already been possible to demonstrate novel sensors that can probe magnetic fields or even spin-carrying nuclei in the environment on the nanometer scale[9]. For instance, local NMR measurements can be performed with single NV^- centers in diamond, providing insight into areas of biology, chemistry and medicine[10,11]. Furthermore, first quantum mechanical operations in the field of quantum information have already been demonstrated at room temperature[4]. In the long term assuming a better scalability, these could also offer an alternative to cryogenically cooled superconducting qubits, with the result that quantum computing may one day find its way into data analysis, quantum simulation and decryption at ambient temperatures. So far, though, such spin defects are known only in 3D materials, which limits their sensitivity to the environment. For example, the frontrunner NV^- in diamond currently possesses the best coherence properties in this field, but loses them if positioned too

close to the surface e.g. due to a graphitization of the diamond surface[12,13].
Another relevant field of solid state physics is dealing directly with surface effects, especially of single monolayers. 2D materials have gained increasing popularity in the last few years, spurred on by graphene[14]. Thus, a completely new field of solid state physics has been established within a very short time[15]. Monolayers of materials show partly completely unique properties. Bismuth and its physical properties, for example, have been widely understood for a long time. A single layer of bismuth on a SiC substrate, in contrast, promises features such as topological insulation to occur already at room temperature[16], which has only been a low-temperature phenomenon so far[17]. In addition, an indirect semiconductor such as MoS_2 exhibits different properties during the transition to a monolayer and turns into a direct semiconductor, thereby becoming an ideal candidate for nanometer-sized new electronic devices[18].
Besides many other novel features of individual 2D materials, the possibility of stacking them is a major focus of current research[15]. The compatibility of individual van der Waals materials permits the design of novel nanometer-sized devices. An example of such devices are transistors[19], consisting of only a few atomic layers based on van der Waals materials, which could supersede the existing silicon technology in the future. Furthermore, the stacking can not only be utilized for novel nanodevices, but also for the creation of metamaterials with tailor-made properties. Oriented on superconducting copper oxides, for example, newly stacked structures are conceivable, bringing the holy grail of room-temperature superconductivity one step closer[20].
In this work, a bridge was built between the so-far separate fields of spin defects and 2D systems: for the first time, an optically addressable spin defect (V_B^-) in a van der Waals material (hexagonal boron nitride) was identified and exploited. The results of this thesis are divided into three topics as follows:

1.) Identification of $\mathbf{V_B^-}$ (published in *Nature Materials*[21])
In the scope of this chapter, the defect - the negatively charged boron vacancy V_B^- - is identified and characterized. An initialization and readout of the spin state can be demonstrated optically at room temperature and its spin Hamiltonian contributions can be quantified.

2.) Coherent Control of $\mathbf{V_B^-}$ (published in *Science Advances*[22])
A coherent control is required for the defect to be utilized for quantum applications, which is demonstrated in this chapter at room temperature. Using this ability of coherent manipulation, it is possible to determine relevant relaxation times such as T_1, T_2, and T_2^*. Furthermore, phonon influences can be investigated by analysing the tem-

perature dependence of the spin relaxation rate and influences of the magnetic environment of surrounding nuclear spins are verified.

3.) Application of $\mathbf{V_B^-}$ as a Sensor (published in *Nature Communications*[23])
First applications of a V_B^--based sensor are demonstrated and discussed here. It is shown that a shift of the zero-field splitting parameter with temperature variations is attributed to changes of the lattice parameters. The same effect can also be induced and ultimately exploited by externally applying pressure to hBN. Thus, in combination with magnetic field-dependent Zeeman splitting, the defect can be used for temperature, pressure, and magnetic field sensing, which potentially enables atomic V_B^--based sensors at the nano-scale in the future.

2 Theory

In the following chapter, the theoretical background of the negatively charged boron vacancy is presented. Starting with the material system, theoretically predicted defects are then discussed in order to be able to better assign the later measurement results. Subsequently, the contributions of the spin Hamiltonian are discussed in order to provide a basis for the measurement routines presented later.

2.1 Defects in hexagonal Boron Nitride

2.1.1 Material System: hexagonal Boron Nitride

Hexagonal boron nitride (hBN) is a van der Waals (vdW) material which, as the name suggests, consists of boron and nitrogen atoms. These atoms are arranged alternately in a hexagonal lattice (see Figure 2.1). The honeycomb structure of a monolayer strongly resembles the one of graphene, which is why hBN is also known as white graphene [15]. However, the physical properties of these two materials differ significantly, which makes hBN a suitable complement to graphene.

Strong sigma bonds with $B1s$ and $N1s$ orbitals (bond energies of 190.4 eV and 398.0 eV, respectively [15,24]) are formed between the atoms of a layer. Between separate layers only weak van der Waals forces (81 meV for hBN bilayer [25]) are present, which allows easy exfoliation as in graphene [26] (see Figure 2.1b). hBN is an excellent insulator with its relatively large band gap of 6 eV [27]. The breakdown voltage is relatively high with 12 $MVcm^{-1}$ [28], which promises sufficient insulation even for a few layers [28]. In addition, hBN is transparent in the visible range (if non-treated/ unirradiated) [29] with a reflection index of $2-2.4$ [30]. This makes hBN an excellent encapsulation material [19,31–34].

Furthermore, hBN has only a low thermal expansion [35] and is stable up to temperatures of 2000 K [15]. Thermal conductivity, on the other hand, is relatively high and comparable to that of pure copper [15,36]. Moreover, hBN is a very elastic 2D material since it exhibits a large Young's modulus of about 270 Nm^{-1} [37] and it is mechanically highly robust, as it also possesses a high tensile strength of approximately 41 MPa [38].

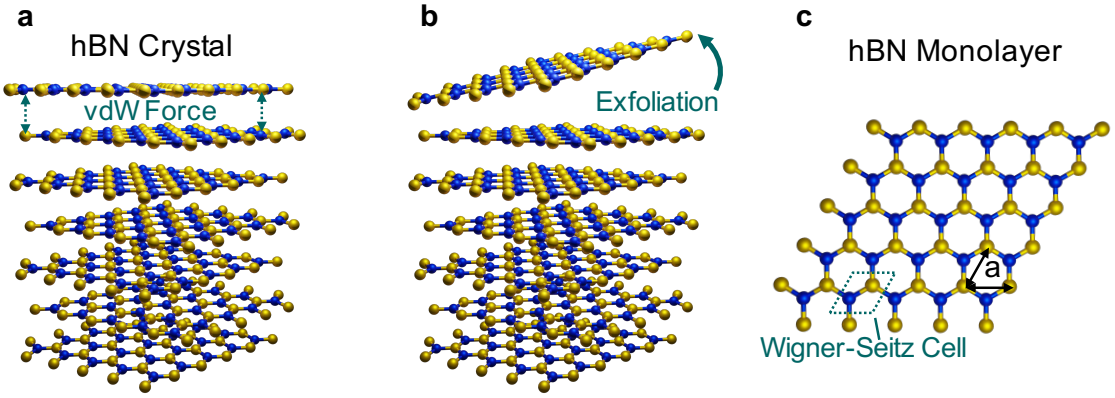

Figure 2.1: Structure of hexagonal Boron Nitride. a hBN Crystal with van der Waals (vdW) forces between the different layers. **b** Multi layered flakes and monolayers are obtained by exfoliation of a hBN crystal. **c** A hBN monolayer is depicted with its Wigner-Seitz cell revealing the periodic honeycomp structure.

The material can be present as a van der Waals crystal, but also single monolayers can be exfoliated and are stable under normal conditions, since no dangling bonds are present [15]. This 2D character of the material is also manifested in the phonon modes. Characteristic for hBN is the in-plane E_{2g} mode, which can be accessed in Raman measurements. In the bulk it is observed at 1366 cm^{-1} and for monolayers at 1370 cm^{-1} [39]. From a crystallographic point of view, hBN belongs to a large number of other 2D materials [40]. Especially the in-plane lattice parameters (a_{hBN} = 2.50 Å) of hBN are almost identical to those of graphene ($a_{graphene}$ = 2.46 Å) and close to MoS_2 (a_{MoS_2} = 3.16 Å) [35,41,42]. This allows a stacking of this class of materials, enabling completely novel devices based on these heterostructures. Particularly because of its aforementioned insulating properties, hBN is the standard material for the encapsulation of emerging 2D structures and is thus already well established. One example are field effect transisotrons consisting of the 2D materials graphene as a conductive gate electrode, molybdenum disulfide as semiconductor and the insulating hBN as dielectric [43].

2.1.2 Theoretically predicted Defects

Theoretically, a wide range of defects in hBN is envisioned: intrinsic vacancies or defects with impurities like oxygen, silicon, sulfur and carbon. Oxygen and carbon in particular can be easily incorporated in the lattice during the manufacturing process [44]. Silicon, on the other hand, is a suitable candidate, since silicon substrates are often

used in the annealing process of the sample and thus individual silicon atoms can diffuse into the hBN lattice[44].

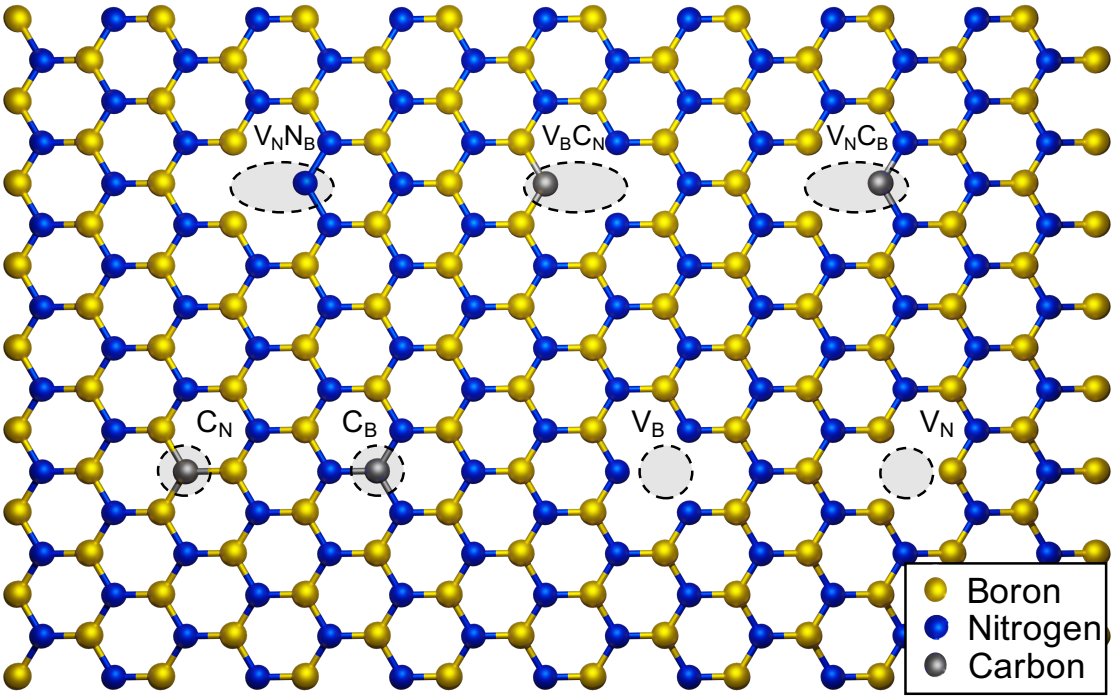

Figure 2.2: Selection of theoretically predicted defects in hBN. The upper defects are representative for antisite defects. The lower defects for atomic defects showing intrinsic defects (right) and with carbon incorporation (left).

A particular focus is on intrinsic and carbon-related defects, as these promise high stability[45]. A few are exemplarily shown in Figure 2.2. Antisite defects (upper half of Figure 2.2) such as V_NC_B and V_NN_B are of interest. These exhibit a C_{2v} symmetry. The V_NN_B is a representative antisite defect with a nitrogen substitution of a boron atom adjacent a nitrogen vacancy[46]. For this defect a non-trivial ground spin state is to be expected[45] - a feature which makes the defect attractive for quantum applications in 2D. Other potential antisite defects are a substitution by a foreign carbon atom in the immediate vicinity of a missing boron and nitrogen atom, respectively (see V_NC_B and V_BC_N). There is no direct evidence of these defects, however, the single photon emitter around 2 eV in hBN is associated with carbon related defects, for which the $V_BC_N^{(-)}$ is identified as a leading candidate. It is worth mentioning that during this work as part of a side project an ODMR signature was assigned to the carbon related defect. The results were published in *Nature Materials*[47], but are not part of this thesis.
More interesting for the scope of this work are the atomic defects, since these conform with their D_{3h} symmetry to the angle-dependent observations (see Chapter 5.4.3). V_N

and V_B could already be confirmed as stable by means of STEM [48]. It turned out that the boron vacancy is two orders of magnitude more common than the nitrogen vacancy. However, an assignment of a photoluminescence or even a spin state remained illusive until the start of this work. Simulations indicate a non-trivial spin state for V_B^- [45], which makes this defect interesting especially for applications in quantum information, communication and in the field of nanosensing [45]. Within the results of Chapter 5 published in *Nature Materials* [21] this non-trivial spin state was confirmed and the spin Hamiltonian of the defect was analyzed in more detail.
Following theoretical publications confirmed these parameters and pointed out that the spin density is localized in-plane on the surrounding nitrogen atoms. This raises the assumption that many of the effects observed in this thesis can also be transferred from the bulk to a monolayer. Theoretical calculations show, for example, that the calculated zero-field splitting value of $D_{bulk}/h = 3.467$ GHz shifts only slightly to higher values ($D_{monolayer}/h = 3.471$ GHz) when transitioning to a monolayer [49]. In addition, the relatively strong hyperfine coupling to the neighboring nitrogen atoms (47 MHz) can be corroborated for the bulk ($A_{bulk}/h = 47.2$ MHz) which, like the zero-field splitting parameter D, should not significantly differ for a monolayer ($A_{monolayer}/h = 47.9$ MHz) [49]. A detailed explanation of these parameters in general is presented in the following section.

2.2 Spin Hamiltonian

The spin Hamiltonian is used to describe a spin and its interaction with the environment (e.g. coupling to surrounding nuclei) by means of the Schrödinger equation [50,51]. This results in the eigenstates and their corresponding eigenenergies, which can later be addressed spectroscopically (in the case of this work by applying magnetic resonance). The spin Hamiltonian of the whole system considering all relevant influences can be formulated additively from the single contributions:

$$H = H_{eZ} + H_{ZFS} + H_{HFI} + H_{nZ} + H_{QI} \tag{2.1}$$

The individual contributions will now be discussed in detail [50–53].

2.2.1 Electron Zeeman Effect

Electrons can couple to an external magnetic field B_0 via their magnetic moment. The coupling is proportional to their angular momentum:

$$\vec{\mu} = \gamma \vec{S} \text{ with } \gamma = -g\mu_B/\hbar \tag{2.2}$$

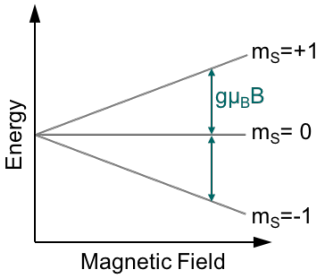

The proportionality constant g is approximately 2 (g = 2.00231930436256 for a free electron [54]). A significant deviation from 2 indicates a strongly localized electron while the g-factor shift reveals the influence of the spin-orbit interaction [55]. The spin Hamiltonian contribution based on the Zeeman effect is composed as follows:

$$H_{eZ} = g\mu_B \vec{B}\vec{S} \tag{2.3}$$

This results in the energy eigenvalues

$$E_{eZ}(m_S) = m_S g\mu_B B_0 \tag{2.4}$$

depending on the respective magnetic quantum number m_S of the corresponding state. For a spin S one obtains the spin quantum numbers $m_S = -S, -S+1, ..., S-1, S$. Thus, a spin 1/2 splits twice whereas a triplet ($S = 1$) splits into three (see illustration on the right).

2.2.2 Zero-Field Splitting

Besides the interaction with the external magnetic field, the electron spins for spin systems of higher order $S > 1/2$ can also interact with each other within their orbital[51]. This is called fine splitting or zero field splitting. It can be formulated as

$$H_{ZFS} = \vec{S}\mathbf{D}\vec{S} \tag{2.5}$$

Where **D** is considered to be a tensor in general. When multiplied out it leads to

$$H_{ZFS} = D_x S_x^2 + D_y S_y^2 + D_z S_z^2 \tag{2.6}$$

This can also be converted to the ZFS parameters D and E, which are more common in the literature.

$$H_{ZFS} = D\left(S_z^2 - S\frac{S+1}{3}\right) + E\left(S_x^2 - S_y^2\right) \tag{2.7}$$

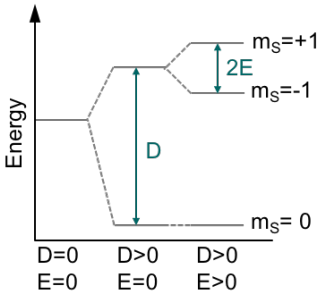

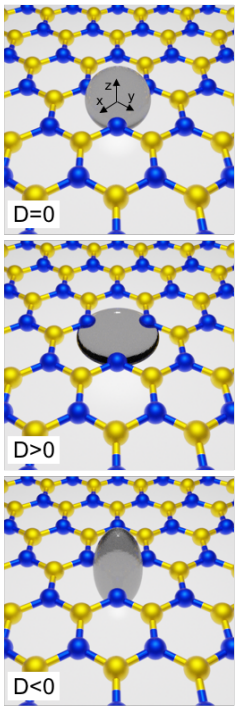

Here D is the axial contribution $D = 3/2 D_z$ and E is the rhombic or off-axial $E = 1/2(D_x - D_y)$. Taking the previous $S = 1$ example into account, the D value describes the splitting between $m_S = 0$ and $m_S = \pm 1$. The energy eigenvalues are given for this example by

$$E_{ZFS}(m_S) = D\left(m_S^2 - \frac{2}{3}\right), \tag{2.8}$$

thus the energy level is lifted by $1/3 D$ and lowered by $-2/3 D$, respectively. For the non-zero case of the off-axial contribution ($E \neq 0$) the $m_S = -1$ and $m_S = +1$ states are further splitted by $2E$(see left illustration).
For a description of the spin system, the axial contribution is often sufficient. The sign of the D value determines the electron distribution. For a D value of 0, an isotropic electron distribution ensues. An axial distribution results for a non-zero ZFS parameter. While a positive D value yields to an oblate distribution, a negative value results in a prolate one (cigar shape). The different electron distributions are shown schematically on the left).
Off-axial terms occur mainly for strains in materials

which lead to an asymmetry of the spin orbital [51]. The ZFS can range from a few GHz as in the well-known NV^- ($D_{NV^-} = 2.87$ GHz [3]) in diamond over a few MHz for V_{Si} ($D_{V_{Si}} = 70$ MHz [56] [57]) in SiC up to quasi zero (or not resolvable).

2.2.3 Hyperfine Interaction

Since nuclei can also carry a spin, it is possible that electron spins interact with the dipole moments of nuclear spins, depending on their localization.

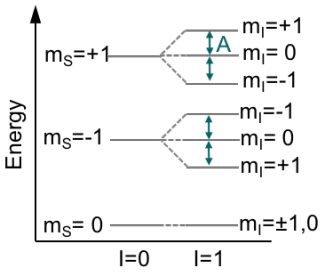

$$H_{HFI} = \sum_k \vec{S}\mathbf{A}\vec{I} \tag{2.9}$$

In many cases, it is sufficient to assume a scalar hyperfine constant instead of a hyperfine tensor. For n non-equivalent nuclei with the nuclear spin I one obtains $(2I+1)^n$ sublevels of the original energy level. For n equivalent spins the scheme simplifies to only $2nI+1$ sublevels [58]. In the right illustration an exemplary spin system with $S = 1$ and one $I = 1$ nucleus spin is shown (e.g. NV^- diamond). The sublevels are splitted by

$$E_{HFI}(m_S, m_I) = A m_S m_I. \tag{2.10}$$

2.2.4 Nuclear Zeeman Effect

As known from NMR, the nuclear spins also undergo a Zeeman effect similar to the electron spin, however, this effect is much smaller due to the smaller gyro magnetic ratio [59]. As soon as the nuclear spins of the system are coupled to the electron spins via hyperfine interaction, the nuclear Zeeman effect leads to a small shift/splitting of the signal.

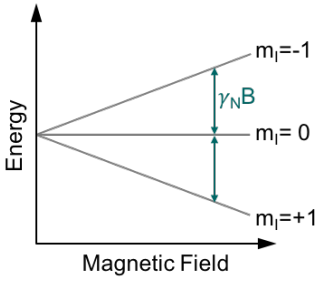

$$H_{nZ} = -\gamma_N \vec{B}\vec{I} \tag{2.11}$$

The corresponding energy scheme for a $I = 1$ is shown on the right. The energy levels are splitted, given by the corresponding eigenvalue

$$E_{nZ}(m_I) = -m_I \gamma B_0 \tag{2.12}$$

2.2.5 Quadrupole Splitting

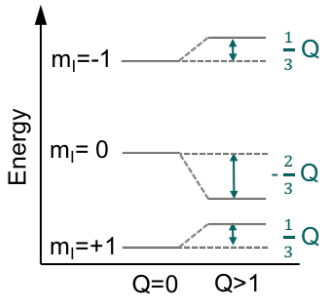

Another interaction specifically affecting the nuclei, and thus indirectly the electron spins, is nuclear quadrupole splitting. Nuclei with a nuclear spin of $I > 1/2$ exhibit an electric quadrupole moment. The mathematical structure is relatively similar to that of the ZFS of electron spins and can be formulated as follows:

$$H_{QI} = \vec{I}\mathbf{Q}\vec{I} \tag{2.13}$$

The eigenvalues for the previous example $I = 1$ (e.g. nitrogen) are derived by

$$E_{QI}(m_I) = Q\left(m_I^2 - \frac{2}{3}\right). \tag{2.14}$$

Therefore, the energy levels are lifted by $1/3Q$ and lowered by $-2/3Q$, respectively [60] (see illustration). In general, this value is also much smaller than the other contributions and is usually negligible for continuous wave measurements. An indirect addressing by means of ENDOR (electron nuclear double resonance) or ESEEM (electron spin echo envelope modulation) can resolve such a small contribution.

3 Method

The following chapter will focus on the used measuring techniques. Most of the observations and results of this thesis are based on optically detected magnetic resonance (ODMR), a further developed form of the established electron paramagnetic resonance (EPR). First, the basics of EPR will be discussed, subsequently followed by ODMR [51,52,58,61,62].

3.1 Electron Paramagnetic Resonance

In the preceding chapter the individual contributions of the spin Hamiltonian of an electron system were discussed. For small magnetic fields (e.g. $B_0 < 1$ T), the energy differences of the intrinsic energies of the aforementioned spin Hamiltonian parameters are in the order of μ eV, which is in the range of microwave photon energies. An optimal method for addressing such small energy differences is EPR. Its fundamental principle is a resonant absorption of incident microwaves, which matches the respective energy differences.
For the simplest case of a spin $S = 1/2$, which is exposed to a magnetic field B_0, the following resonance condition is obtained according to the selection rule $\Delta m_S = \pm 1$:

$$\Delta E = h\nu = g\mu_B B_0 \tag{3.1}$$

To satisfy the resonance condition, the external magnetic field and the incident microwave frequency must match accordingly. This can either be achieved by scanning the incident microwave frequency or by sweeping the external magnetic field. Usually, the latter is swept by driving a defined current through a Helmholtz coil pair. The frequency, on the other hand, is fixed, since reflection cavities are used by default in EPR to increase the sensitivity. The interaction of microwaves and spin system is increased, as far as the microwaves are equal to the resonance frequency of the cavity, which is given by its geometrical dimensions. If the external magnetic field is swept to tune the transition, microwave absorption can be observed for the resonant case.

Figure 3.1 illustrates the schematic configuration for cw EPR employed in this work as described elsewhere [51].

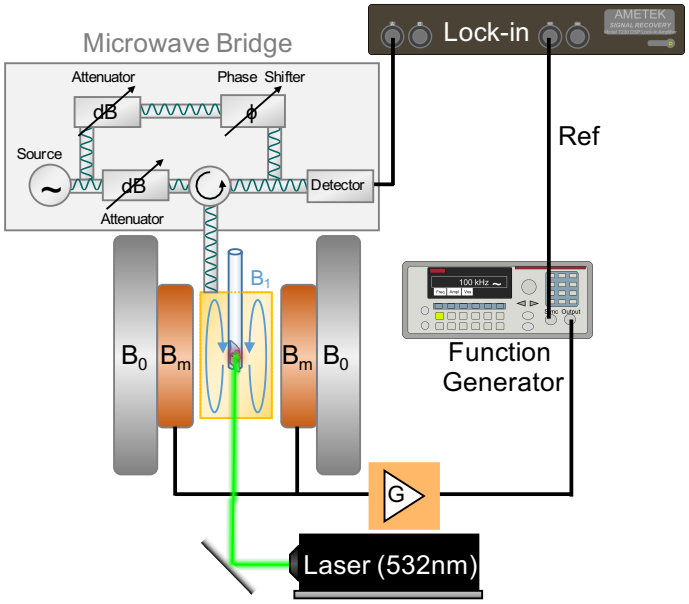

Figure 3.1: Continuous wave EPR setup. The sample is placed on a quartz rod inside a gold-coated microwave cavity (orange box). An external magnetic field B_0 with an additional modulation field B_m is applied via Helmholtz coil pairs. Microwaves are inserted and detected via a microwave bridge (gray box) and measured with a lock-in amplifier (see main text for further details). An optional laser can be inserted in order to spin polarize the sample.

The external magnetic field B_0 is applied via Helmholtz coils depicted in gray. Between the two coils is a gold-coated box resonator in whose center the sample is positioned via a quartz rod. Microwaves are injected and detected via a so-called microwave bridge (in this work from a Bruker spectrometer). It operates as follows: A microwave source emits microwaves matching the resonant frequency of the cavity. A part is outcoupled into the reference arm (upper part) and the rest remains in the signal arm. The power of the microwaves is adjusted by an adjustable attenuator and injected into the cavity via a circulator (B_1 field of microwaves outlined in blue). The reflected part of the microwaves travel through the circulator to the detector. If the cavity is critically coupled, no microwaves are reflected. However, as soon as the system is in resonance with the spin system, this critical coupling is disturbed and microwaves are reflected, which are registered by the detector. Depending on the design, the reference arm, in which the power and the phase of the microwaves can be adjusted separately, has a different function. In the present case, a Schottky diode is used, which generates a voltage proportional to the incoming microwave power. To ensure its proportionality, the re-

ference arm acts as a bias. In more recent models (e.g. Magnettech, see quantitative EPR measurements Figure 6.9), a mixer detection is used. In this case, the microwaves of the reference arm are used to down convert the actual signal.

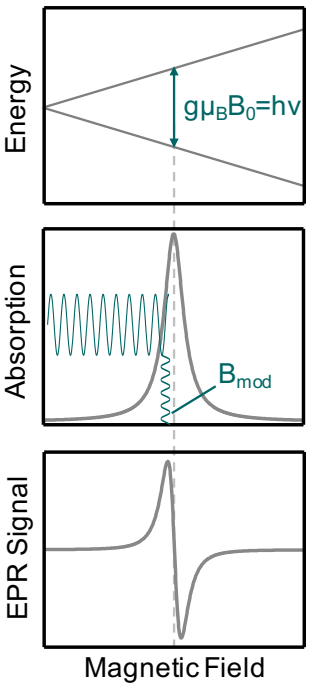

To increase the signal-to-noise ratio, a lock-in based detection is often chosen, where the magnetic field is additionally sinusoidally modulated. This is accomplished via an additional (small) pair of coils. The current is generated by a function generator (Keithley 3390) with the proper modulation frequency (usually 100 kHz to avoid $1/f$ noise) and amplified to the required power by an amplifier. The voltage proportional to the microwave power from the microwave bridge is fed to a lock-in amplifier (Signal Recovery 7230 lock-in amplifier) whose frequency is locked to the modulation frequency of the function generator. The resulting EPR signal is sketched in the margin: A $\Delta m_S = \pm 1$ transition leads to microwave absorption at the magnetic field corresponding to the resonance condition. The natural line width is given by a Lorentz profile and can be additionally broadened by Gaussians or a more complex structure (e.g. unresolved hyperfine splitting). Due to the modulated magnetic field, the lock-in detection results in a signal, which is proportional to the slope of the absorption peak at the different magnetic field positions. This yields to the first derivative of the microwave absorption signal. It should be noted that microwaves can only be absorbed if there is also a difference in the two energy levels involved. This is usually the case due to the Boltzmann statistics. At low temperatures, this difference is larger and therefore the EPR signal is typically larger as well. However, by using an externally coupled laser, the population difference can also be artificially manipulated to detect spin polarizations of electron spin states. This is realized in the present work with a 532-nm laser (Cobolt Samba 100). Dark measurements of EPR, on the other hand, have the advantage that in addition to providing insight into the spin Hamiltonian, they also provide quantitative information on the number of spins involved. They are proportional to the total microwave absorption (area under the absorption curve). This in turn is given by the double integral DI of the detected EPR signal. Summarizing, the double integral is proportional to the following influences [62]:

$$DI \propto \sqrt{P} B_m Q n_B S(S+1) n_S \tag{3.2}$$

with the microwave power P, the modulation amplitude B_m, the quality factor Q of the resonator, the Boltzman factor n_B, the total spin S and finally the number of involved spins n_S. Influences such as the spatial distribution of the microwave field are negligible for point samples which can be considered as the samples from the presented work. By comparing the DI of an EPR signal with the DI of a sample with a known spin number, the absolute spin number can be calculated, taking into account all measurement parameters. In this work, the material BDPA is used as a reference sample, since it has one radical with spin $S = 1/2$ per molecule (see later measurement Figure 6.9). The number of molecules and thus the number of EPR spin involved can therefore be derived from the amount of material.
Another general advantage of EPR (for both dark and illuminated measurements) is the possibility of performing angle resolved measurements. For this purpose, the sample is adjusted on a quartz rod (or fixed in an EPR tube) and rotated with a goniometer. Depending on the orientation of the sample in the external magnetic field, different projections of the B_0 field onto the defect axis can be studied. A disadvantage of EPR, however, are the limitations to large ensembles and only one frequency (the resonant frequency given by the resonator).

3.2 Optically Detected Magnetic Resonance

One of the best ways to study optically active spins is optically detected magnetic resonance or in short ODMR[51]. ODMR combines the optical properties of a system with its spin properties. For a mere characterization of the system, as with EPR, the cw mode is appropriate initially. Afterwards, the pulsed mode will be introduced, which gives insight into time-resolved processes and characteristic times such as T_1 and T_2.

3.2.1 Continuous Wave

The principle of ODMR will be exemplified by the following pumping scheme of an optically spin-polarizable triplet[63]. The system consists of a ground state triplet, an excited triplet and a metastable state. If the system is illuminated with a laser of sufficiently high energy, spin-preserving excitation of the spins to the excited state occurs. Subsequently, the system relaxes via two paths: either by emitting photons via photoluminescence or via intersystem crossing (ISC) using the metastable state. Assuming a spin-selective transition at ISC, spin polarization of the ground state ensues. If microwave photons of suitable energy are now inserted, transitions within the ground state (also possible for the excited state, although not relevant for this work) can be induced. A manipulation of this equilibrium manifests itself in an increase/decrease of the photoluminescence, as long as it differs in intensity depending on the spin state. The resulting difference depends on the investigated material system and can be enhanced by external influences such as low temperatures. Material systems such as NV^- diamond and SiC, for example, exhibit values in the range of 10 % and 0.1 %, respectively[64,65].

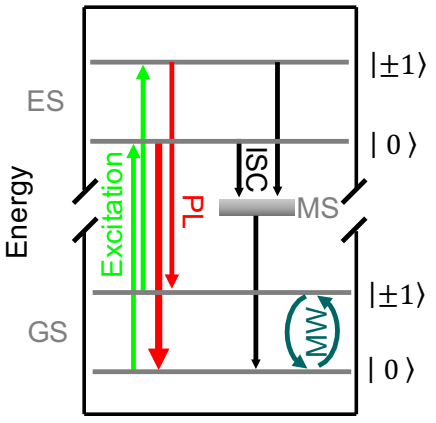

The quantity to be measured is therefore the change in photoluminescence. Analogous to EPR from the previous section, the magnetic field can be swept and the microwaves - now with higher power to achieve saturation - can be applied. Detection of the photoluminescence under optical excitation of the sample would already provide the ODMR signal. This is also called high field ODMR and is often used for larger ensembles (e.g. in organics).

A much more sophisticated approach is to use a confocal microscope, which allows the addressing of much smaller ensembles theoretically down to single emitters[10]. The setup for this is shown in Figure 3.2.

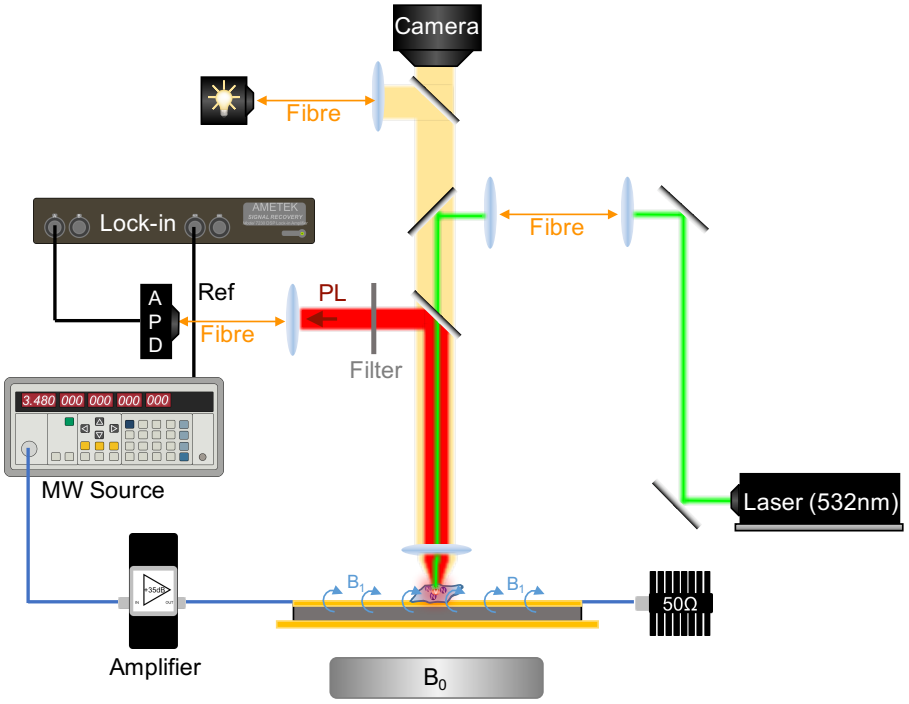

Figure 3.2: Confocal continuous wave ODMR setup. The sample is excited via a laser. The emitted Photoluminescence is detected by an APD and digitized by a lock-in. In order to induce transitions between spin levels a microwave is inserted through an amplifier into a stripline. The on/off modulation frequency is locked by the lock-in amplifier.

The upper part is the microscopic section of the setup, consisting of a white LED and a USB camera. With these it is possible to focus through a lens (Olympus: LMPLN10XIR, LMPLFLN50x and MPLN100x depending on the sample) on the sample lying on a microwave stripline. A 523-nm laser is used to excite the sample (Cobolt Samba 100 and Laser Quantum opus532 for power dependent measurements). The laser is coupled into the setup via multiple mirrors using a fiber that acts as a pinhole. The light is reflected by a dicroic mirror and focused on the sample. The PL of the sample is then separated from the excitation wavelength by a second dicroic mirror and reflected into the detection path. To block the remaining laser light and cut the correct PL band from the spectrum, several long-pass filters are also incorporated (532 nm and 700 nm. The avalanche photodiode (Thorlabs APD440A) is fiber-coupled to the setup and the voltage, which is proportional to the incident photons, is digitized with a lock-in (Signal Recovery 7230 lock-in amplifier). To induce transitions according to the above energy scheme, a microwave source (Stanford Research Systems SG384) is used to generate microwaves that are amplified to a sufficient power (Minicircuits ZVE-3W-83+) and passed through the stripline. The corresponding B_1 field is parallel to the surface at the center. The remaining microwave power is absorbed by a 50 Ω terminating resistor. The microwave source is on/off modulated for a S/N enhance-

ment to observe small changes in PL. The lock-in is tuned to the modulation frequency (677 Hz). In addition, a permanent magnet can be positioned below the stripline for an external magnetic field up to ≈ 20 mT. With this setup, it is possible to perform microwave frequency sweeps for arbitrary magnetic fields while tracking changes in photoluminescence.

3.2.2 Pulsed Mode

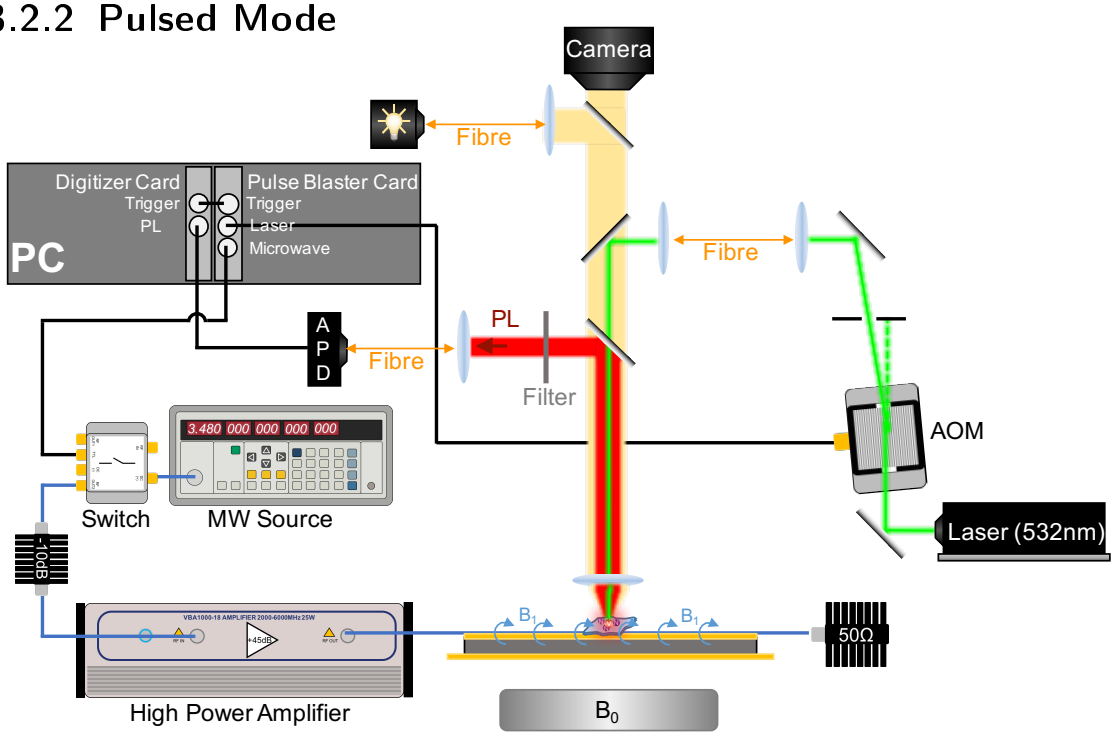

Figure 3.3: Confocal pulsed ODMR setup. The sample is excited via a laser pulsed by an AOM. The emitted photoluminescence is detected by an APD and digitized with a digitizer Card. In order to induce spin flips microwave pulses are created by a microwave switch and amplified by a high power amplifier. The whole measurement routine is controlled by a pulse blaster card, sending TTL pulses to the trigger of the digitizer card, the AOM for laser pulses and the microwave switch.

For quantum mechanical applications in general, the spin states must also be examined and comprehended in a time-resolved manner. Relevant times are T_1 and T_2, which have to be determined. The required pulse sequences are relatively similar to those used in NMR [66,67]. However, in order to apply such sequences, the setup has to be modified accordingly.

On the one hand the laser (Cobolt Samba 100) has to be pulsable, which in this case is provided by a TTL controllable acousto-optic modulator (AOM: AA.MT250-A0,2-VIS). On the other hand, the microwave source needs to be pulsable as well, which is accomplished by an external microwave switch (ZASWA-2-50DR+) that is also TTL controllable. To generate microwave pulses with a sufficiently high B_1 field, a high power

25 W MW amplifier (Vectawave VBA2060-25) is implemented. Finally, the detection is done with an APD (Thorlabs APD120A/M, Hamamatsu C10508-01, Hamamatsu MPPC C14455-3050A) with a higher bandwidth compared to cw ODMR. The output voltage is recorded with an oscilloscope (in this case a digitizer card built into the measuring PC). A controlled triggering of the single components with 2 ns accuracy is achieved by a Pulse Blaster card (PulseBlasterESR PRO 500 MHz), which is also integrated in the measuring PC.
The most important pulse sequences are discussed below.

Rabi-Oscillations

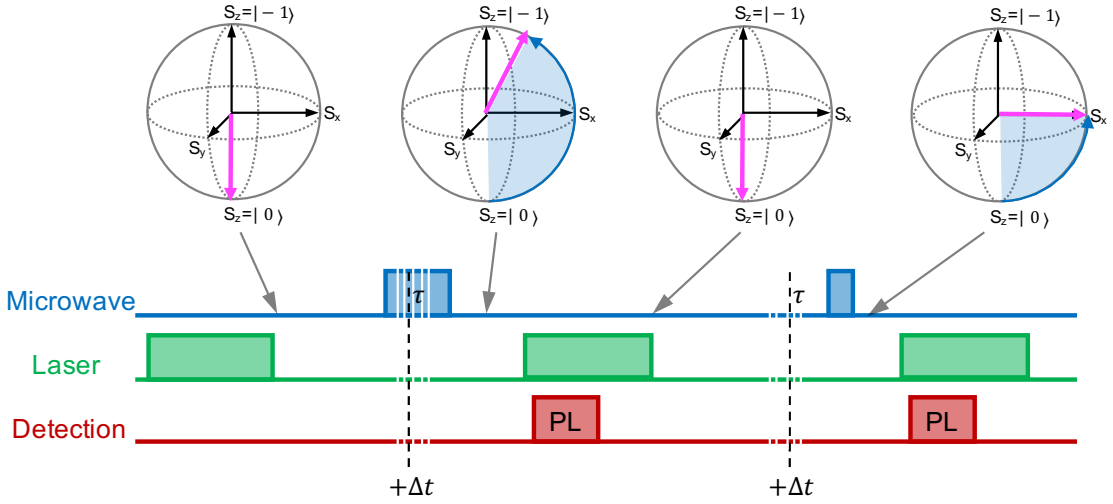

Figure 3.4: Pulse sequence for Rabi measurements. The current spin state during the pulse sequence is represented by a bloch sphere exemplary for the $|0\rangle \longleftrightarrow |-1\rangle$ transition. A laser pulse (green) is used for an initialization and read-out (red) of the spin state. Microwave pulses (blue) are used for flipping the angle of the spin on the Bloch sphere.

The fundament for all further pulse sequences is the demonstration of Rabi oscillations in order to accomplish a coherent control of the system. The coherent control is achieved in three steps, which will be introduced in the following using the example of Rabi measurements.

1) Initialization:
Initialization is accomplished by optical pumping via laser, polarizing the ground state as previously seen in cw ODMR. In the example shown here, the net magnetization is flipped to the $|0\rangle$ ($m_S = 0$) state, as illustrated by the Bloch sphere in Figure 3.4. Subsequently, the laser is switched off and the system remains in this state within the relevant relaxation times (see later described T_1 and T_2)

2) Manipulation:
Afterwards, the manipulation is performed by resonantly injected microwaves of variable length. The spin vector shown here in pink rotates on the Bloch sphere between $|0\rangle$ and $|-1\rangle$. Its rotating angle ϕ depends on the B_1 field but also on the length τ of the microwave pulse $\phi = 2\pi f_R(B_1)\tau$.

3) Read Out:
For read out, a second laser pulse is applied to the sample, measuring the photoluminescence immediately at the beginning, before the state is initialized.

The corresponding pulse sequence is shown in 3.4 with a Bloch sphere displaying the current spin state. Additionally to the theoretical steps 1-3, the measurement has to be repeated for a reference measurement. The reference pulse consists of an arbitrary but fixed length of a microwave pulse in order to exclude heating effects from the laser or unwanted oscillations from the AOM. On the one hand Rabi measurements are an evidence for a coherent controllable system, on the other hand, they are the calibration tool for defined microwave pulses and spin flips on the Bloch sphere in order to perform more complex measurement routines.

Spin-Lattice Relaxation T_1

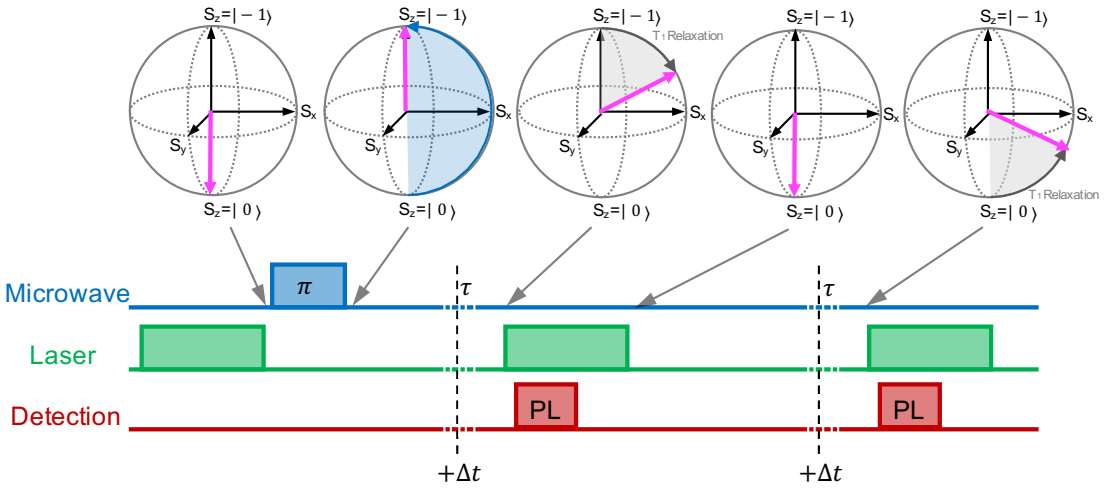

Figure 3.5: Pulse sequence for spin-lattice relaxation measurements. A Bloch sphere represents the current spin state for the $|0\rangle \longleftrightarrow |-1\rangle$ transition. A laser pulse (green) is used for an initialization and read-out (red) of the spin state. Microwave $\pi-$pulses (blue) are used for a controlled change into the $|-1\rangle$ state. The temporal evolution into the thermal equilibrium corresponds to the T_1 time.

One of the most important spin parameters is the spin-lattice relaxation time T_1 which is an upper limit for the spin coherence time. The spin lattice relaxation time

T_1 describes the time required for a state to relax to thermal equilibrium [51].
A simple excitation of the spin system with an additional read-out after a specific time would be sufficient to determine the T_1 time. However, in order to exclude other decays due to heating, again, a reference pulse method is chosen as depicted in 3.5.
First, the system is initialized into the $|0\rangle$ state. In the first half of the sequence the system is flipped by a π-pulse into the $|-1\rangle$ state, where a relaxation of the net magnetization occurs back into the thermal equilibrium. The current spin state is mapped after different times τ which is increased by an increment of Δt after each repetition. In the second half the system is initialized and relaxes directly back into the equilibrium. The decay of the difference of both measurements reveals the spin lattice relaxation time T_1 of the system.

Spin-Spin Relaxation T_2

Especially for quantum application, the spin-spin relaxation is the limiting time scale on which quantum operations can be performed. It describes the coherent properties of the investigated system. The pulse protocol is based on the well-known Hahn-Echo sequence which is one of the standard sequences in NMR. The adapted pulse scheme for pulsed ODMR is shown in Figure 3.6 [67].
Identically to the other pulsed measurements, the system is first initialized into the $|0\rangle$ state with a laser pulse. Afterwards, a $\pi/2$-pulse flips the spins into the transversal plane. Here, the spins are dephasing with their individual precession during a waiting time $\tau/2$. To reduce this influence a π-pulse is applied, which refocuses the spins. The remaining contribution is flipped back after $\tau/2$ into the $|0\rangle$ state by a $\pi/2$-pulse. The reference pulse scheme is identically except that the refocused spins are projected into the $|-1\rangle$ state by a $3\pi/2$-pulse. A variation of the increment Δt results in a sampling of the temporal coherence of the system, revealing the coherence time T_2.

3.2.3 Multifrequency ODMR

Another powerful ODMR-related measurement technique is the so-called hole burning spectroscopy [68–71]. This multifrequency magnetic resonance method is actually inspired by optical spectroscopy, where two lasers of different wavelengths are used. The first laser is typically taken as a conventional probe, whereas the second "pump laser" is applied to saturate transitions. For optically detected magnetic resonance, this effect has already been demonstrated and exploited for both NV in diamond and V_{Si} in SiC. It is suggestive to apply this measurement method also to a comparable system - like the color centers in hBN considered in this work (see Chapter 6.5). In the following, the

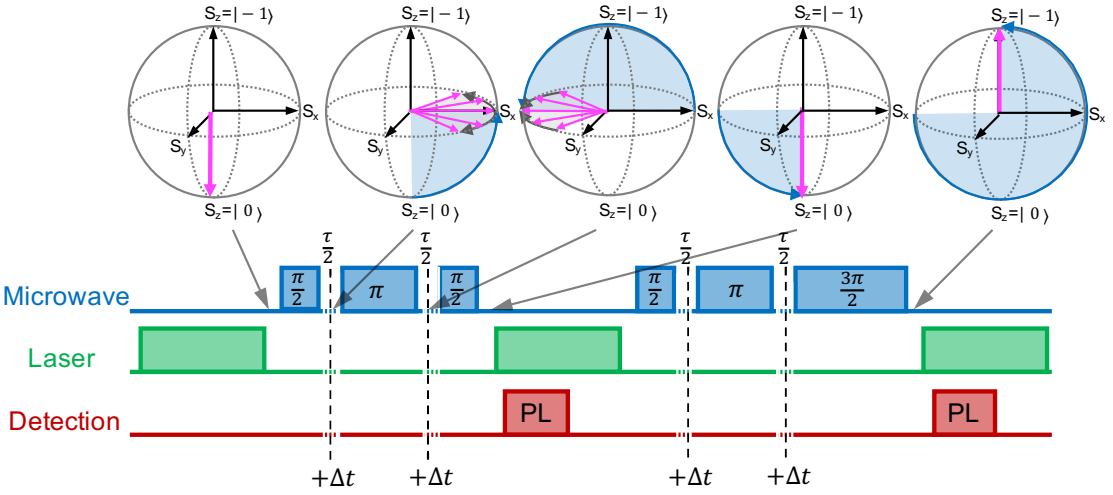

Figure 3.6: Pulse sequence for spin-spin relaxation measurements. A Bloch sphere represents the current spin state for the $|0\rangle \longleftrightarrow |-1\rangle$ transition. A laser pulse (green) is used for an initialization and read-out (red) of the spin state. A $\pi/2-$microwave-pulse (blue) flips the initialized state into the transversal plane where a dephasing occurs. A $\pi-$pulse refocuses the spins and an additional $\pi/2-(3\pi/2-)$pulse is used for flipping the spins further into a well-defined spin state in order to enable a read-out.

observable effects of this technique will be briefly addressed:
Hole burning spectroscopy is a sophisticated technique to explore the structure of broadened spectra in more detail. A magnetic resonance spectrum e.g. an ODMR spectrum can be homogeneously but also inhomogeneously broadened. The fundamental mechanism for the individual material system is often unclear, which corresponds, for example, to a broad Gaussian without structure (see Figure 3.7a). If the system is inhomogeneously broadened, the whole peak consists of a superposition of single narrower spectra. In cw ODMR only the broad peak would be detectable, with the multi-frequency method of hole burning, however, also the substructures can be dissolved as follows. By applying a second frequency suitable for the sub-transition, it can be saturated at sufficient power, preventing it from contributing to the conventional ODMR spectrum. This manifests itself in a decrease of the ODMR amplitude at the irradiated resonance frequency which finally yields a hole (gray). A cw ODMR spectrum (swept frequency modulated as normal on/off) with a continuously irradiated central hole frequency is illustrated in Figure 3.7b. This is often sufficient as evidence for an indication for inhomogeneous broadening[72]. To obtain the actual hole spectrum, the signal can be subtracted from the original cw ODMR spectrum or - much more efficiently - extracted directly via an appropriate modulation (see Figure 3.7).

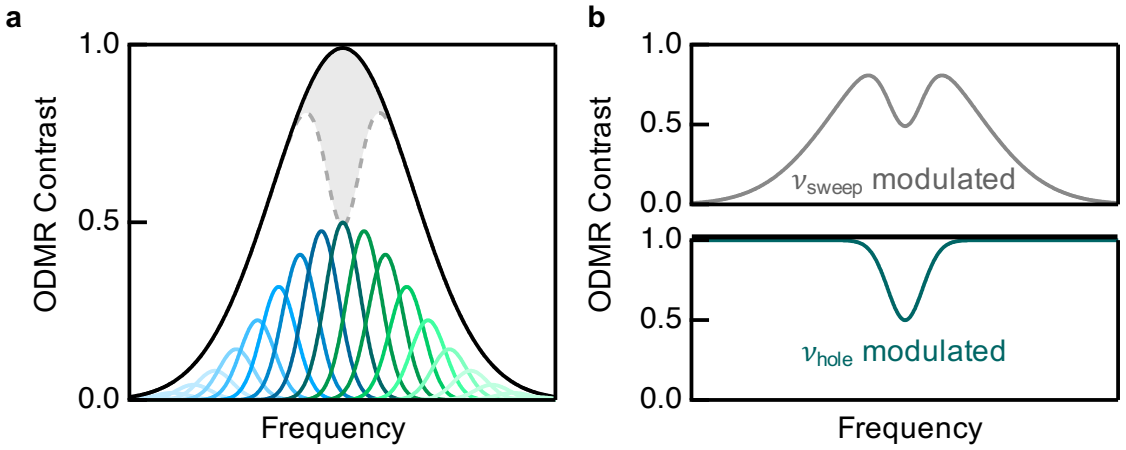

Figure 3.7: Principle of hole burning. **a** Inhomogeneous broadened spectrum (black) consisting of different contributions (coloured gaussian curves). In hole burning spectroscopy a second frequency saturates one of the sub-transitions resulting in the gray curve (saturation of the center transition). **b** Types of hole burning measurements: In the top panel the swept frequency is modulated, whereas the hole frequency in inserted continuously. In the bottom panel the hole frequency is modulated resulting in the pristine hole spectrum.

If the hole frequency is modulated on/off, a probe is located at the peak which is expressed in the value of the ODMR contrast (in this case continuously 1). When sweeping the continuously injected frequency, a sweeping of the conventional spectrum occurs. If the frequency approaches the modulated hole, the ODMR signal collapses and the signal corresponds directly to the pristine hole spectrum.
For a realization of this measurement method the same setup as for cw ODMR is used. In addition, a second microwave source (Stanford Research Systems SG384) is coupled using a microwave combiner (Minicircuits ZFRSC-183-S+). Depending on the choice of modulation (or swept microwave source), both measurement modes from Figure 3.7 can be employed.

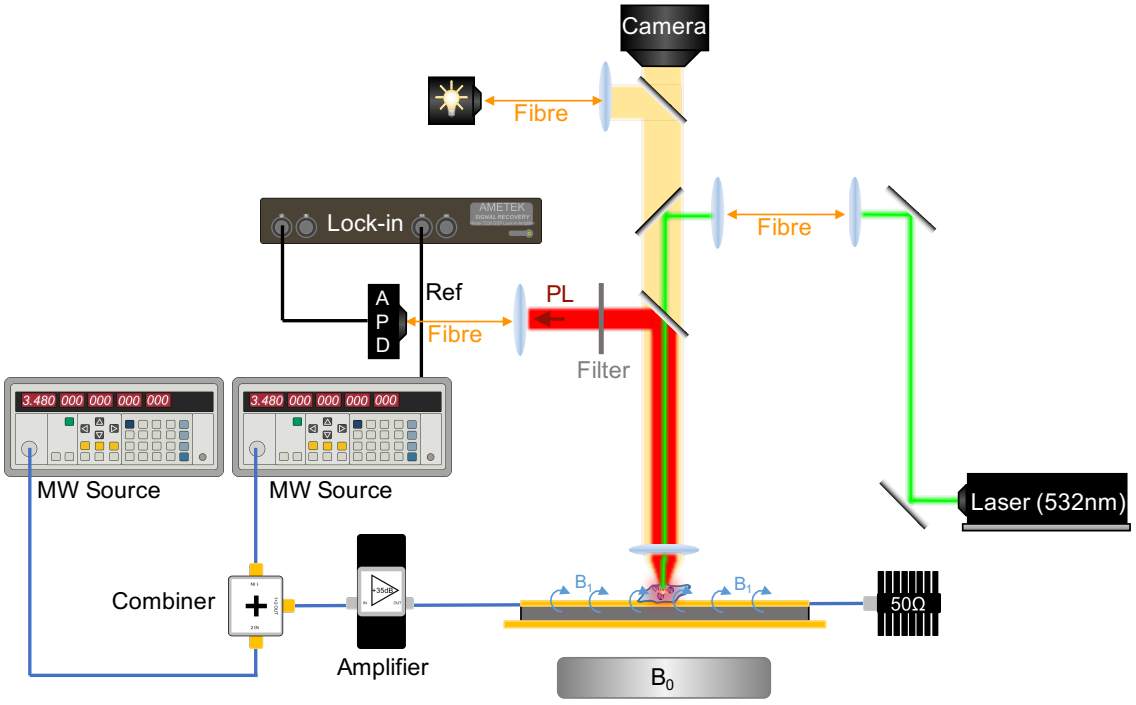

Figure 3.8: Multifrequency ODMR setup. A second microwave source is added to the previously shown cw ODMR setup. The microwave sources are connected via a combiner and can be addressed individually.

4 Sample

Hexagonal boron nitride is a commercial material and, like other 2D Materials, can be obtained from companies such as HQ Graphene and Graphene Supermarket, respectively[73,74]. At the beginning of this thesis, it was unknown how to create the investigated defects the best way. In the meantime there are a lot of publications about generating the vacancies via neutrons, electrons, protons, different ions and femtosecond laser pulses[75–78]. Figure 4.1 shows an overview of the three samples types investigated in the work: an hBN single crystal, ultrafine hBN powder and multi-layered hBN flakes.

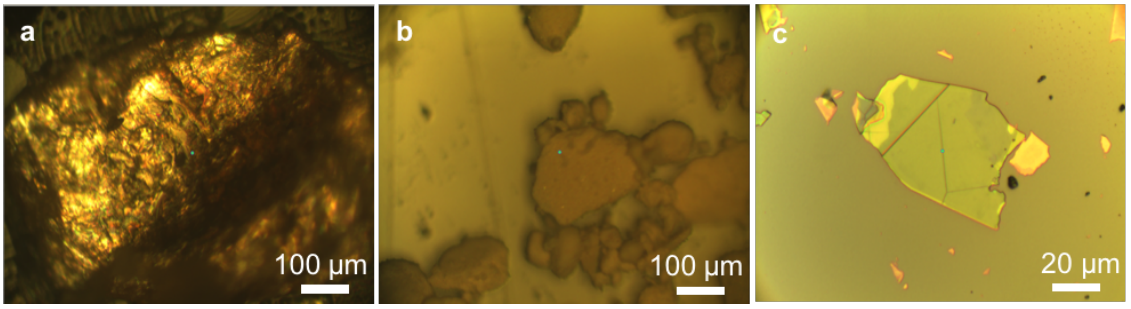

Figure 4.1: Overview of the samples used in this thesis. **a** Neutron irradiated single crystal of hBN. **b** Ultrafine hBN powder of randomly oriented flakes. **c** Ion irradiated flakes.

4.1 Single Crystal of hexagonal Boron Nitride

Most of the results here are based on an hBN single crystal. The single crystal is purchased from the company HQ Graphene, which synthetically fabricated monocrystalline hexagonal boron nitride to comparatively large crystals[73]. The thickness is about 60 μm and the diameter was initially about 1 mm. As the work progressed, the sample decreased in size due to normal wear, but also due to W-Band EPR measurements where the maximum sample volume is severely limited due to the short wavelength. In the last chapter, where the surface area is of significant importance (see Chapter 7.3), the contact area was approximately 0.24 mm^2.

The defects studied in this work were created by neutron irradiation. This was realized in the brazilian nuclear reactor Triga Mark I IPR-R1 of the Nuclear Technology Development Center (CDTN). The neutron flux was about $4 \cdot 10^{12}$ n cm^{-2}s^{-1} resulting

in an integrated dose of $2.3 \cdot 10^{18}$ n cm^{-2}. The sample was encapsulated in cadmium in order to block thermal neutrons whereas higher energetic neutrons penetrate the sample.

4.2 Powder of hexagonal Boron Nitride Flakes

A second sample is a commercial ultrafine hBN powder consisting of randomly oriented flakes with a size of about 70 nm[74]. The sample was acquired from Graphene Supermarket. The defects were created identically with neutron irradiation with the same flux etc. Since the flakes are randomly oriented and therefore the spin defects, they are not the best choice for a precise analysis of spin Hamiltonian contributions. However, the volume is larger than for the crystal which makes it ideal for large ensemble measurements e.g. high-field ODMR (see later Figure 5.4).

4.3 Oriented hexagonal Boron Nitride Flakes

The third sample type are thin multilayered hBN flakes on Si_2/Al_2O_3 substrates. The exfoliated flakes are purchased by HQ Graphene with a size below 100 μm. The spin defects were created by different ion irradiations (lithium, gallium) in order to reveal the intrinsic nature of the investigated defects (see Section 5.9 for further details).

5 Identification of Spin Defects in hexagonal Boron Nitride

ABSTRACT: Optically addressable spins in wide-bandgap semiconductors are a promising platform for exploring quantum phenomena. While colour centres in three-dimensional crystals such as diamond and silicon carbide were studied in detail, they were not observed experimentally in two-dimensional (2D) materials. In this chapter, spin-dependent processes in the 2D material hexagonal boron nitride (hBN) are reported. Fluorescence lines are identified associated with a particular defect, the negatively charged boron vacancy (V_B^-), showing a triplet ($S = 1$) ground state and zero-field splitting of ~ 3.5 GHz. Furthermore, a coupling of the spin defect to its surrounding nitrogen atoms resulting in a hyperfine splitting of $A = 47$ MHz is observed. This centre exhibits optically detected magnetic resonance at room temperature and a spin polarization under optical pumping, which leads to optically induced population inversion of the spin ground state - a prerequisite for coherent spin-mainpulation schemes. These results constitute a step forward in establishing 2D hBN as a prime platform for scalable quantum technologies, with potential for spin-based quantum information and sensing application.

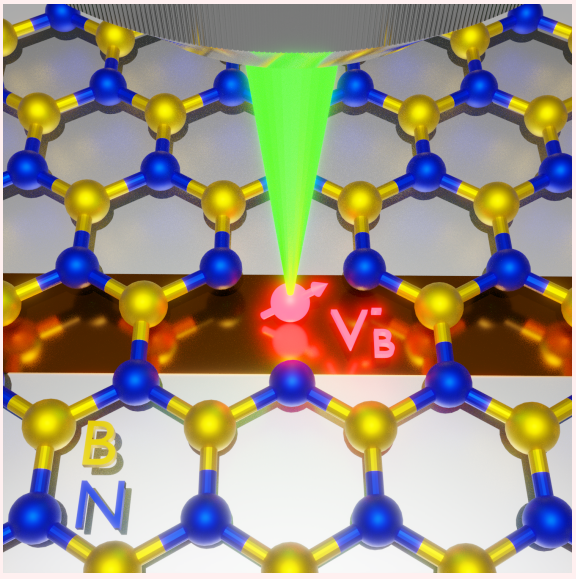

This chapter is based on A. Gottscholl et al. "Initialization and read-out of intrinsic spin defects in a van der Waals crystal at room temperature", *Nature Materials*, **19** 540-545 (2020) [21].

5.1 Introduction

The emergence of two-dimensional (2D) materials and van der Waals crystals has enabled the observation and realization of unique optoelectronic and nanophotonic effects, such as Moiré excitons and quantum spin Hall effect at elevated temperatures, to name a few[79,80]. Amidst the large variety of van der Waals crystals studied, hBN offers a combination of unique physical, chemical and optical properties[81]. Most relevant to this work is the ability of hBN to host atomic impurities (or point defects), which give rise to quantized optical transitions that are well below its bandgap[82,83]. hBN colour centres are ultrabright with narrow and tuneable linewidth[84–86], and photostability up to 800 K[87]. Whilst the nature of many of the defects is still uncertain[44,45,88–91], they are being extensively studied as promising candidates for quantum photonic applications requiring on-demand, ultrabright single-photon emission.

A step forward, which will significantly extend the functionality of hBN emitters for quantum applications, is to interface their optical properties with spin transitions, and realize spin polarization and optical spin readout schemes[92,93]. The concept of the spin-photon interface has been extensively studied in quantum dots[94] and the nitrogen vacancy centre in diamond[95]. The latter has been harnessed to realize basic two-node quantum networks[95] and a plethora of advanced quantum-sensing schemes[10,96,97]. The basic principle is that the high-spin ground or excited state of the defect can be polarized, manipulated and read out optically owing to the spin-dependent excitation, decay and intersystem crossing pathways available to the system during the optical excitation–recombination cycle[98].

Yet, extending the optical control of single-spin states beyond defects in three-dimensional (3D) crystals to those in 2D systems has remained elusive. If achieved, it will open up a range of possibilities both fundamental and technological. The two-dimensional nature of these materials inherently allows for seamless integration with heterogeneous, optoelectronic devices where the hosted solidstate qubits can be readily interfaced with cavities, resonators and nanophotonic components from foreign materials. Further, it naturally grants nanoscale proximity of the spin probe to target samples for high-resolution quantum-sensing realizations. Reliable and deterministic transfer of hBN layers on stacks of other 2D materials is well established and is part of one of the most relevant endeavours of condensed matter physics at present—engineering heterostructures made with purposefully chosen sequences of atomically thin 2D materials[40].

5.2 Photoluminescence of the Defect

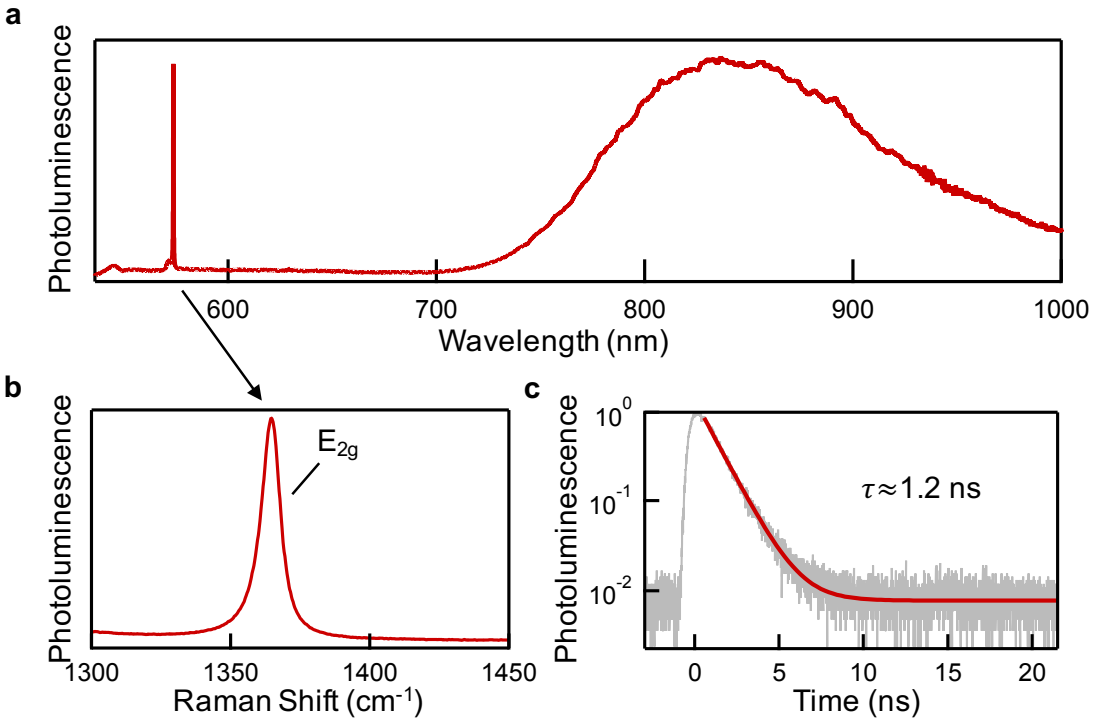

Figure 5.1: Photoluminescence of an hBN single crystal at room temperature, T = 300 K. **a** Photoluminescence spectrum of the sample at room temperature displaying a sharp Raman peak at 574 nm and a pronounced emission at 850 nm. **b** Zoom of the Raman peak plotted over inverse centimeters. The peak is located at 1364 cm^{-1} and corresponds to the in-plane E_{2g} mode. **c** Transient photoluminescence data (gray) revealing an excited-state lifetime of $\tau = 1.2$ ns.
(Transient measurement provided by I. Aharonovich, M. Kianinia, C. Bradac and M. Toth)

Most of the investigated quantum emitters in hexagonal boron nitride are emitting around 2 eV (≈ 620 nm) [83–86,88]. The samples which are studied in this work reveal a broad emission around $\lambda_{max} \approx 850$ nm under $\lambda_{exc} = 532$ nm laser excitation after irradiation with e.g. neutrons (see Chapter 4). The corresponding photoluminescence (PL) spectrum of a neutron irradiated single crystal of hBN is shown in Figure 5.1a. Besides the dominating PL band in the near infrared a sharp peak is located around $\lambda_{Raman} \approx 574$ nm which can be addressed to the Raman scattering process of the hBN lattice. Figure 5.1b depicts a detailed zoom of the peak plotted over cm^{-1} to reveal the Raman shift position. The peak is located at 1364 cm^{-1} and coincides well with the expected in-plane E_{2g} mode [39], which confirms the 2D properties of the van der Waals system and the quality of the hBN single crystal. While the sharp peak can be attributed to scattering processes of incident light with the lattice, the PL created by neutron irradiation can be explained by defects laying inside the wide bandgap of 6 eV [27]. Their excited-state lifetime can be determined to $\tau_{exc} = 1.2$ ns by time resolved PL measure-

ments presented in Figure 5.1c. Most interestingly, the PL which is found from this hBN colour centre is spin dependent.

5.3 Spin read-out via Optically Detected Magnetic Resonance

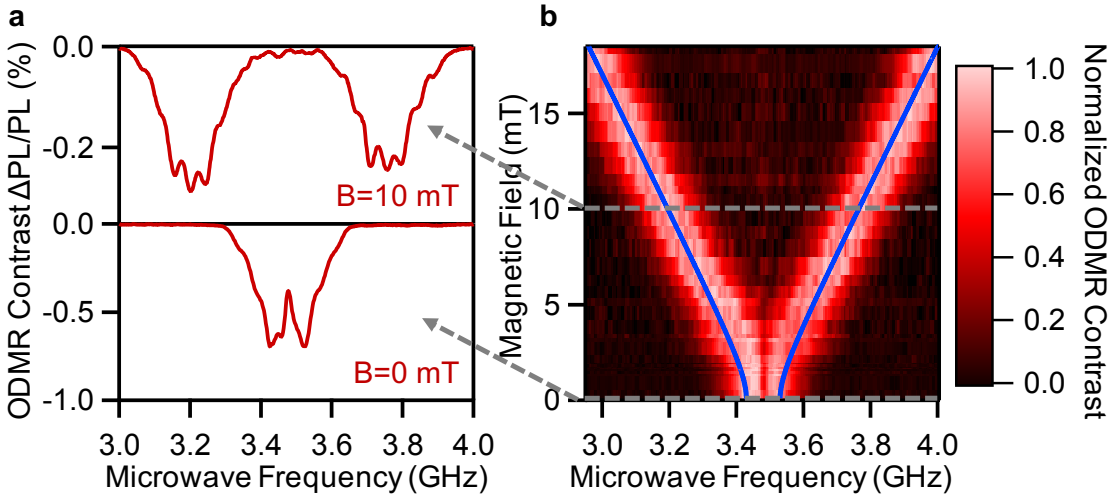

Figure 5.2: ODMR of an hBN single crystal at room temperature, T = 300 K. **a** ODMR spectra measured at zero magnetic field (bottom) and at magnetic field B = 10 mT (top) with the corresponding ODMR frequencies ν_0, ν_1 and ν_2, respectively. **b** Dependence of ODMR frequencies on the magnetic field ($\vec{B} \parallel \vec{c}$). Experimental data (red) and fit (blue line) obtained using Equation 5.1 with parameters D/h = 3.48 GHz, E/h = 50 MHz and g = 2.000. The gray dashed lines represent the positions of the left ODMR spectra.

Figure 5.2 shows the ODMR spectrum recorded for an hBN single crystal at T = 300 K. As described in Chapter 5.3, in ODMR experiments, microwave-induced magnetic dipole transitions between spin sublevels manifest as changes in PL intensity (ΔPL). The prerequisite for optical (PL) detection of EPR is thus the existence of a dependence between the optical excitation–recombination cycle and the spin orientation of the defect. Figure 5.2a shows the spectrum of the investigated sample as normalised change of PL intensity (ΔPL/PL) -that is, ODMR contrast- as a function of the applied microwave frequency ν for two static magnetic fields, B = 0 and B = 10 mT. Even without an external magnetic field, the ODMR spectrum shows two distinct resonances, ν_1 and ν_2, located symmetrically around the frequency ν_0. These are tentatively assigned to the $\Delta m_S = \pm 1$ spin transitions between triplet energy sublevels with completely lifted threefold degeneracy, due to a splitting induced by dipolar interaction between the unpaired electron spins, forming the triplet. This so-called zero-field splitting is described by parameters D and E (see Chapter 2.2.2), which can be derived

from the spectrum as $^{D}/_{h} = \nu_0$ and $\nu_{1,2} = {}^{(D\pm E)}/_{h}$, with h being Planck's constant, to express the interaction energies in frequency units. To verify this assignment, the dependence of the ν_1 and ν_2 resonant microwave frequencies on the magnitude of the external static magnetic field is studied.

The evolution of the ODMR spectrum with the field applied parallel to the hexagonal $\vec{c}$ axis ($\vec{B} \parallel \vec{c}$) of hBN is presented in Figure 5.2b. To explain the observed transitions and their variation with magnetic field, the standard spin Hamiltonian given by equation 5.1 is used, with $\vec{z}$ as the principle symmetry axis oriented perpendicular to the plane (collinear with the c axis of the hBN crystal).

$$H = D\left(S_z^2 - S\frac{(S+1)}{3}\right) + E\left(S_x^2 - S_y^2\right) + g\mu_B\vec{B}\vec{S} \tag{5.1}$$

where D and E are the ZFS parameters, $\vec{S}$ is the total electron spin ($S = 1$ for triplets), g is the Landé factor, μ_B is the Bohr magneton, $\vec{B}$ is the static magnetic field and $S_{x,y,z}$ are the spin-1 operators. According to Equation 5.1, and for $\vec{B}$ applied parallel to the $\vec{c}$ axis, the resonant microwave frequencies at which the transitions occur vary as

$$\nu_{1,2} = \nu_0 \pm \frac{1}{h}\sqrt{E^2 + \left(g\mu_B B\right)^2} \tag{5.2}$$

where $\nu_0 = {}^{D}/_{h}$. The dependence of ODMR frequencies ν_1 and ν_2 on the magnetic field shown in Figure 5.2b can be perfectly fitted by Equation 5.2 with $g = 2.000$, ${}^{D}/_{h} = 3.48$ GHz and a small off-axial component of the ZFS ${}^{E}/_{h} = 50$ MHz. This demonstrates a highly symmetrical, almost uniaxial, defect structure.

5.4 Spin Hamiltonian analysis via Electron Paramagnetic Resonance

So far, it was shown that the investigated hBN defect is an $S = 1$ system, which can be optically addressed and read out using ODMR. From the ODMR measurements alone, however, it is difficult to conclude whether the defect is in an excited, metastable or ground state. It is essential to know this so as to determine the correct spin-dependent recombination pathway. Notable is that earlier results[99] proposed a defect in hBN with a singlet ground state to possess a spin-triplet metastable state. However, from the EPR results presented below, it becomes clear that another defect is investigated here. A second consideration is that zero-field ODMR measurements alone are not sufficient to deduce the microscopic structure of the defect. To address these points, highfield ODMR is applied on previously studied exfoliated hBN flakes[100] (see Chapter 5.5, as well as highfield EPR to the hBN single crystal as studied by ODMR shown in Figure 5.2. It is also notable that defects in hBN single crystals and in the hBN exfoliated flakes were introduced in the same way (see Chapter 4), and the PL emission at 800 nm and ODMR signal are only seen after implantation/neutron irradiation. These defects (which may be present) were not optically active in pristine samples.

5.4.1 Spin polarization of a Triplet State

Figure 5.3 shows X-band EPR spectra taken at a fixed microwave frequency ($\nu = 9.4$ GHz) while scanning the static magnetic field aligned parallel to the c axis of the crystal ($\vec{B} \parallel \vec{c}$). Due to the amplitude modulation of the B field, EPR spectra look like first derivatives of the absorption signals (see Chapter 3.1). The spectra are recorded with (green trace) and without (black trace) optical excitation and consist of two groups of signals originating from two different types of paramagnetic species. The first group (centred at $B \approx 330$ mT) is characterized by $g = 2.003$ and consists of three EPR lines of nearly equal intensities corresponding to a paramagnetic centre with electron spin $S = 1/2$ interacting with a nuclear spin $I = 1$ (see Figure 5.3c for a detailed zoom of the relevant range). The origin of such a splitting is hyperfine interaction. This group of lines remains the same with and without optical excitation and is not observe in ODMR under the same conditions (see Figure 5.4).

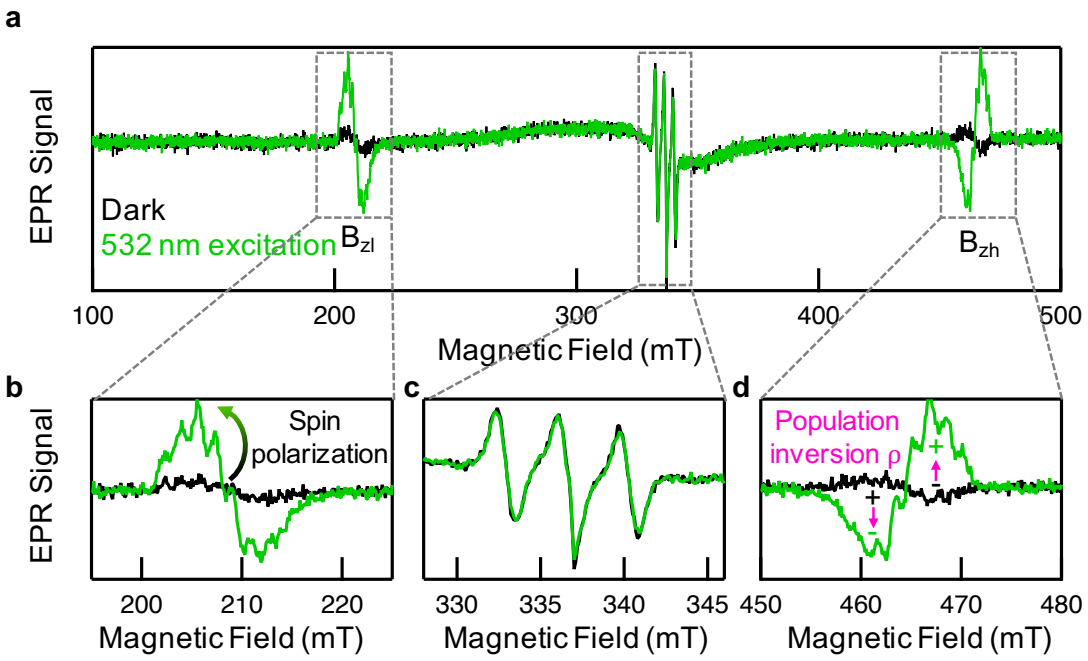

Figure 5.3: X-band EPR studies of the V_B^- centre in the hBN single crystal at T = 5 K. **a** Spectra measured with (green trace) and without (black trace) 532-nm optical excitation in the magnetic field orientation $\theta = 0°$ ($\vec{B} \parallel \vec{c}$). Doublet lines associated with the $S = 1$ centre with splitting of $\Delta B \approx 260$ mT (equivalent to ${}^{2D}/_{h} \approx 2 \cdot 3.6$ GHz are labelled B_{zl},B_{zh}. **b** Zoom into the left B_{zl} transition displaying a spin polarization. **c** Zoom of the central $S = {}^1/_2$ related spin signature. **d** Zoom into the right B_{zh} transition revealing a population inversion.

Concluding, the spin transitions that cause these EPR signals are optically inactive. Although spin $S = {}^1/_2$ centres in hBN were reported in the late 1970s and assigned to a one-boron-centre or three-boron-centre defect[29], it can be assumed that there is a $S = {}^1/_2$ center occupying a boron site in the lattice interacting with a $14N$ ($I = 1$). However, this interpretation is beyond the scope of this work. On the other hand, the second group of EPR lines in Figure 5.3b,d (labelled B_{zl}, B_{zh} with l, h indices denoting low and high magnetic field transitions and the principal symmetry axis $\vec{c}$ the defect orientation $\vec{B} \parallel \vec{c} \parallel \vec{z}$) consists of two widely separated transitions, which are strongly responsive to optical excitation (532 nm laser). The splitting between the lines B_{zl} and B_{zh} ($\Delta B \approx 260$ mT) is the same as in the ODMR experiments under the same conditions performed on the hBN flakes (see Figure 5.4). The EPR signals can be satisfyingly described by the spin Hamiltonian (equation 5.1) with the following Zeeman and ZFS parameters: $S = 1$, $g = 2.000$, ${}^D/_h = 3.6$ GHz.

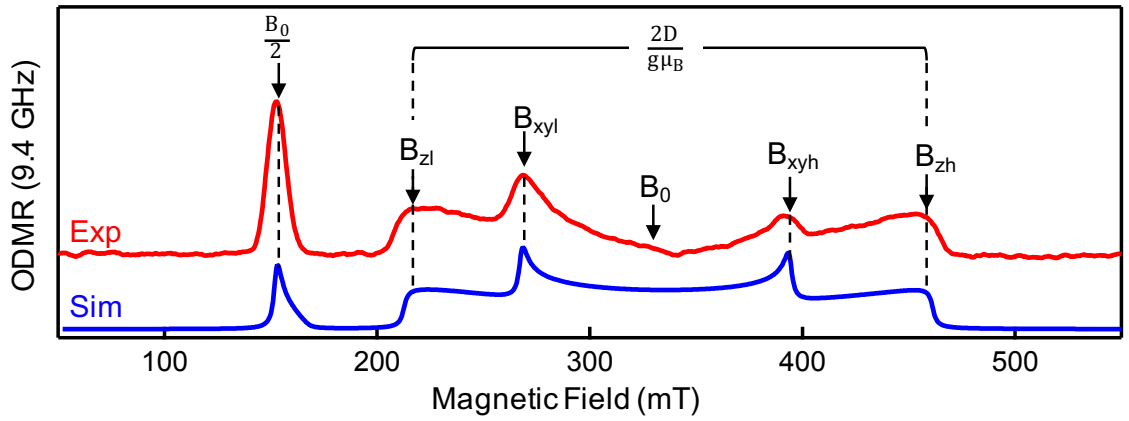

Figure 5.4: X-band (high field) ODMR spectrum (red) and simulation (blue) of randomly-oriented exfoliated hBN flakes. Five peaks are displayed corresponding to changes in fluorescence intensity ($\Delta PL/PL$), as a function of the applied static magnetic field B. Four distinct resonance features corresponding to the selection rules $\Delta m_s = \pm 1$, which are labeled B_{zl}, B_{zh}, B_{xyl}, B_{xyh} together with a "half-field" resonance at $B_0/2$, corresponding to the double-quantum transition with $\Delta m_s = \pm 2$. The latter feature is often used to identify triplet states ($S = 1$) and to distinguish these from higher spin states. D indicates the zero-field splitting parameter. $T = 5$ K and $\lambda_{exc} = 532$ nm.

The EPR transitions between these triplet sublevels are also visible without optical excitation (black trace in Figure 5.3), suggesting that the investigated triplet state is in the ground state.

The ZFS parameter E, which became apparent in ODMR measurements at $B = 0$ (Figure 5.2), could not be easily resolved in X-band EPR due to its small magnitude. It is, however, noticeable that the EPR measurements yield a slightly larger value for the ground-state ZFS parameter $D/h = 3.6$ GHz than was determined from zero-field ODMR. This is expected for triplet spin centres [98] and this difference can be attributed to a pronounced temperature dependence of D varying between 3.6 GHz at $T = 5$ K (determined via EPR and ODMR) and 3.48 GHz at $T = 300$ K (ODMR). Assuming a linear dependence, this would lead to a slope of approximately 0.4 MHz/K, which can be reasonably expected for the temperature-induced hBN lattice expansion (see Chapter 7.2 for a detailed analysis).

Notably, while the signal of B_{zl} is increasing under optical excitation revealing a spin polarization (see Figure 5.3b), the phase of the B_{zh} signal shown in Figure 5.3d becomes opposite (up-down to down-up) upon optical excitation and an emission is observed rather than absorption for the EPR transition B_{zh}. This can be explained by an optically induced population inversion ρ taking place amongst the spin-triplet sublevels of the ground state—with either the $m_S = \pm 1$ or $m_S = 0$ sublevels being lower lying at $B = 0$.

5.4.2 Sign of the Zero-Field Splitting

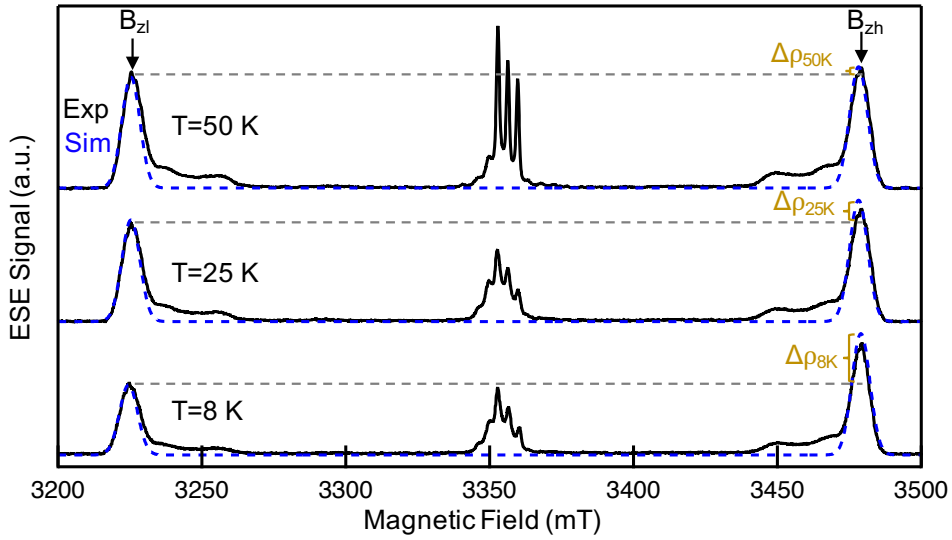

Figure 5.5: Dark W-band Electron Spin Echo (ESE) EPR spectra. Experimental data (black solid line) and simulations (blue dashed trace) show a pronounced transition for higher magnetic fields. The difference is indicated with $\Delta\rho$ for different temperatures ($T = 8, 25, 50$ K).
(Measurements provided by V. Soltamov, S. Orlinskii and G. Mamin)

The order of the energy sublevels $m_S = 0, \pm 1$ is determined by the sign of the ZFS parameter D, which is positive in this case ($D > 0$). To prove this independently, EPR studies without optical excitation are conducted and different signal intensities for B_{zl} and B_{zh} transitions are found. Since the expected differences are quite small due to the Boltzmann statistic, very high magnetic fields and low temperatures facilitate the effect on the signal. Therefore, the EPR spectra are performed in a W-band $\nu = 94$ GHz ($B \approx 3 - 3.5$ T) spectrometer at cryogenic temperatures.

Figure 5.5 shows a W-band electron spin echo (ESE)-detected EPR spectrum of the hBN single crystal for $\vec{B} \approx\parallel \vec{c}$ orientation measured in the dark at $T = 8$ K, $T = 25$ K and $T = 50$ K, respectively. The spectrum clearly reveals that the intensity of the low-field transition (B_{zl}) is lower in magnitude than that of the high-field transition (B_{zh}). The effect is pronounced for lower Temperatures ($\Delta\rho_{8\,\mathrm{K}} > \Delta\rho_{25\,\mathrm{K}} > \Delta\rho_{50\,\mathrm{K}}$). Since the relative magnitudes of the EPR transitions under such experimental conditions are determined only by the difference $\Delta\rho$ of the thermal populations of the Zeeman levels, the less intense B_{zl} EPR line can be attributed to the transition $m_S = 0 \rightarrow m_S = \pm 1$ and deduce the sign of D to be positive (see Chapter 2.2.2). Schematic comparison of the energetic order of spin sublevels for positive ($D > 0$) and negative ($D < 0$) ZFS is shown in Figure 5.6a. This result is in line with ab initio theoretical predictions of D having a positive sign in the ground state of the V_B^- defect[49].

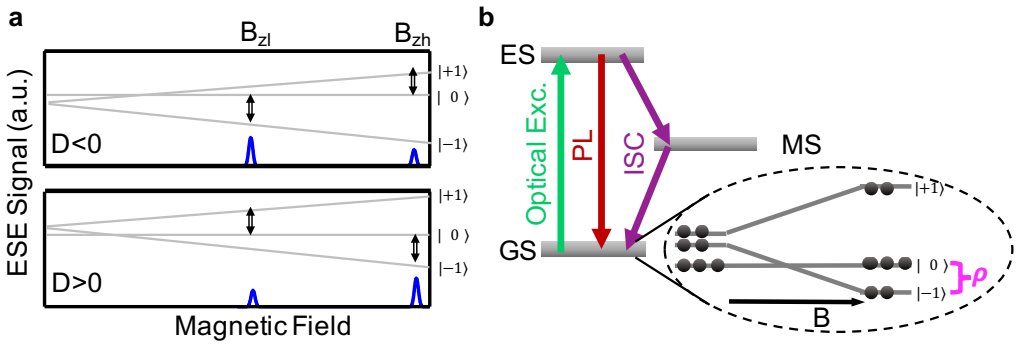

Figure 5.6: Energy level scheme of the V_B^- centre in the hBN. a Schematic comparison of the energetic order of spin sublevels for negative ($D < 0$) and positive ($D > 0$) ZFS. **b** Simplified energy-level diagram illustrating the optical pump cycle between ground state (GS), excited state (ES) and metastable state (MS) resulting in population inversion ρ, between $|0\rangle$ and $|-1\rangle$ ground-state spin sublevels. Optical excitation (green), photoluminescence (red) and intersystem crossing (purple) are indicated by arrows.

In Figure 5.6b, the tentative energy-level scheme of the spin defect consistent with the observations of Figure 5.3, 5.5 and 5.6 is proposed. Zeeman splitting of the $m_S = \pm 1$ levels results in the crossing of $m_S = -1$ and $m_S = 0$ sublevels, while optical pumping induces population transfer (via excited and metastable states) from $m_S = \pm 1$ to $m_S = 0$,and results in microwave emission at the B_{zh} field.

5.4.3 Symmetry of the Defect

To test the symmetry of the defect more closely the angular dependencies of the EPR signals are analysed for rotations around the polar and azimuthal angles θ and Φ, respectively. Figure 5.7 shows the EPR signals measured for a polar rotation (θ) of the magnetic field from parallel ($\vec{B} \parallel \vec{c}$) to perpendicular ($\vec{B} \perp \vec{c}$) orientation and for azimuthal rotation Φ in the (0001) plane ($\vec{B} \perp \vec{c}$) of an hBN single crystal. The angular variation of the resonant magnetic fields is described by numerical simulation (shown with blue traces in Figure 5.7b,e) of equation 5.1 employing the full set of the previously derived parameters (S, g, D, E). In addition, the simulation for the central $S = 1/2$ signature is shown in red in Figure 5.7c,f.

For both polar (Figure 5.7a) and azimuthal rotation (Figure 5.7d) an exceptionally good agreement of the overlaid simulated traces and the magnetic field positions of the experimentally observed transitions can be found. For the angular dependence shown in Figure 5.7e the splitting between the lines remains unchanged. These results point at the $\vec{c}$ axis being the axis of symmetry of the almost uniaxial ODMR active triplet. Although hBN can accommodate a large number of defects (either intrinsic or extrinsic)

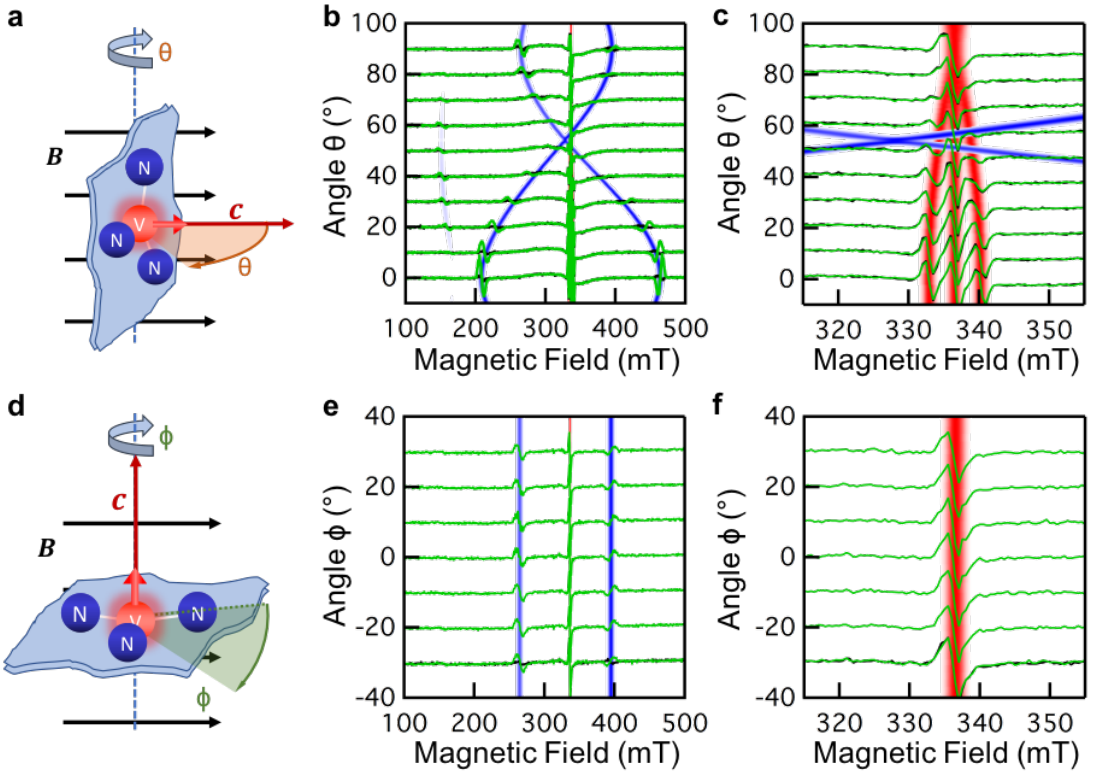

Figure 5.7: Angular dependence of EPR spectra (green traces) and simulations (blue/red traces) in hBN single crystal. a-f, V_B^- centre consits of a vacancy (red sphere) surrounded by three nitrogen atoms (blue spheres). **a-c**, Rotation of the magnetic field $\vec{B}$ (black arrows) relative to the $\vec{c}$ axis (red arrow) by angle θ from parallel ($\theta = 0$, $\vec{B} \parallel \vec{c}$) to perpendicular ($\theta = 90$, $\vec{B} \perp \vec{c}$) orientation **a** with resulting EPR spectra **b** (simulation in blue). **c** Zoom of centre transition in order to resolve the angular variation of the $S = 1/2$ centre (central EPR group, see text). The corresponding simulation is shown in red. **d-f** Rotation of the magnetic field $\vec{B}$ (black arrows) by angle Φ in the (0001) plane of hBN ($\vec{B} \perp \vec{c}$) **d** with resulting EPR spectra **e**. **f** Zoom of centre transition.

in its lattice sites (see Chapter 2.1.2), the combined EPR and ODMR data allow us to pinpoint the type of defect. The common defects include boron vacancies (V_B), nitrogen vacancies (V_N) and anti-site complexes (for example, a nitrogen atom on a boron site next to a vacancy ($V_N N_B$), or substitutional carbonrelated defects, such as C_B or even $V_N C_B$. The complex defects, such as $V_N N_B$ and $V_N C_B$, were shown to have in-plane C_{2v} symmetry[45,101], which is inconsistent with the observations of an almost axial defect with respect to the $\vec{c}$ axis (see Figure 5.7). On the other hand, it was also shown that point defects V_B, C_B and V_N are characterized by the uniaxial D_{3h} group symmetry, with a C_3 rotation axis parallel to the c axis. These defects are thus compatible with these findings and must be considered. Recent theoretical investigations of point defects in hBN have shown that the neutral V_N^0 and C_B^0 defects should be $S = 1/2$,

but they may become non-magnetic in their energetically preferred charge state V_N^+, V_N^-, C_B^+, while the negatively charged boron vacancy (V_B^-) has been predicted to be stable with an $S = 1$ ground state [102]. In addition, the optically induced spin polarization of the V_B^- triplet ground state through the spindependent intersystem crossing pathway has already been theoretically proposed [45].

5.4.4 Hyperfine Splitting and the Magnetic Environment

To discern between possible hBN lattice sites for the defect, the hyperfine structure of EPR and ODMR signals is analysed. The two simplest possible environments for a D_{3h} group symmetry are illustrated in Figure 5.8a,b for a boron and a nitrogen vacancy, respectively. Figure 5.8c,d shows the B_{zl} EPR line together with the zero-field ODMR ν_1 transition.

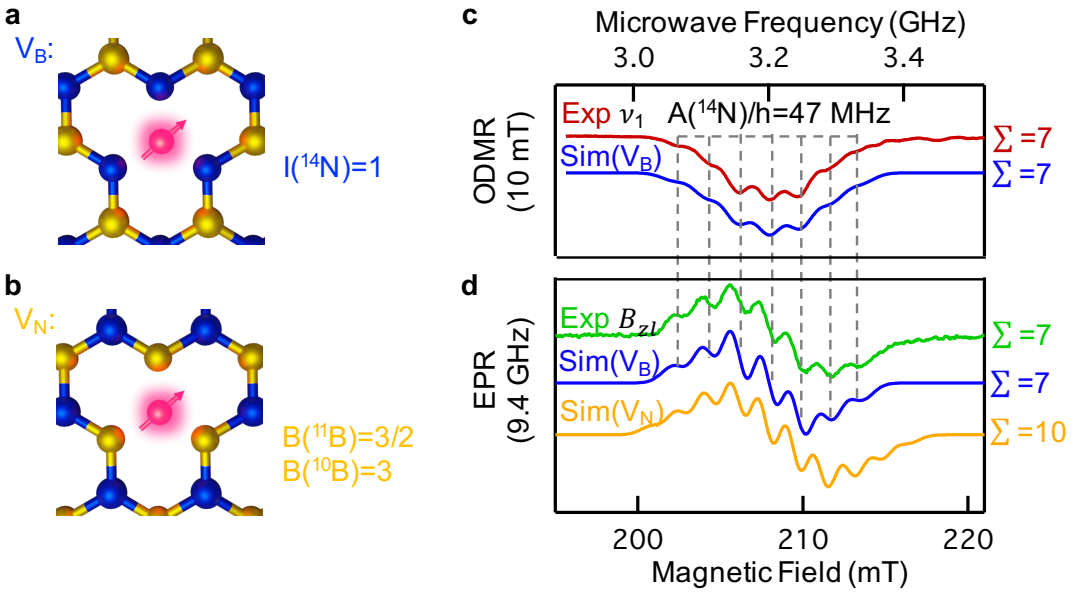

Figure 5.8: Magnetic enviroment of the defect. **a** Surrounding of a boron vacancy (V_B^-) consisting of three equivalent nitrogens. **b** Surrounding of a hypothetical nitrogen vacancy (V_N) consisting of three boron atoms. **c** Hyperfine splitting of ODMR ν_1 (red trace) line. **d** Hyperfine splitting of EPR B_{zl} (green trace) transition. Vertical bars indicate seven transitions caused by hyperfine interaction with three equivalent nitrogen nuclei. The blue traces are the simulated EPR/ODMR spectra of the (V_B^-) defect with equation X, where the hypferfine term with a splitting constant $A/h = 47$ MHz is considered. The orange trace is a simulated ODMR spectrum for a nitrogen vacancy (V_N) for comparison. In total 10 (19) hyperfine peaks are expected which differs from the measured spectra.

The hyperfine splitting is known to be due to the interaction of the electron spin with the surrounding nuclear spins, sometimes called superhyperfine interaction - which in turn reflects the nature of the nearest atoms (in this case either three boron or three nitrogen atoms). It can be described by adding the term $\sum_k \vec{S} A_k \vec{I}_k$ to equation 5.1, where A_k is the hyperfine interaction and I_k is the nuclear spin. The number of observed hyperfine lines is seven (Figure 5.8c,d). This is consistent with a spin $S = 1$ point defect localized at the boron site interacting with $n = 3$ equivalent nitrogen atoms (nuclear spin $I = 1$, $^1 4N$, 99,63 % natural abundance) and it thus supports the cases of the C_B and V_B defects with $2nI + 1 = 7$ hyperfine transitions. Conversely, for V_N there is hyperfine interaction of the electron spin with $n = 3$ equivalent boron atoms, each having two isotopes ($I = 3/2$, ^{11}B, 80.2 % natural abundance and $I = 3$, ^{10}B, 19.8 % natural abundance), resulting in $2nI+1 = 10$ plus $2nI+1 = 19$ transitions. The V_N simulation shown in orange takes the natural isotope abundance into account and is dominated by the ten hyperfine transitions for ^{11}B. Consequently, ruling out V_N, the numerical simulations of the hyperfine structure agree well with a carbon atom or a vacancy localized at the boron site (see Figure 5.8c,d) yielding a hyperfine splitting constant $A/h = 47$ MHz. Looking more closely, there are no obvious spectral features pointing at hyperfine interactions with second neighbours (boron). These $n = 6$ equivalent boron atoms would have a much smaller coupling constant A with $2nI + 1 = 20$ plus 38 transitions for ^{10}B and ^{11}B, respectively. The spectral features would fall within the observed linewidth and would only result in slight broadening and miniscule modulations on top of the spectrum. Alternatively, the lack of obvious secondneighbour hyperfine interaction could be a sign of a very localized wavefunction. Future simulations, in combination with electron nuclear double resonance experiments, could help to clarify the wavefunction extent.

5.5 V_B^- in other hBN Samples

Note that while the defect symmetry (D_{3h}) and lattice site (boron) can be determined on the basis of EPR data alone, it cannot be fully discerned whether the defect is intrinsic (V_B) or extrinsic (C_B). Consequently, irradiation of pristine hBN material is performed (see Chapter 4) with various species: ion implantation with different ions (lithium, gallium and carbon) on hBN flakes, as well as neutron irradiation on exfoliated flakes and an hBN single crystal. The 800-nm PL band (Figure 5.1) can be observed for all of these samples (Figure 5.9a) except the carbon implanted sample. The PL of the carbon (gray) enriched sample is significantly shifted towards lower wave-

lengths (2 eV emission) and fits to a defect with another ODMR signature (see[47] for futher details). Furthermore, ODMR is detected (Figure 5.9b) for all but the gallium-implanted flakes, due to damage from the gallium beam and very low PL intensity to yield an ODMR contrast. The Li-implanted flakes show the same ν_1 and ν_2 resonances as the single crystal. Additionally, an asymmetrical ODMR signal at $\nu_0 \approx 3.5$ GHz is visible. This central peak in the Li-implanted flakes can be tentatively attributed to the same spin defects found in single crystals, but randomly oriented at the edges and surfaces. Strong angular dependence of EPR transitions known for single crystals (see Figure 5.7) may result in a spectral collapse of ν_1 and ν_2 resonances. To backup this spectrum with simulations, the superposition of the simulation of the oriented sample is calculated with an additional spectrum using the same EPR parameters - but with randomly oriented spin-defects. We can thus deduce that the investigated defect is indeed of intrinsic nature and is most likely the V_B^-.

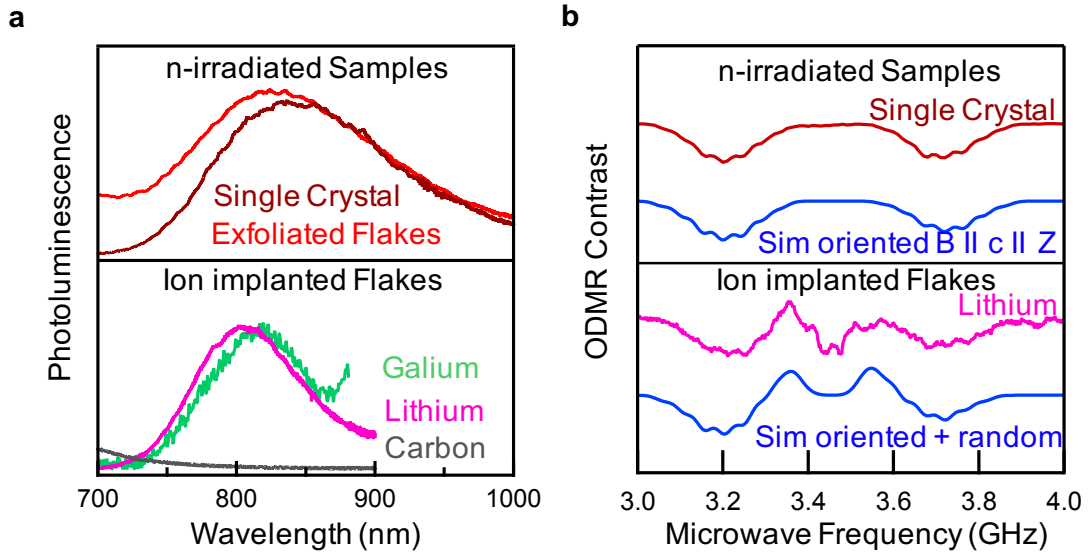

Figure 5.9: Comparison of PL and ODMR spectra of various hBN samples at room temperature and λ_{exc} = 532 nm. a PL spectrum of the neutron irradiated single crystal (same as Figure 5.1) together with spectra of neutron irradiated exfoliated flakes (same as Figure 5.2) and ion implanted flakes (on glass substrate). All samples except the carbon implanted hBN flakes show a similar PL at $\lambda_{max} \approx 800$ nm, therefore only the central part of the spectra is shown. **b** ODMR spectrum at 10 mT of the neutron irradiated single crystal with Easyspin simulation (same as Figure 5.2,5.8) together with the spectrum of lithium ion implanted flakes on glass substrate.

5.6 Conclusion

To conclude, a room-temperature optical initialization and readout of ensembles of intrinsic $S = 1$ defect centres in hBN have been demonstrated. From rigorous EPR measurements performed on hBN single crystal, exfoliated and ion-irradiated flakes,the proposed investigated defect is the negatively charged boron vacancy V_B^-. An overview of the determined spin Hamiltonian parameters is listed in Table 5.1.

Parameter	Value	Measurement
S	1	X-EPR, ZfODMR
g	2.000	ZfODMR
D/h ($T = 300$ K)	3.48 GHz	ZfODMR at 300 K
D/h ($T = 5$ K)	3.6 GHz	X-EPR, X-ODMR at 5 K
D	> 0	W-EPR at 8, 25, 50 K
E/h	50 MHz	ZfODMR
A/h	47 MHz	ZfODMR, X-EPR

Table 5.1: Overview of the extracted spin Hamiltonian parameters.

Furthermore, a spin polarization under optical excitation and optically induced population inversion in the triplet ground state has been demonstrated, which provides the basis for coherent spin manipulation. While the research into spin defects always starts with ensembles, it can be confidently expected that in the future it will be possible to address individual V_B^- defects, particularly using super-resolution techniques[103]. The main challenge lies in the means to increase the quantum efficiency and engineer defects deterministically at various densities. One particularly promising approach is to use resonant excitation to select one or a few defects out of an ensemble, at cryogenic temperatures[104]. This stimulates further research in hBN-based heterostructures for quantum-sensing applications and drives interest into deterministically engineering single V_B^- centres. The work will also accelerate the research into spin optomechanics with hBN, particularly given the established theoretical framework[105] and advances in nanofabrication of resonators[106]. The very fact that spin echo experiments were possible on hBN clearly proves that the investigated system is a coherent spin system characterized by a spin–spin coherence time that is long enough for coherent spin manipulation by microwave fields. The spin–spin coherence time at cryogenic temperatures can be estimated to be several microseconds and is limited by the nuclear bath, in particular by boron nuclei with high gyromagnetic ratio, so that isotopic purification in hBN will be necessary. As reported, isotope purification of 2D materials is much easier than for conventional 3D systems and coherent manipulation of spin states may become feasible, yielding potentially high coherence time[107]. In this context, the V_B^-

defect identified here may be advantageous due to weaker coupling of the defect electron spin with the surrounding ^{14}N nuclear bath compared to other possible defect configurations.

6 Coherent Control of the Boron Vacancy

ABSTRACT: Optically active spin defects are promising candidates for solid-state quantum information and sensing applications. To use these defects in quantum application coherent manipulation of their state is required. Here, a coherent control of ensembles of boron vacancy centers in hexagonal boron nitride (hBN) is realized. Especially, by applying pulsed spin resonance protocols, a spin-lattice relaxation of $T_1 \approx 18$ μs and a spin coherence time of $T_2 \approx 2$ μs is measured at room temperature. The spin-lattice relaxation time increases by three orders of magnitude at cryogenic temperature. By applying a method to decouple the spin state from its inhomogeneous nuclear environment the optically detected magnetic resonance linewidth is substantially reduced to several tens of kilohertz. These results are important for the employment of van der Waals materials for quantum technologies, especially in the context of high resolution quantum sensing of two-dimensional heterostructures, nanoscale devices, and emerging atomically thin magnets.

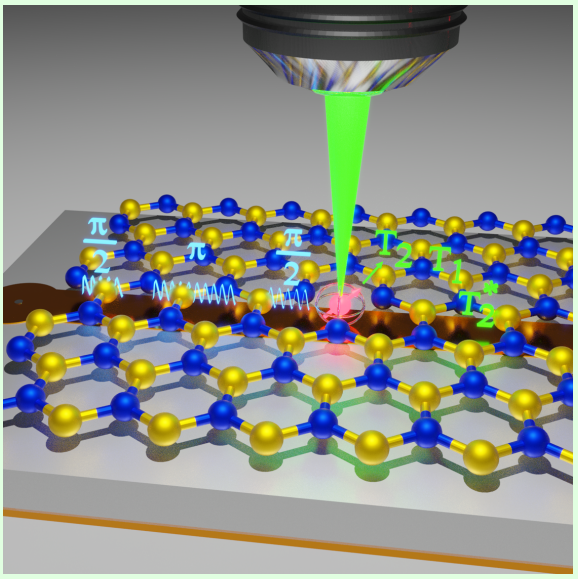

This chapter is based on A. Gottscholl et al. "Room temperature coherent control of spin defects in hexagonal boron nitride", *Science Advances*, **7** eabf3630 (2021) [22].

6.1 Introduction

Van der Waals (vdW) crystals have recently emerged as a promising family of materials to investigate light matter interaction at the nanoscale [40,108–110]. Out of a growing suite of vdW crystals, hexagonal boron nitride (hBN) stands out owing to its ability to host optically active defects that emit single photons of light while displaying spin-optical quantum properties at room temperature [21,83]. A specific defect of interest is the negatively charged boron vacancy (V_B^-) center (see previous Chapter 5). This atom-like defect has a spin triplet ground state ($S = 1$) [45], which can be prepared, manipulated, and optically read out through a combination of microwave and laser excitation cycles [21]; a feat that makes it particularly appealing for quantum sensing and spintronic applications. In the realm of vdW heterostructures, having an optically active spin sensor confined in an intrinsically atom-thin, two-dimensional (2D) host is highly desirable, as it allows for achieving high-resolution sensing strategies with specific requirements such as, for instance, imaging the magnetic domains in 2D ferromagnets [111–113] or magnetic superlattices [114]. However, before these defects can be used in practical implementations, full understanding and, ultimately, control of their coherent properties must be acquired. In this chapter, a coherent control of an ensemble of V_B^- defects in hBN is demonstrated. While coherent control of spin qubits in 3D crystals (e.g. diamond, silicon carbide (SiC), or rare earth ions in glass) [115–119] has been demonstrated, spin defects in vdW crystals are still unexplored. It is further shown that the coherence properties of V_B^- spin ensembles are influenced by the coupling with the surrounding nuclei spin bath (^{14}N with $I = 1$,^{10}B with $I = 3$, and ^{11}B with $I = 3/2$). By applying optically detected two- and three-pulse electron spin-echo envelope modulation (ESEEM), magnetic and quadrupole fields of surrounding nuclei is probed and information about hyperfine coupling and quadrupole splitting is obtained, although an exact assignment to nitrogen or boron in their corresponding coordination shells remains ambiguous. By implementing a two-frequency optically detected magnetic resonance (ODMR) technique to the V_B^- spin system, the ability is demonstrated to selectively saturate one of the hyperfine transitions and effectively decouple the electron spin system from the nuclear bath, which allows estimating the upper limit of the highest achievable coherence times.

6.2 Coherent manipulation of V_B^-

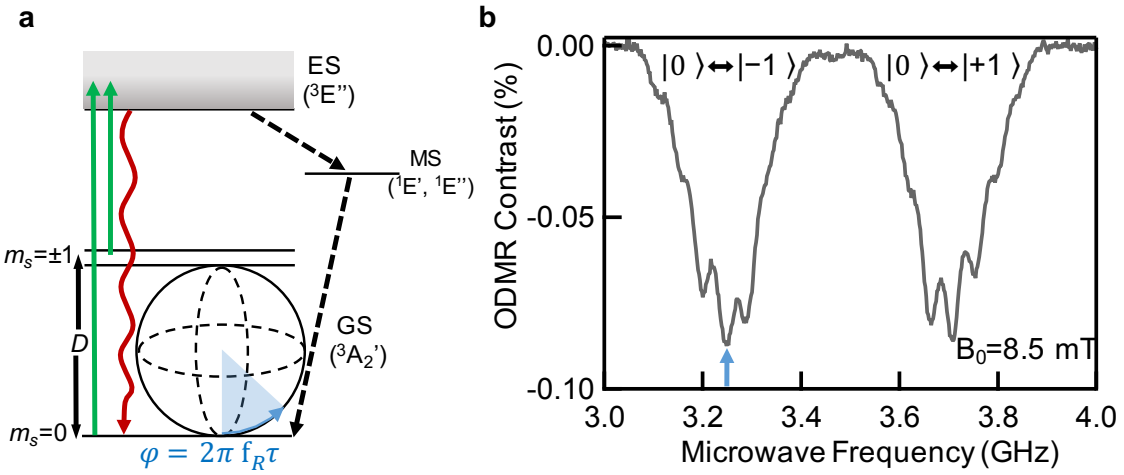

Figure 6.1: V_B^- defect in hBN. **a** V_B^- defect energy diagram and the optical pumping cycle comprising excitation to excited state (ES)(green), radiative recombination (red), and non-radiative decay to ground state (GS) via metastable state (MS) (dashed lines). D denotes ZFS. The $|0\rangle \longleftrightarrow |-1\rangle$ transition is represented on a Bloch sphere. The ground state $|0\rangle$ is spin polarized by a laser (green) and can be manipulated to an angle ϕ after applying microwaves with the Rabi frequency f_R for a time τ. **b** Continuous wave (cw) ODMR spectrum with two charecteristic transitions in a magnetic field of 8.5 mT. Both signals reveal structure due to hyperfine interaction (HFI) with three next neighboring nitrogen atoms. The blue arrow indicates the frequency of the resonant transition at which the pulsed measurements were performed.

The corresponding simplified energy level diagram is shown in Figure 6.1a. The defect has a nominal D_{3h} symmetry as demonstrated in the previous chapter (lower symmetries are expected because of strain and reorganization), and the main optical transition takes place between the ${}^3E''$ and ${}^3A_2'$ levels. When excited with a 532 – nm laser source, the defect emits at a wavelength centered at ~ 850 nm. The inset shows the evolution of the $|0\rangle$ substate on the Bloch sphere under the action of the microwave field.

Figure 6.2b shows the continuous wave (cw) ODMR spectrum of the V_B^- defects at room temperature. The signal is centered around the 3.5 – GHz frequency, corresponding to the zero-field splitting (ZFS) (see previous chapter for detailed information). The photoluminescence (PL) intensity signal is frequency dependent. The two distinct features at frequencies ν_1 and ν_2 correspond to the ground-state spin transitions $|0\rangle \longleftrightarrow |-1\rangle$ and $|0\rangle \longleftrightarrow |+1\rangle$ and occur because the ground $m_s = \pm 1$ states scatter less photons than the $m_s = 0$ state, through the excited state. Both features show a clearly resolved hyperfine splitting with seven peaks due to three equivalent nitrogen nuclei ($2nI + 1 = 7$, with $n = 3$, $I = 1$) in the hBN plane surrounding the missing boron atom.

To explain the observed transitions and their variation with the magnetic field, the spin Hamiltonian, which describes electron spin-spin interaction (ZFS), electron and nuclear Zeeman interaction, electron-nuclear hyperfine interaction (HFI), and electric quadrupole interaction (QI) is used.

$$H = D\left(S_z^2 - S\frac{(S+1)}{3}\right) + E\left(S_x^2 - S_y^2\right) + g\mu_B\vec{B}\vec{S} + \vec{S}\mathbf{A}\vec{I} + Q\left(I_z^2 - I\frac{(I+1)}{3}\right) - g_N\mu_N\vec{B}\vec{I} \quad (6.1)$$

where D and E are the ZFS parameters, S is the total electron spin ($S = 1$ for V_B^-), g is the Landé factor, μ_B is the Bohr magneton, μ_N is the nuclear magneton, B is the static magnetic field, $S_{x,y,z}$ are the spin-1 operators, $\mathbf{A}$ is the HFI tensor, I and I_Z are nuclear operators, and Q is the quadrupole coupling constant. The hyperfine coupling constant due to coupling with ^{14}N ($I = 1$) in the first coordination shell $A = 47$ MHz is known from the experiment and confirmed by calculations [21,49].

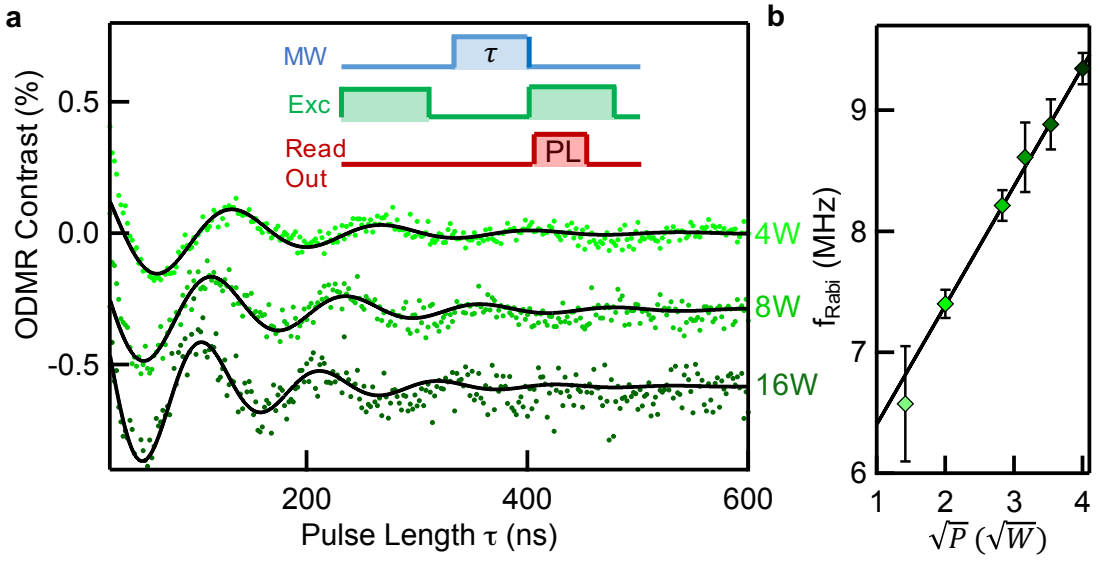

Figure 6.2: Coherent manipulation of V_B^- spin centers in hBN at room temperature. a Optically detected Rabi oscillations on transition $|0\rangle \longleftrightarrow |-1\rangle$ after initialization into $|0\rangle$ state for different microwave (MW) powers. The inset schematically shows the pulse sequence, in which the first excitation laser pulse (green) is used for the initialization of the spin state and the second one for a readout (red) of the current state after the microwave pulse (blue). **b** Rabi frequency f_{Rabi} versus square root of microwave power P, which is proportional to B_1 field.

To get access to the spin dynamics of the V_B^-, and to determine their spin relaxation times T_1 and T_2, pulsed ODMR measurements are performed. They are based on preparing the ground spin state of the system by optical excitation, applying microwave pulses of variable length to coherently manipulate the spin state, and lastly perform-

ing an optical readout of the state. Figure 6.2a shows Rabi oscillations with a characteristic frequency f_R in the megahertz range, which depends on the microwave power and, hence, the strength of the B_1 component of the microwave field, as shown in Figure 6.2b. These measurements allow calibrating the microwave pulse length at a given power for subsequent pulsed ODMR experiments.
The microwave protocol for measuring the Rabi oscillations (Figure 6.2a) can also be used to estimate the upper limit of the spin-dephasing time T_2^* induced by surrounding magnetic moments by fitting the Rabi oscillations with the function $f(\tau) = f_0 + A \cdot exp\left(-\tau/T_2^*\right) cos\left(2\pi f_{Rabi}\tau\right)$ as $T_2^* = 100$ ns.

6.3 Spin-Lattice relaxation T_1

6.3.1 Room Temperature T_1

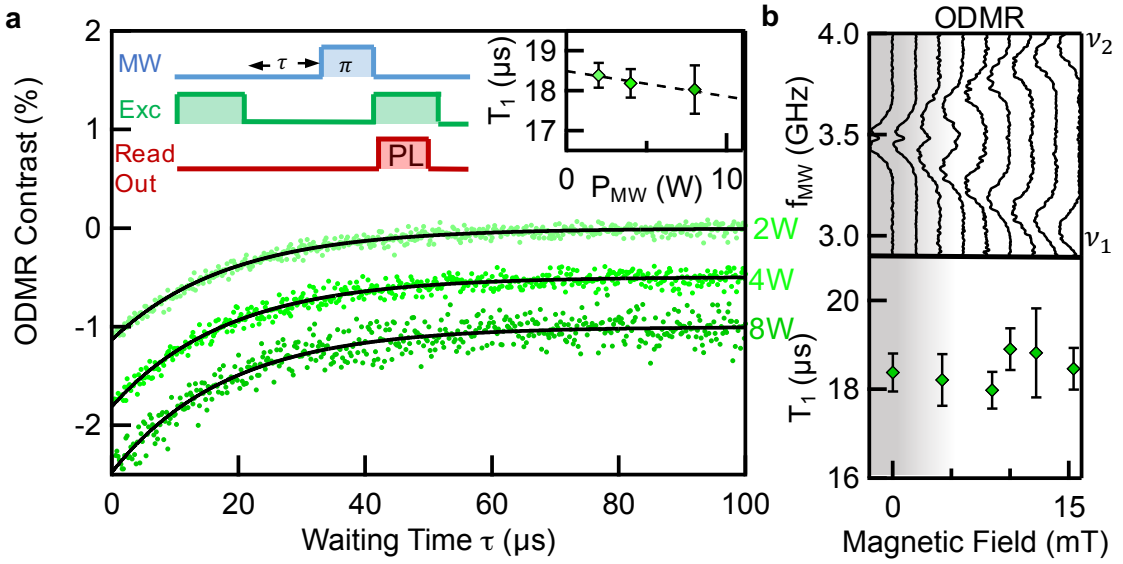

Figure 6.3: Spin-lattice relaxation dynamics of V_B^- spin centers in hBN at room temperature. **a** ODMR signal decay with waiting time τ at $T = 300$ K for different microwave powers (2, 4, 8 W). The pulse sequence is schematically shown, in which the duration of microwave π-pulse is known from Rabi experiments and the waiting time τ is varied. The T_1 time slightly increases for lower microwave powers (inset). **b** T_1 versus external magnetic field (0 to 15 mT)(bottom). The gray background indicates the magnetic field range where two ODMR transitions ν_1 and ν_2 overlap (top).

The upper limit for spin coherence is given by the spin-lattice relaxation time T_1, which is determined with a standard π-pulse sequence[115,116], as shown in Figure 6.3. The T_1 time is around 18 μs and does not seem to be influenced by an external magnetic field, even if the two ODMR peaks collapse and form a single peak at $B = 0$ (see Figure 6.3b). The gray background indicates the overlap of the two transitions ν_1 and

ν_2 below 5 mT. This can be explained by the large ZFS compared to the small external magnetic field applied. Note that ZFS of V_B^- centers in hBN is 3.5 GHz and the magnetic fields applied in the experiments are not large enough to induce the level anticrossing ($B \approx 125$ mT). Hence, the local magnetic field at the spin defect site dominates the spin properties. This leads to a robust spin-lattice relaxation dynamic of the V_B^- defect, independent of external magnetic perturbation fields. To gain further insights into the nature of spin-lattice relaxation mechanisms, e.g. the interaction with lattice phonons, the temperature dependence of T_1 is probed. In this case, one would vary the spectrum of vibronic lattice modes, which are an effective relaxation channel if they have energies comparable to the Larmor frequency of the electron spin. The V_B^- ZFS is very large, so one can expect a relaxation behavior similar to the nitrogen vacancy (NV) centers in diamond, where the direct one-phonon absorption and emission processes are neglected at higher temperatures [120]. Nevertheless, the 2D character of the hBN and the symmetry of the spin defects are expected to influence their vibronic properties compared to 3D crystals [121,122], although detailed calculations about these effects in the presence of spin defect or experimental data are not available yet.

6.3.2 Temperature dependence of T_1

To study the behavior of spin-phonon contributions to T_1, the pulse sequence shown in Figure 6.3a is used and the temperature is varied between 300 and 20 K. Figure 6.4a reveals a monotonic growth of T_1, as the temperature decreases, up to a value of 12.5 ms at $T = 20$ K (see Figure 5.5b). In general, the T_1 time is governed by the following processes [67,123]

$$1/T_1 = A_0 + A_1 T + A_s T^s + \frac{R}{exp\left(\frac{\Delta}{k_B T}\right) - 1} \tag{6.2}$$

Single-phonon scattering processes are considered by the linear term A_1. Two-phonon processes (direct transition, Stokes, anti-Stokes, and spontaneous emission) are described by the A_s term (higher orders $s+1$ and $s+2$ are neglected), where $s = 4\nu + 2d - 3$ [123]. Because d is the dimension of the system and ν is a phenomenological spin-phonon coupling factor reflecting the symmetry of the lattice ($\nu = 1/2$ for a noncubic), one expects $s = 5$ for the NV centers in diamond and silicon vacancies (V_{Si}) in SiC. For a noncubic 2D system such as hBN ($d = 2$, $\nu = 1/2$), one expects $s = 3$. Orbach-type processes resulting from quasi-localized phonon modes are described by an exponential contribution with the characteristic energy $\Delta = \hbar\omega_{loc}$ and its fitting parameter R with dimension per second. Therefore, the spin-lattice relaxation rate is ultimately limited by A_0, which provides the longest achievable T_1 time. To quantify the observed temperature dependence shown in Figure 6.4b, a double logarithmic scaling of the

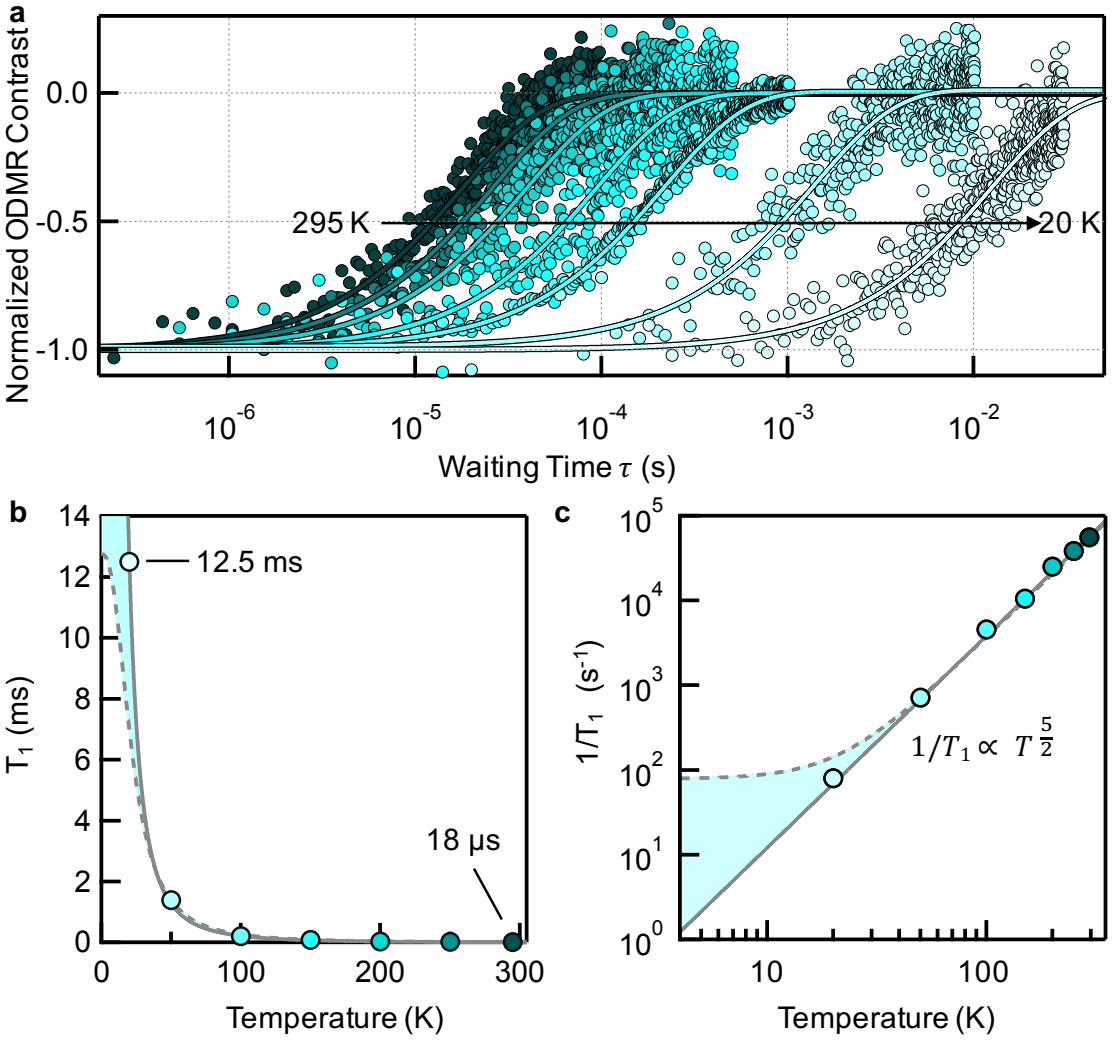

Figure 6.4: Spin-lattice relaxation dynamics of V_B^- spin centers in hBN at different temperatures (20 – 300 K). a Normalized ODMR signal decay with waiting time τ plotted on a logarithmic time scale.**b** Temperature dependence of the spin-lattice relaxation time of V_B^- spin centers in hBN. The T_1 time increases by three orders of magnitude from 18 μs to 12.5 ms, when lowering the temperature to 20 K. **c** Log-log plot for the spin-lattice relaxation rate ($1/T_1$) shows a $T^{5/2}$ behaviour over a broad temperature range. An upper boundary for the fastest spin-lattice relaxation rate can be estimated by assuming a saturation of the T_1 time at 20 K (highlighted in blue).

spin-lattice relaxation rate $1/T_1$ is depicted in Figure 6.4c. All observed values can be fitted with only one line with a slope of $s = 5/2$ that corresponds to $1/T_1 \sim T^{5/2}$ (see Figure 6.4c). This value differs from the expected values of $s = 3$ ($s = 5$) for a 2D (3D) system mentioned above. Because the experimental values are all in the linear regime (in the log-log scale), it is not possible to make any further assumptions regarding other spin-lattice rate contributions such as linear terms or Orbach-related effects. Never-

theless, an estimate for the lowest relaxation rate corresponding to the longest measured $T_1 = 12.5$ ms can be given. Assuming that the spin-lattice relaxation rate starts to level off and becomes temperature independent at temperatures below 20 K[67,116,120], an upper limit for the term $A_0 < 80\ s^{-1}$ can be set, as highlighted in blue in Figure 6.4b, c. After determining the T_1 relaxation time, the T_2 time is following.

6.4 Spin-Spin relaxation T_2

6.4.1 Room Temperature T_2

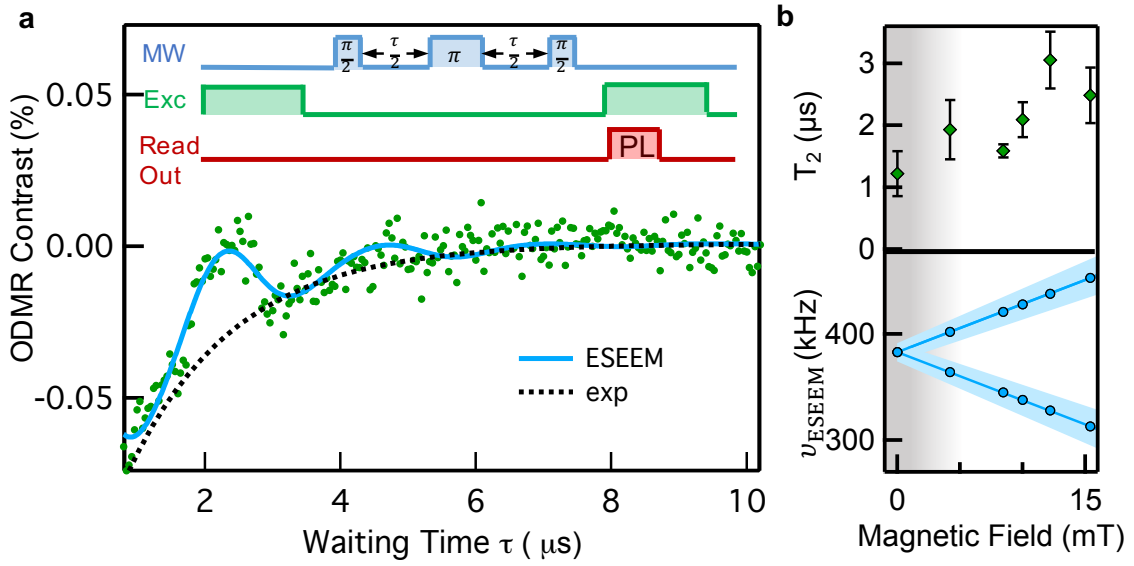

Figure 6.5: Spin-spin relaxation dynamics of V_B^- spin centers in hBN at room temperature. **a** The applied spin-echo pulsed sequence including the projection pulse $\pi/2$ and the ODMR contrast versus waiting time τ (green) is shown. The expected exponential rise (black dotted line) is superimposed by the oscillations (green and blue) due to the coupling of electron spins to nuclei (ESEEM effect, see text). The fit with modulated exponential function (blue) allows estimating the ESEEM frequencies and the T_2 time. **b** Top: T_2 time versus magnetic field. T_2 slightly decreases in the magnetic field range where ODMR transitions ν_1 and ν_2 overlap (gray area), indicating the presence of additional decoherence, e.g. due to HFI. Bottom: ESEEM frequency versus external magnetic field according to the observed oscillations in the spin-spin relaxation measurements.

The T_2 time of the V_B^- defects is measured with a Hahn spin-echo sequence[124–126]. The pulse sequence applied is $\pi/2 - \tau - \pi - \tau -$ echo, and the results are shown in Figure 6.5. Note that to enable optical detection of spin echo, an additional $\pi/2$-pulse[71,127,128] is required after the standard spin-echo pulse sequence to read out the spin polarization of a well-defined state (bright state $|0\rangle$) versus dark states $|\pm1\rangle$). The ODMR transient shows the exponential rise from which T_2 is determined. A room temperature coherence time of $T_2 \approx 2\ \mu$s can be extracted for an external magnetic field of 8.5 mT.

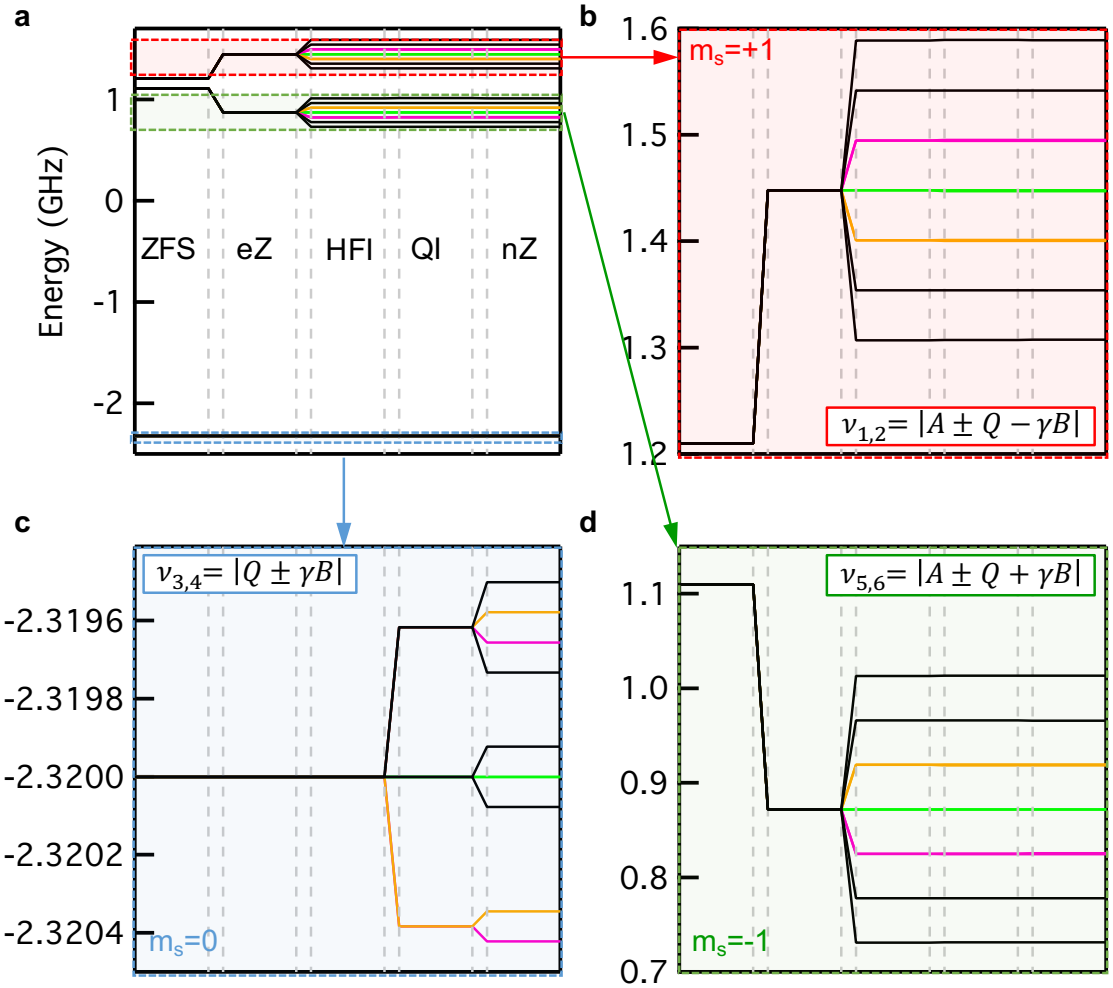

Figure 6.6: Energy diagram corresponding to spin-Hamiltonian (Equation 6.1) with 6 possible ESEEM frequencies taking three equivalent ^{10}N nuclei into account (B = 8.5 mT). a Overview of all energy levels. **b-d** Zoom into the energy levels corresponding to the different m_S states, 6 possible ESEEM frequencies are derived. Since the hyperfine coupling A = 47 MHz contributes to $\nu_{1,2}$ and $\nu_{5,6}$, they are not observable for the mentioned ESEEM measurements in the 100 kHz regime leaving $\nu_{3,4}$ as the detectable frequencies. The colors of the energy levels are representing the spin states $\Sigma m_I = +1$ (pink), $\Sigma m_I = 0$ (green) and $\Sigma m_I = -1$ (green), respectively (see Chapter 6.5 for further details).

As shown in Figure 6.5b, T_2 increases slightly to about 3 μs by increasing the magnetic field above the region where the ODMR signals overlap (gray zone). Furthermore, the ODMR transient is superimposed by oscillations containing two frequencies, as determined by Fourier analysis and plotted for different magnetic fields in Figure 6.5b. The effect is known as ESEEM[129] and is widely used to study interactions between electron and nuclear spins. In ESEEM, the electron spin-echo envelope exhibits amplitude modulation that corresponds to the nuclear magnetic resonance (NMR) frequencies of

nuclei, which are coupled to the electron spin. For the V_B^-, only one ESEEM frequency is expected if the HFI of the electron spin with three equivalent nitrogen nuclei ($I = 1$) in the first coordination sphere is considered. For all nuclei with $I > 1/2$, however, the quadrupole term becomes important, as described in Equation 6.1 because it modifies the NMR frequency spectrum considerably.

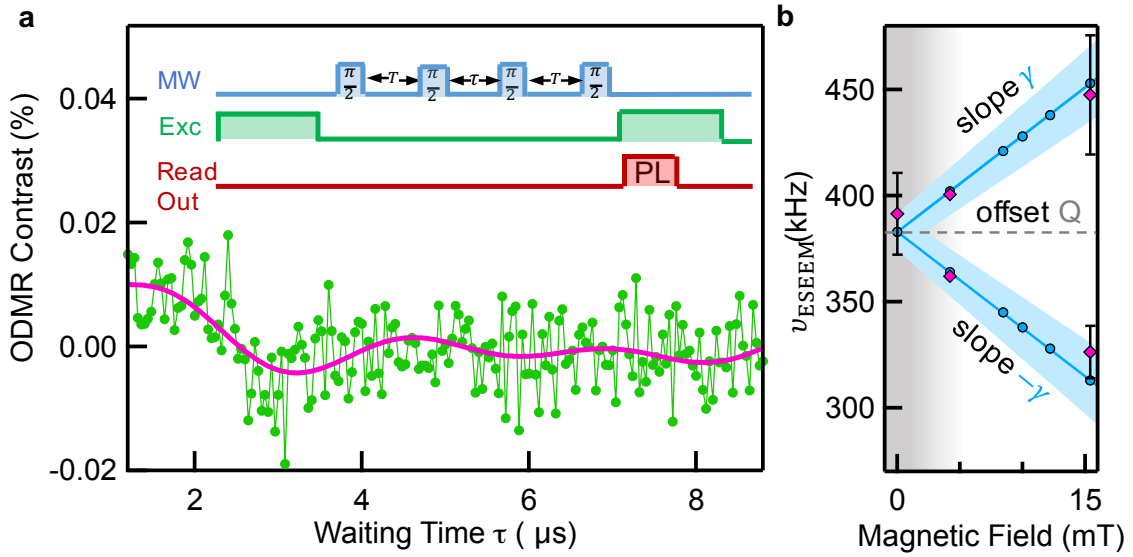

Figure 6.7: Three-pulse ESEEM of V_B^- spin centers in hBN at room temperature. **a** In order to confirm the ESEEM frequencies extracted from the T_2 measurements a three-pulse ESEEM measurements is applied to the system. The corresponding pulse sequence for the microwave and laser pulses is depicted in the inset. In contrast to three-pulse ESEEM in pulsed EPR measurements, a fourth pulse is required at the position of the expected echo in order to return the spin system into a well-defined state, which enables the optical readout. The resulting curve is then limited by T_1 instead of T_2 which can be fitted with two frequencies. **b** ESEEM frequency versus external magnetic field. Plotted are frequencies obtained from the two-pulse (blue) and three-pulse (pink) ESEEM. The ESEEM frequency is proportional to the applied magnetic field according to the nuclear Zeeman effect ($\pm\gamma B$), while the offset is given by a quadrupole Q splitting due to surrounding nuclei.

In this case, one expects six frequencies derived from the combination of the Zeeman nuclear and the quadrupole splitting of the surrounding nuclei, as shown in Figure 6.6. Note that additional splitting (with corresponding frequencies) are expected when the ^{10}B ($I = 3$) nuclei are taken into account. Because of experimental limitations, only two of them can be resolved. Figure 6.5b plots a global fit over all T_2 transients measured at different magnetic fields (blue circles). Additional frequency values for other magnetic fields obtained by three-pulse ESEEM (see Figure 6.7) are also shown (pink diamonds), and they complement the field dependence obtained by the two-pulse ESEEM within the error margin (shown in light blue). The ESEEM frequencies evolve linearly with the

magnetic field B following the law $\nu_{\mathrm{ESEEM}} = \mid \nu_0 \pm \gamma B \mid$, where $\gamma = 4.54 \pm 0.59$ kHz/mT and $\nu_0 = 382.9 \pm 4.4$ kHz is the frequency at $B = 0$. In the absence of magnetic field, the nuclear Zeeman splitting is zero, and ESEEM arises only from the nuclear QI and/or HFI [130] and can be used to determine the quadrupole coupling as $Q = \nu_0 = 383$ kHz (Equation 6.1), as shown in Figure 6.7b. The experimentally derived γ is close to the tabulated value of the ^{10}B nuclear gyromagnetic ratio ($\gamma(^{10}B) = 4.575$ kHz/mT); thus, the observed oscillations are possibly due to the coherent coupling of the electron spin with the ^{10}B nuclear spin bath. Note that the coupling of the electron spin V_B^- with the neighbouring ^{14}N nuclear spin with slightly smaller gamma ($\gamma(^{14}N) = 3.076$ kHz/mT) cannot be fully disregarded because it is also within the error margins of the $\nu_{\mathrm{ESEEM}}(B)$ dependence in Figure 6.7b. The three nearest ^{14}N nuclei strongly coupled to V_B^- via hyperfine interaction ($A = 47$ MHz) cannot be excited with the available B_1 field, which is in the range of 0.33 mT because the condition $\gamma_e B_1 > A$, where $\gamma_e = 28$MHz/mT is not fulfilled, and therefore, they cannot be seen in the modulation pattern of the ESEEM. A slight increase in the spin coherence time T_2 with increasing magnetic field (Figure 6.5b) may be due to the partial suppression of heteronuclear or homonuclear spin pair flip-flop processes (cross-resonances) in a moderate magnetic field [131]; however, the nuclear spin bath of the hBN lattice with ^{14}N (99.6 %) (nuclear spin $I = 1$), ^{11}B (80.1 %), and ^{10}B (19.9 %) that have nuclear spin of 3/2 and 3, respectively, remains a major factor of decoherence. Observed ESEEM frequencies clearly show that the electron spin of V_B^- is coherently coupled to nuclear spins in the distant coordination shells from the vacancy, but the exact decoherence mechanism is not understood yet.

6.4.2 Temperature dependence of T_2

An increase of the spin-spin relaxation time at low temperatures can be achieved for many coherent systems [67,132]. For this purpose, the temperature dependence of the T_2 time is examined. Figure 6.8a shows a nearly temperature-independent T_2 time when varying the temperature between 300 and 50 K. Also the observable ESEEM frequencies remain constant within their error bars (see Figure 6.8b). The behavior of temperature-independent T_2 can be attributed to the high defect density in the sample (see Figure 6.9) together with the smallness of the Boltzmann factor to polarize nuclear and electronic spin systems and, thus, to suppress the decoherence in these magnetic field and temperature ranges and is also reported for NV centers in diamond [132] and silicon vacancies in SiC [71].

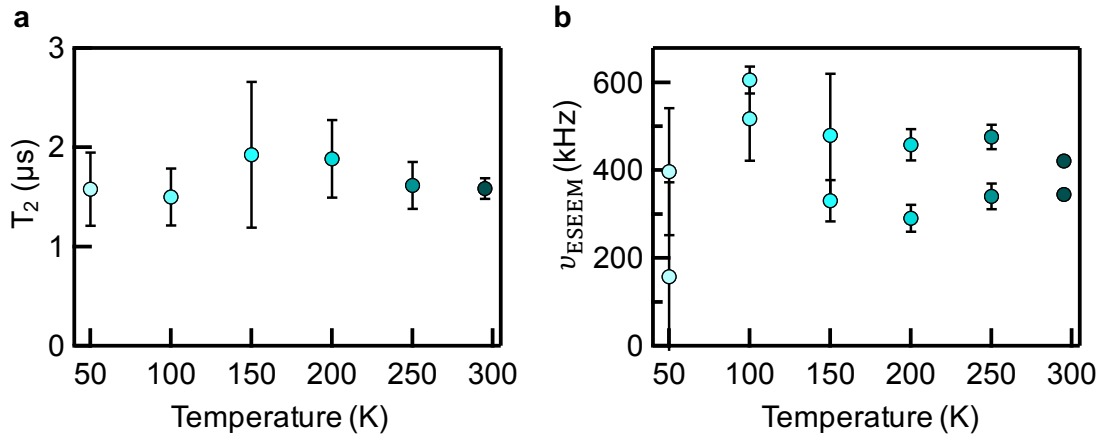

Figure 6.8: Spin-spin relaxation dynamics of V_B^- spin centers in hBN at different temperatures (50 – 300 K. a T_2 time versus temperature at 8.5 mT. **b** ESEEM frequencies extracted from two-pulse ESEEM. T_2 as well as ν_{ESEEM} are almost constant within the error bars.

6.5 Hole-Burning spectroscopy

To further explore the origins of the ODMR line broadening and, hence, the spin--dephasing, a two-frequency cw ODMR technique is applied, which eliminates the contributions of the magnetic nuclei. The so-called "hole-burning" technique[68–71] is realized by introducing a second frequency (pump), which is fixed within the inhomogeneously broadened ODMR line. In Figure 6.10a, a standard cw ODMR spectrum is shown (black curve). Applying a second microwave frequency results in a sharp dip in a particular ODMR transition at the position of the applied frequency. This is shown for three selected resonances at 3.2 GHz (pink), 3.25 GHz (green), and 3.3 GHz (orange), respectively. The pump microwave field excites modes in certain spin packets, and if the power is sufficiently high, then it saturates them, resulting in a reduction in ODMR contrast.

To evaluate the spin hole-burning and extract the "hole" spectrum directly, a selected transition at 3.25 GHz is zoomed in, as shown in Figure 6.10b. The spectral shape of the hole can be fitted by a Gaussian function with a full width at half maximum (FWHM) of 15.5 MHz with a sharp spike in the middle. The linewidth of the broad component is much narrower than the ODMR signal with the linewidth of several hundreds of megahertz due to hyperfine broadening. Thus, by saturating an individual hyperfine transition, the linewidth contribution from magnetic nuclei is eliminated and a spin package separated. As shown in Figure 6.10c, a 500 – kHz frequency sweep around the center of the hole reveals a spike that is perfectly reproducible by two Lorentz functions with

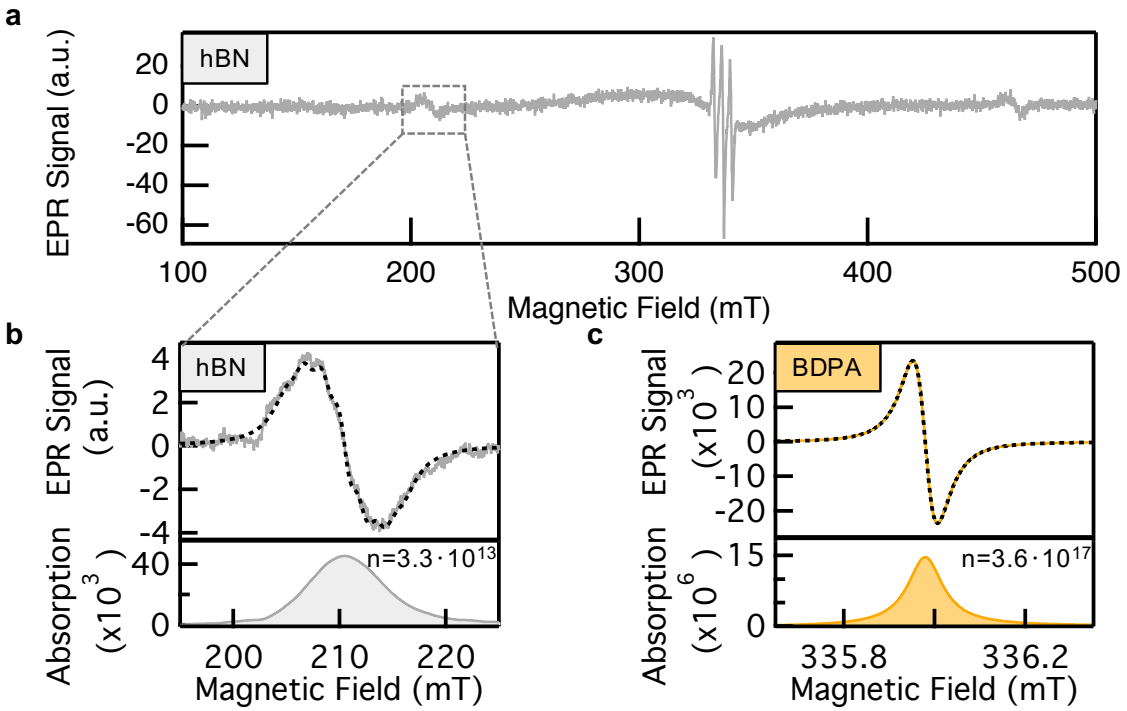

Figure 6.9: Quantitative EPR measurements for defect density determination. **a** Dark X-band EPR spectrum of hBN at $T = 5$ K. The two outer peaks correspond to the V_B^- defect. **b** low-field EPR transition (top) and the integral of the EPR signal (bottom). The absolute spin number n is proportional to the area under the EPR absorption curve. **c** EPR spectrum of a reference sample (BDPA) with a known spin number of $3.6 \cdot 10^{17}$. Taking the EPR settings into account, the obtained absolute number of boron vacancies results in $n = 3.3 \cdot 10^{13}$ which corresponds to the defect density of $N = 5.4 \cdot 10^{17}$ cm^{-3}.

84.7 – kHz (blue) and 25.5 – kHz (yellow) linewidths, respectively. This narrow spike can be explained by coherent population oscillations, where the ground-state population of a two-level quantum system oscillates at the beat frequency between the pump and probe (swept frequency) fields [68–70]. These oscillations can be observed only if the beat frequency is less than, or approximately equal to, the inverse of the population relaxation time. Projecting the spectral hole-burning in optical spectroscopy to the V_B^- spin system, the width of the spike can be related to the population decay rates (relevant spin-relaxation processes) [68,133]. Because there are two contributions to the linewidth, the narrow contribution (25.5 kHz) is assigned to the spin-lattice relaxation rate and extract a T_1^{HB} of 25.0 μs. Consequently, the second contribution (84.7 kHz) is assigned to T_2^{HB} of 7.5 μs. In particular, the spin-spin relaxation time estimated in this way exceeds the value measured directly by pulsed ODMR by a factor of three after the broadening contributions are strongly suppressed by the surrounding nuclear

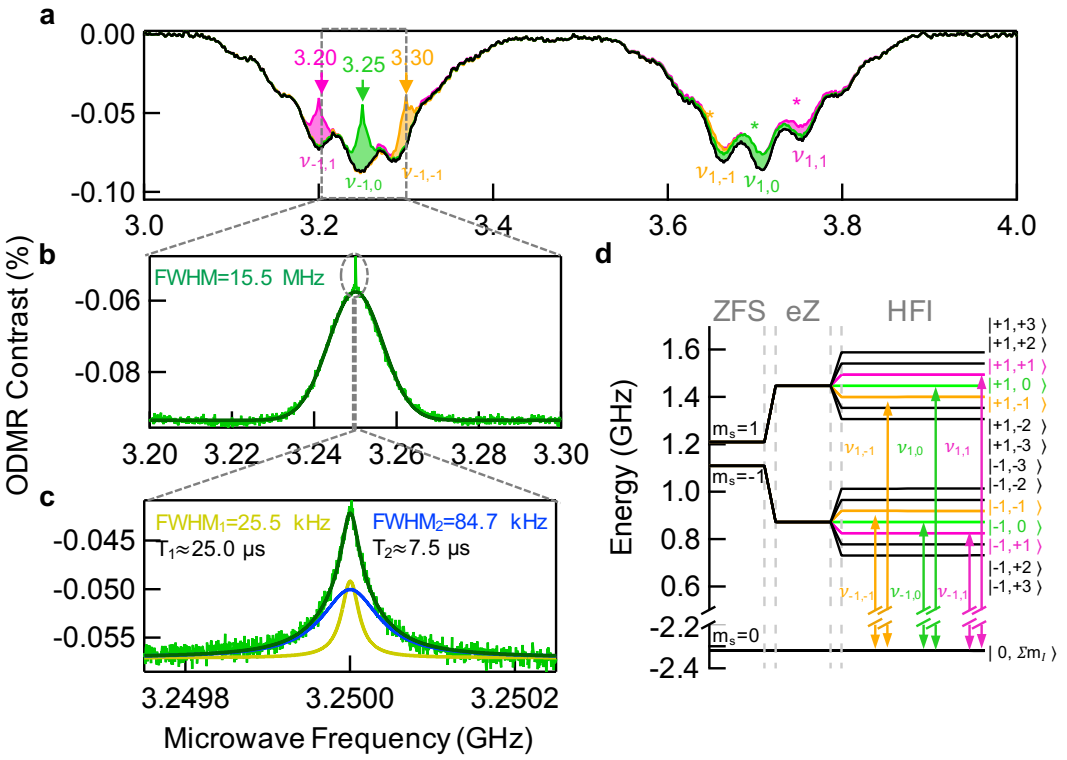

Figure 6.10: Cw multifrequency ODMR measurements at T = 300 K. **a** A standard cw ODMR measurement is plotted in black. The application of a second microwave frequency (pump) leads to a dip (hole) indicated by an arrow (3.20 GHz, pink; 3.25 GHz, green; 3.30 GHz, orange) A second peak (indicated by an asterisk) appears symmetrically to the center of the spectrum (3.48 GHz) for the transitions from $m_S = 0$ to $|-1,-1\rangle$ and $|+1,-1\rangle$ substates, respectively. **b** The hole spectrum. By modulating the fixed (pump) frequency instead of the swept (probe) frequency the pristine hole spectrum can be obtained directly. The signal consists of a broad inhomogeneously broadened Gaussian peak and a very narrow spike on top in the center. **c** The narrow peak is due to coherent population oscillations, it consists of two contributions, and can be fitted with two Lorentz functions (yellow and blue, sum of both in green). The inset shows the respective full width at half maximum (FWHM) and the inverted values assigned to spin-relaxation times T_1 and T_2. **d** Simplified energy diagram illustrating the hyperfine splitting due to three equivalent nitrogen nuclei with the respective electronic and nuclear spin quantum numbers m_S and m_I.

bath and can therefore be regarded as the upper limit for the relaxation rates for V_B^- in hBN at room temperature. Note that the spectral hole is mirrored relative to the ODMR spectrum symmetry axis at $D/h = 3.48$ GHz and also appears in the second ODMR transition ($\sim 3.7-$ GHz range), as indicated by asterisks in Figure 6.10a. To understand this phenomenon, one can use a simplified energy diagram of Figure 6.6 in which only the HFI with three equivalent nitrogen nuclei is considered (see Figure 6.10d). As soon as the pump frequency has saturated the transition, e.g. between the $m_S = 0$ state and the

$|-1,-1\rangle$ substate of $m_S = -1$ state, the hole in the left (low-frequency) ODMR signal is burned. Hence, the state $m_S = 0$ is already depleted and is kept so, therefore, the intensity of the transition to the substate $|+1,-1\rangle$ of the state $m_S = +1$ (high-frequency ODMR signal) will also be lower. This applies to all transitions that correspond to the nuclear spin quantum numbers m_I.

6.6 Conclusion

To conclude, a coherent control of the V_B^- spin ensemble in hBN is demonstrated at room temperature. The results suggest reasonably long spin-relaxation times $T_1 \approx 18$ μs and $T_2 \approx 2$ μs at room temperature that can be substantially increased to $T_1 \approx 12.5$ ms at cryogenic temperatures. The behavior is governed by spin-phonon interaction and follows a power law of $T^{-5/2}$. Using a spin hole-burning technique, the upper limit of the spin-relaxation times is determined to $T_1^{HB} \approx 25.0$ μs and $T_2^{HB} \approx 7.5$ μs at room temperature by suppressing the inhomogeneous broadening due to the surrounding nuclear bath. In addition, the electronic spin system can be further decoupled from the detrimental nuclear bath, as was demonstrated for other 3D systems [134–136], whereby the spin coherence time needs to be seen in relation to other properties depending on the applications [116,137]. The ability to engineer V_B^- defects in thin hBN flakes on demand [77] offers promising perspectives for deploying quantum sensing with vdW crystals. For instance, positioning a monolayer or few layer hBN with embedded V_B^- within a stack of 2D materials can provide an in situ magnetometer to sense the surrounding electromagnetic fields [9,138] or couple the spin to the valley degree of freedom from the surrounding excitons in transition metal dichalcogenides [139].

7 Boron Vacancy as a local Temperature, Pressure and Magnetic Field Sensor

ABSTRACT: Spin defects in solid-state materials are strong candidate systems for quantum information technology and sensing applications. Here the recently discovered negatively charged boron vacancies (V_B^-) in hexagonal boron nitride (hBN) are explored in detail and their use as atomic scale sensors for temperature, magnetic fields and externally applied pressure is demonstrated. These applications are possible due to the high-spin triplet ground state and bright spin-dependent photoluminescence (PL) of the V_B^-. Specifically, the frequency shift in optically detected magnetic resonance (ODMR) measurements is not only sensitive to static magnetic fields, but also to temperature and pressure changes which are related to crystal lattice parameters. This work is important for the future use of spin-rich hBN layers as intrinsic sensors in heterostructures of functionalized 2D materials.

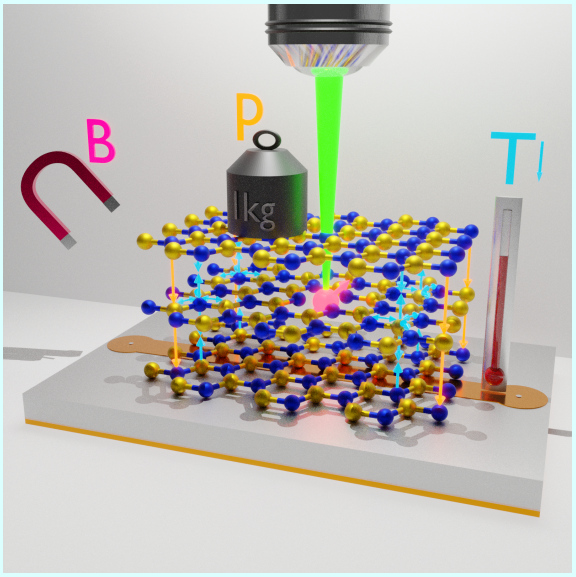

This chapter is based on A. Gottscholl et al. "Spin defects in hBN as promising temperature, pressure and magnetic field quantum sensors", *Nature Communications*, **12** 4480 (2021) [23].

7.1 Introduction

Spin defects in three-dimensional (3D) wide band-gap semiconductors have extensively been utilized in both fundamental and practical realizations in quantum science. The most prominent systems are the nitrogen-vacancy center in diamond [3] and various types of spin defects in silicon carbide (divacancy and silicon vacancy) [117,140]. These systems reveal optically detected magnetic resonance (ODMR), which allows for polarization, manipulation and optical readout of their spin state and consequent mapping of external stimuli (magnetic/electric field, temperature, pressure, etc.) onto it [141–143]. A variety of reports has demonstrated outstanding nanoscale sensing applications of NV-centers (particularly NV^-) in physics and biology including detection of individual surface spins [5] and nanothermometry in living cells [6,7]. However, NV-centers in diamond and spin centers in SiC possess intrinsic limitations. The three-dimensional nature of the material makes it challenging to position the spin-defects close to the sample surface, and thus, to the object/quantity to be sensed. Furthermore, the proximity to the surface deteriorates their spin coherence properties and hinders their sensitivity as nano-sensors [144].

A remedy to these limitations may be provided by recently discovered defects in layered materials. One of the most prominent stackable 2D materials is hexagonal boron nitride (hBN) which hosts a large variety of atom-like defects including single photon emitters [81,85,86,145]. Spin carrying defects have been theoretically predicted and experimentally confirmed in hBN [21,45,47,49,146]. Currently, the most understood defect is the negatively-charged boron vacancy center (V_B^-) [22], which can be readily created by neutron irradiation, ion implantation or femtosecond laser pulses [77,78]. Due to its spin-optical and properties, the V_B^- center is proving to be a promising candidate system for quantum information and nanoscale quantum sensing applications and has thus expanded the already large suite of unique features displayed by 2D materials [81]. The recently identified V_B^- in hBN displays a photoluminescence (PL) emission band around 850 nm and has been found to be an electronic spin-triplet ($S = 1$) system with a ground state zero-field splitting (ZFS) $D_{gs}/h \approx 3.5$ GHz between its spin sublevels $m_s = 0$ and $m_s = \pm 1$ [21]. In this chapter, the effect of external stimuli on the defect's properties is studied and its suitability for sensing temperature, pressure (as lattice compression) and magnetic fields is demonstrated. Notably, these experiments show that the resolution and range of operation of the hBN V_B^- center is competitive or exceeding those of similar defect-based sensors [147].

7.2 Temperature Sensing

The results presented in this chapter were obtained on single-crystal hBN (see Chapter 4.1). The V_B^- centers were generated in the sample via neutron irradiation ($\approx 2.3 \cdot 10^{18}$ n cm^{-2}), as described elsewhere[21,22]. More specifically, the absolute number of V_B^- defects was determined as 10^{13} spins by electron paramagnetic resonance in the dark, giving the defect density of $\approx 5.4 \cdot 10^{17}$ cm^{-3}. Since a neutron irradiation is used, it is assumed that the defects are homogeneously distributed in the sample. The hBN single crystalline sample consists of a stack of a few thousand mono layers. The distance between two identically aligned layers is $c \approx 6.6$ Å, while the in-plane distance between two identical atoms is $a \approx 2.5$ Å (Figure 7.1a). As shown by temperature dependent X-ray data[35], the hBN lattice undergoes highly anisotropic thermal expansion with c and a changing in opposite directions, i.e. while c decreases with cooling, a increases, as schematically shown in Figure 7.1b. This crystallographic feature can be used to monitor local temperature variations optically, via ODMR, since the temperature-driven compression/expansion of the lattice parameters a and c causes a direct change in the ZFS parameter D_{gs} of the triplet ground state[148]. Figure 7.1c shows continuous wave (cw) ODMR measurements for three different temperatures, with (dark blue) or without (cyan) an external magnetic field B applied. At room temperature and in the absence of the external magnetic field, the ODMR spectrum of the V_B^- shows two resonances (ν_1, ν_2) centered symmetrically around ν_0, which corresponds to the ZFS parameter $D_{gs}/h = \nu_0 = 3.48$ GHz with the splitting due to the non-zero off-axial ZFS parameter $E_{gs}/h = \nu_0 = 50$ MHz When applying an external static magnetic field B, ν_1 and ν_2 split further following:

$$\nu_{1,2} = D_{gs}/h \pm 1/h\sqrt{E_{gs}^2 + \left(g\mu_B B\right)^2} \tag{7.1}$$

Here, h is Planck's constant, g is the Lande factor and μ_B is the Bohr magneton. The separation of the two resonances ν_1 and ν_2 can clearly be seen in Figure 7.1c (dark blue traces). The visible substructure in both ODMR peaks is due to hyperfine coupling of the electron $S = 1$ spin system (negatively charged boron vacancy) with three equivalent nearest nitrogen atoms, each possessing nuclear spin $I = 1$ for the most abundant ^{14}N isotope (99.63 %). In total, seven hyperfine peaks can be resolved, whose relative separations are temperature and magnetic field independent. A closer look at Figure 7.1c reveals that cooling down the sample results in a shift of the ODMR peaks to higher frequencies. Thus, the dependencies of the ODMR spectrum on temperature and magnetic fields can provide a basis for the use of the V_B^- center as a thermometer and magnetometer at the nanoscale.

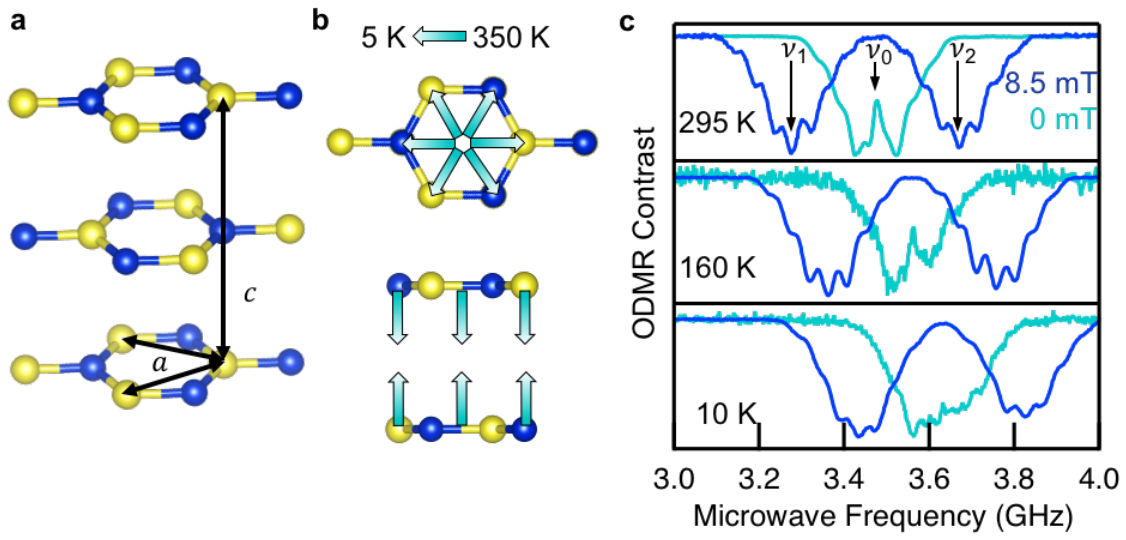

Figure 7.1: Temperature dependence of hexagonal boron nitride. a Schematic of the hBN crystal, its hexagonal structure with alternating boron (yellow) and nitrogen (blue) atoms and the lattice constants a and c. **b** Lattice contraction and expansion due to temperature variation, according to crystallographic data [35]. **c** Cw ODMR spetra measured with (dark blue) and without (cyan) external magnetic field at different temperatures $T = 295$ K, 160 K and 10 K. Lowering of the temperature causes the resonances ν_0, ν_1 and ν_2 to shift to larger microwave frequencies indicating an increase of the zero-field splitting D_{gs}

7.2.1 Temperature induced ZFS Shift

The observed shift of the resonances to higher frequency values (Figure 7.1c) is independent of the applied magnetic field and is solely due to a increasing of the ZFS parameter D_{gs}. Over the temperature range 295–10 K, D_{gs} undergoes a variation $\Delta D_{gs} \approx$ 195 MHz. This is a relatively large change compared to analogous spin systems in 3D materials ($\approx$ 30-fold). For instance, the NV^- center in diamond exhibits a shift $\Delta D_{gs} \approx 7$ MHz [148], while the D_{gs} of V_{Si} in SiC is almost constant over the same range. Only more complex spin defects such as Frenkel defects ($V_{Si} - Si_i$) in SiC display a comparably strong effect ($\Delta D_{gs} \approx 300$ MHz) [142].

To quantify this temperature-induced shift of the ground state triplet energy-levels temperature- and magnetic field-dependent ODMR measurement are combined. Figure 7.2 summarizes the shift of D_{gs} in the ODMR spectrum as a function of temperature both, in the presence (a) and absence (b) of an external magnetic field. In Figure 7.2a, an external magnetic field of 8.5 mT is applied. A monotonic, nearly linear increase of the resonance frequencies associated to a change in the zero-field splitting parameter D_{gs} can be observed for temperatures down to 50 K. Zero-field ODMR (Figure 7.2b) shows the same behavior. The ZFS values D_{gs}/h are now extracted from

Figure 7.2a, b and plotted against temperature (Figure 7.3a). Both temperature dependencies, represented by dark blue and cyan diamonds, match perfectly and thus confirm that the temperature scaling of D_{gs} is indeed independent of the magnetic field.

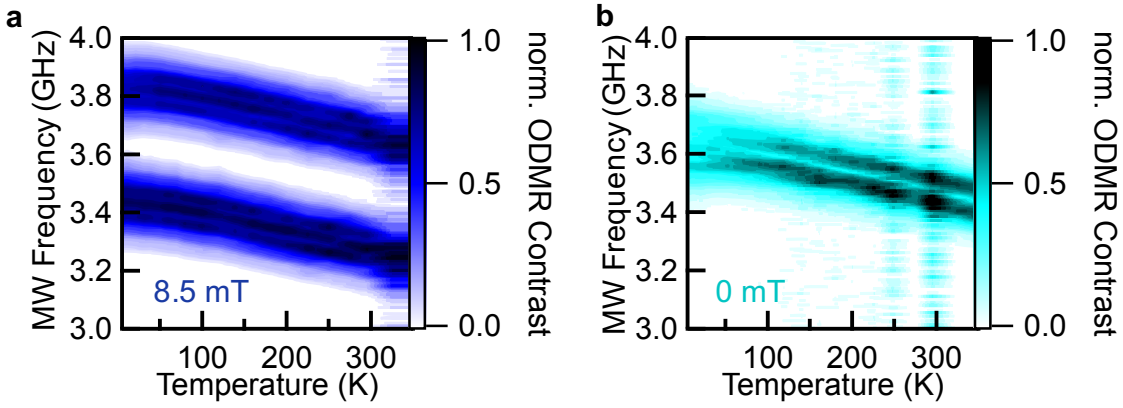

Figure 7.2: Temperature dependence of the ODMR spectrum of V_B^-. **a** Color map represents the peak positions of the normalized ODMR spectrum for different temperatures in an external magnetic field of $B = 8.5$ mT. **b** The same color map representation of the peak positions but without an external magnetic field.

7.2.2 Model of ZFS and Lattice Parameters

The temperature dependency can be explained by considering the change in the delocalization of the spin-defect wave function due to temperature-induced structural deformations of the crystal lattice. This is consistent with e.g. the case of the NV^- center in diamond[148,149]. The latter shows a linear behavior for the shift of the ZFS associated to the relative change of the lattice constant η[149] $\Delta D_{gs}(\eta)/h = \theta\eta(T)$, where θ is the proportionality factor, explicitly written as $dD/d\eta$ and $\eta(T)$ is the relative change of the lattice parameter. Applying the same concept to hBN with its two lattice parameters a and c results in the equation:

$$D_{gs}(T) = D_{gs}(295\text{ K}) + \theta_a\eta_a(T)h + \theta_c\eta_c(T)h \tag{7.2}$$

Here, D_{gs}/h is the experimentally measured ZFS frequency. $D_{gs}(295\text{ K})/h = 3.48$ GHz is the ZFS at $T = 295$ K that is chosen as reference, and $\eta_a(T)$, $\eta_c(T)$ are relative changes of a and c, respectively (see also Equations 7.6 and 7.7 below). The temperature-dependent lattice parameters $a(T)$ and $c(T)$ for hBN were determined in Ref.[35] and are plotted in Figure 7.3b in addition to the ODMR data. The proportionality factors θ_a and θ_c are the significant parameters that connect lattice deformation and ZFS and will be derived from the experimental data in the following. To do so, Equation 7.2 is fitted to

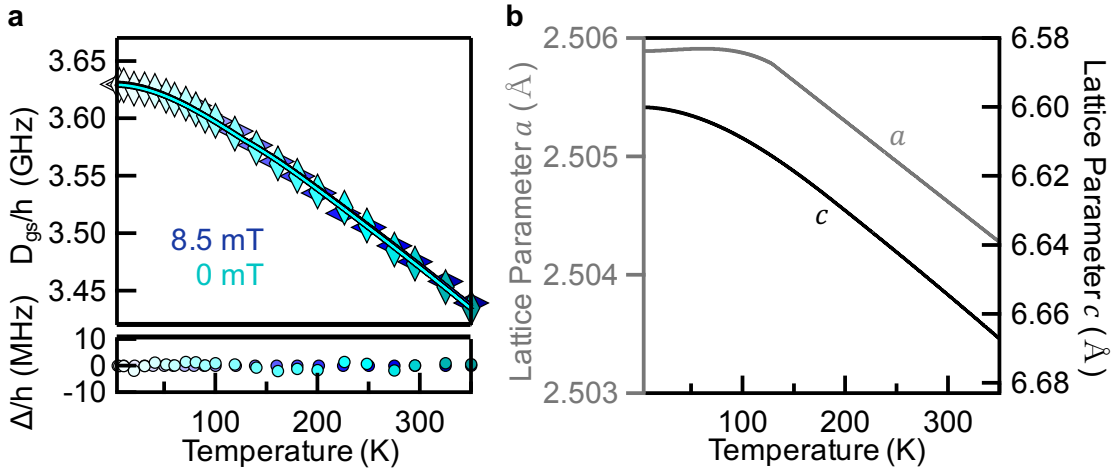

Figure 7.3: Comparison of temperature dependence of lattice parameters and ZFS behaviour. **a** ZFS parameter D_{gs}/h obtained from 7.2 a (blue diamonds) and b (cyan diamonds) vs. temperature. The monotonic increase while lowering the sample temperature is unaffected by the magnetic field. The data can be fitted using Equation 7.2 describing the temperature-dependent change of the lattice parameters a (gray line[35]) and c (black line[35]) that are plotted in b. The fits are shown as solid lines (blue for 8.5 mT and cyan for 0 mT) on top of the diamonds and reproduce the temperature dependence perfectly. The difference between measurement and fit (Δ/h) is shown in the bottom panel. **b** Lattice parameters extracted from[35].

the experimentally measured ZFS D_{gs}, as shown in Figure 7.3 a. The fit perfectly reproduces the experimental data, which highlights the remarkable linear response of the resonance frequency to changes of the lattice constants in this case due to temperature. More specifically, the maximum error between the polynomial function and the measured data is < 5 MHz, which is within the measured data scatter. Figure 7.3a (bottom panel) shows the difference between the fit and the measured data.

Figure 7.4 shows the relationship between temperature-dependent lattice parameters and ZFS by combining the three separate functions ($a(T)$, $c(T)$ and $D_{gs}(T)$) of Figure 7.3b in one plot. By inserting the crystallographic data for the hBN lattice parameters[35] (Figure 7.3b) into Equation 7.2, partial shifts of the ZFS $\Delta D_{gs,a}$ and $\Delta D_{gs,c}$ are obtained with respective slopes θ_a and θ_c, as shown in Figure 7.5b, c. This enables the extraction of the values for θ_a of (-84 ± 15) GHz and (-78.2 ± 8.8) GHz or θ_c of (-24.32 ± 0.59) GHz and (-24.6 ± 1.0) GHz at $B = 0$ mT and 8.5 mT, respectively. The out-of-plane θ_c can be determined more precisely, since the relative change of lattice parameter c is one order of magnitude larger.

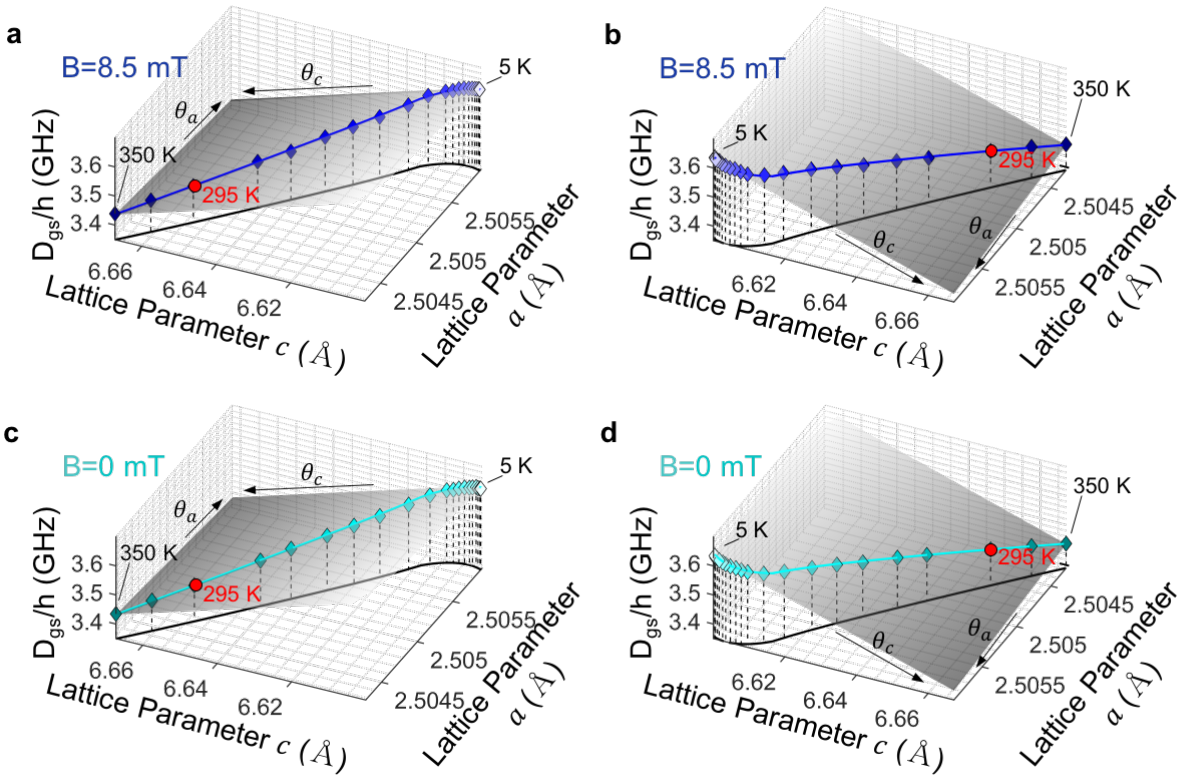

Figure 7.4: Zero-field splitting dependence on the lattice parameters a and c. Equation 7.2 is fitted (solid lines) to the experimental data displayed as diamonds. The ZFS reference temperature $T = 295$ K is marked by a red dot. The assignment of colors of fitting lines (blue for 8.5 mT and cyan for 0 mT) is the same as in Figure 7.3. **a**,**b** Combined 3-dimensional representation with the slopes θ_a and θ_c (shown also in Figure 7.5b, c) for the dataset with magnetic field ($B = 8.5$ mT).**b** is rotated by 180° relative to **a**. **c**,**d** Combined 3-dimensional representation for the dataset without external magnetic field ($B = 0$ mT).**d** is rotated by 180° relative to **c**.

The values coincide within the experimental error and can be combined as:

$$\theta_a = (-81 \pm 12)\ \text{GHz} \tag{7.3}$$

$$\theta_c = (-24.5 \pm 0.8)\ \text{GHz} \tag{7.4}$$

Remarkably, the ratio $\theta_a/\theta_c \approx 3.3$, which means the influence of the lattice distortion on the ZFS in-plane is at least three times stronger than the influence of the interplanar distance on the same, indicating a localization of the V_B^- spin density in the plane as predicted by the theory[49].

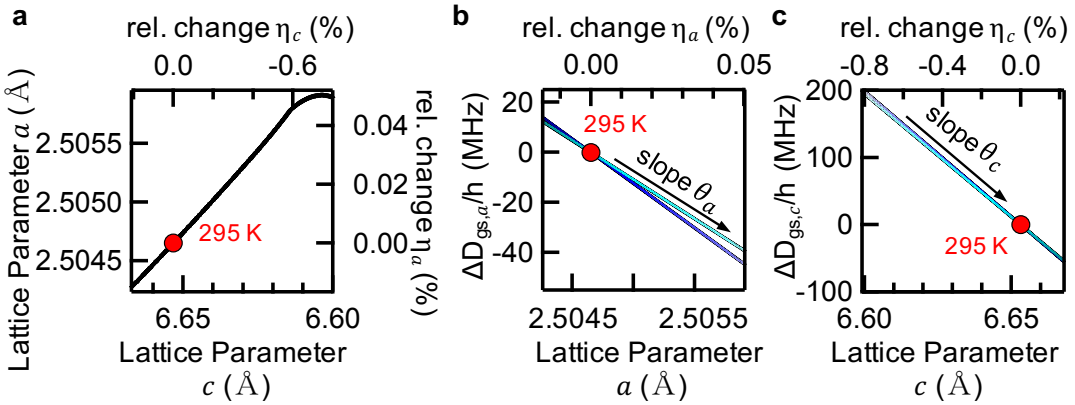

Figure 7.5: Zero-field splitting contribution of the lattice parameters a and c. **a** Comparison of the lattice parameters in the temperature range 5 – 350 K. **b** Change of the ZFS $\Delta D_{gs,a}$ caused by temperature-dependent lattice parameter a. **c** Change of $\Delta D_{gs,c}$ caused by the temperature-dependent lattice parameter c.

Finally, a polynomial is proposed which allows a direct determination of D_{gs} from the sample temperature T:

$$D_{gs}(T) = h\sum_k A_k T^k (k = 0,1,2,3) \tag{7.5}$$

where T is the temperature, h is Planck's constant, k is an integer, and the polynomial coefficients A_k are summarized in Table 7.2 for different temperature ranges. To obtain the coefficients A_k, the essential step is to determine the relative changes of the lattice parameters from the crystallographic data [35] by using the Equations 7.6 and 7.7:

$$\eta_a(T) = \frac{a(T) - a(295\ \mathrm{K})}{a(295\ \mathrm{K})} \tag{7.6}$$

$$\eta_c(T) = \frac{c(T) - c(295\ \mathrm{K})}{c(295\ \mathrm{K})} \tag{7.7}$$

To assess the heating effect induced by the laser, ODMR spectra at different laser powers between 200 and 1000 mW are measured. An overall shift of < 10 MHz due to laser heating is observed. The data is shown in Figure 7.6a,b. The observed effect is negligible for other measurements, since all other measurements presented in this chapter were performed with laser power < 100 mW. To estimate the heating induced by the microwaves, ODMR spectra at different microwave power between 0.03 and 3 W are measured at room temperature (ambient laboratory conditions). This data is summarized in Figure 7.6c,d. A change of the ZFS of about 5 MHz is observed, which corre-

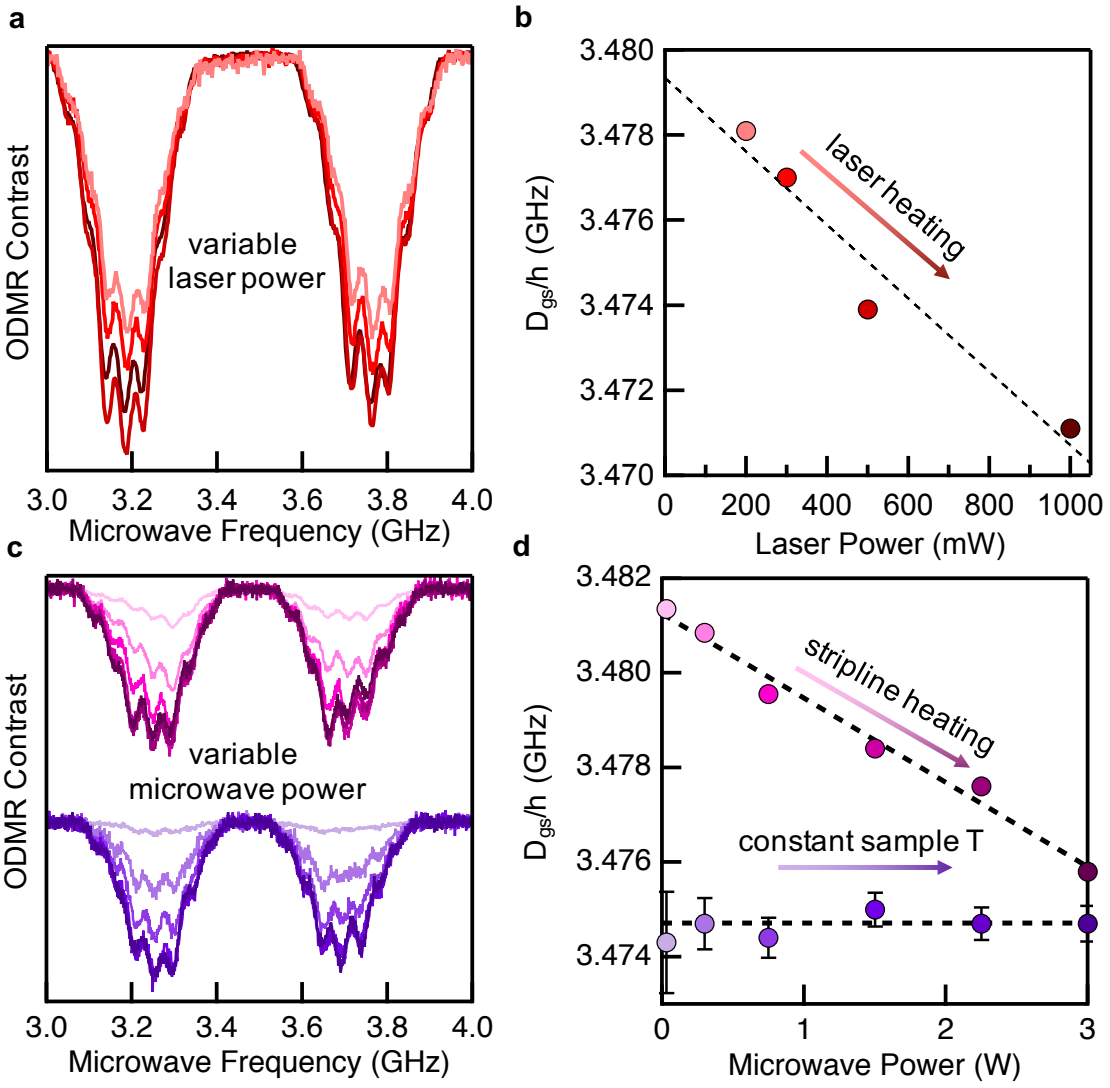

Figure 7.6: Influence of laser power and microwace power on the ODMR signal. **a** Cw ODMR signals for different laser powers. **b** Change of the ZFS parameter D_{gs}/h as a function of the applied laser power. A total shift of < 10 MHz due to laser heating is observed. This effect can be neglected for other measurements, since all other measurements presented in this work were performed with laser powers < 100 mW.**c** Cw ODMR signal at room temperature (pink) and for a temperature stabilized stripline at T = 300 K (purple) for different microwave powers. The spectra without temperature stabilization (pink) are shifted towards lower frequencies for higher microwave powers. **d** Change of the ZFS parameter D_{gs}/h as a function of the applied microwave power. A total shift of 5 MHz due to the resistive heating of the stripline is observed (pink speres). However, the local temperature (purple spheres) remains unaffected.

sponds to a heating of 10 K (pink symbols). However, the main effect can be assigned to the resistive heating of the stripline and not to the power absorbed by the spin system in resonance. The two effects can be separated by a precise measurement in a stabi-

lized cryo-system (shown in purple). The local sample temperature is constant within the error bars, which means that the resonant absorbed microwaves have very little or no influence on the temperature dependent ZFS in this microwave power range.

7.3 Pressure Sensing

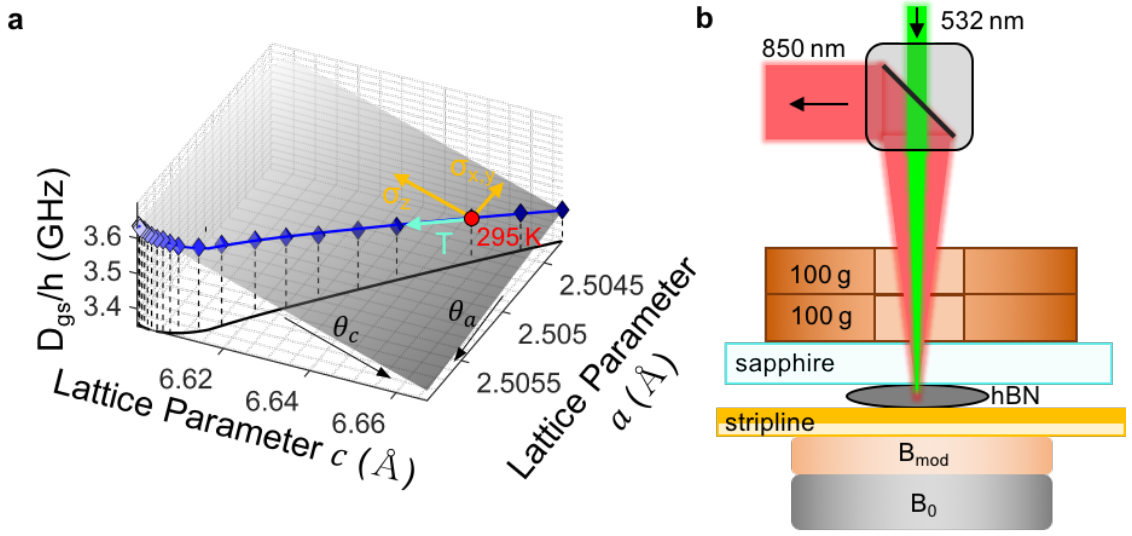

Figure 7.7: Pressure sensing with V_B^-. a A three-dimensional representation of the parameter space (see Figure 7.4b) according to the linear model. The blue curve shows the lattice parameters and therefore the ZFS dependence given by heating/cooling the sample. External pressure in z-direction (c) or x,y-direction (a) also results in a shift. **b** Modified setup for pressure sensing: weights (e.g. 100 g) are pressing on a transparent sapphire substrate applying a pressure on the sample. A copper wire coil is placed between stripline and external offset magnetic field in order to perform a magnetic field modulation for a high S/N.

The observation that a temperature-induced change in the lattice parameters directly results in a shift of the ZFS D_{gs} leads to the consideration of utilizing the V_B^- center also as a sensor, for externally applied in-plane or out-of-plane pressure. The basic idea is illustrated in Figure 7.7. Figure 7.7a shows the extracted linear model where a ZFS shift due to a change of the temperature can be explained by moving on the blue curve. An external pressure enables an arbitrary movement on the surface in c-direction (external pressure in z, see Figure 7.7b) and in a-direction (external pressure in x,y) resulting in different ZFS values.

7.3.1 Theoretical Calculations

For a first-order estimation an isothermal system is assumed without shear strain and derive the perspective sensitivity based on reported elastic moduli for hBN crystals [150,151]. In cartesian coordinates, the pressure vector σ_{xyz} is given by the elastic moduli tensor

C multiplied with the relative change of the lattice parameters η_{xyz}:

$$\begin{pmatrix}\sigma_x\\ \sigma_y\\ \sigma_z\end{pmatrix} = \begin{pmatrix}C_{11} & C_{12} & C_{13}\\ C_{12} & C_{11} & C_{13}\\ C_{13} & C_{13} & C_{33}\end{pmatrix}\begin{pmatrix}\eta_x\\ \eta_y\\ \eta_z\end{pmatrix} \tag{7.8}$$

The reported elastic moduli for hBN are: $C_{11} = (811 \pm 12)$ GPa, $C_{12} = (169 \pm 24)$ GPa, $C_{13} = (0 \pm 3)$ GPa and $C_{33} = (27 \pm 5)$ GPa[150]. The hBN lattice parameters a and c are oriented along the y- and z-direction, respectively. This simplifies Equation 7.8 by incorporating $\eta_{a,c}$ and removing C_{13}, which is 0:

$$\begin{pmatrix}\sigma_x\\ \sigma_y\\ \sigma_z\end{pmatrix} = \begin{pmatrix}\eta_a\left(\frac{2}{3}C_{11} + \frac{1}{3}C_{12}\right)\\ \eta_a\left(\frac{2}{3}C_{12} + \frac{1}{3}C_{11}\right)\\ \eta_c C_{33}\end{pmatrix} \tag{7.9}$$

This can be rewritten to obtain $\eta_{a,c}$ directly:

$$\eta_a = \frac{\sigma_x}{\frac{2}{3}C_{11} + \frac{1}{3}C_{12}} = \frac{\sigma_y}{\frac{2}{3}C_{12} + \frac{1}{3}C_{11}} \tag{7.10}$$

$$\eta_c = \frac{\sigma_z}{C_{33}} \tag{7.11}$$

Substituting these relationships into Equation 7.2 yields the ZFS as a function of the applied pressure:

$$\begin{aligned} D_{gs}(\sigma_x, \sigma_y, \sigma_z) &= D_{gs,295\text{ K}} + \Delta D_{gs,x} + \Delta D_{gs,y} + \Delta D_{gs,z} \\ &= D_{gs,295\text{ K}} + \frac{\theta_a \sigma_x h}{\frac{2}{3}C_{11} + \frac{1}{3}C_{12}} + \frac{\theta_a \sigma_y h}{\frac{2}{3}C_{12} + \frac{1}{3}C_{11}} + \frac{\theta_c \sigma_z h}{C_{33}} \end{aligned} \tag{7.12}$$

Based on these estimates for $\theta_{a,c}$ in Equations 7.3 and 7.4 and the reported elastic moduli[150], the sensitivity to measure the ZFS shifts for each direction of the applied pressure can be obtained:

$$\Delta D_{gs_x} = \sigma_x h(-0.136 \pm 0.028)\ \frac{\text{Hz}}{\text{Pa}} \tag{7.13}$$

$$\Delta D_{gs_y} = \sigma_y h(-0.212 \pm 0.052)\ \frac{\text{Hz}}{\text{Pa}} \tag{7.14}$$

$$\Delta D_{gs_z} = \sigma_z h(-0.91 \pm 0.20)\ \frac{\text{Hz}}{\text{Pa}} \tag{7.15}$$

Consequently, the ZFS shift $\Delta D_{gs,xyz}$ is directly associated with external compression of the hBN lattice and therefore V_B^- can be utilized as a pressure sensor. Remarkably, the out-of-plane sensitivity along the c-axis is much higher due to the small C_{33} coefficient. This makes this type of sensor particularly useful to measure vertical indentation in 2D heterostructures.

7.3.2 External Pressure in z-Direction

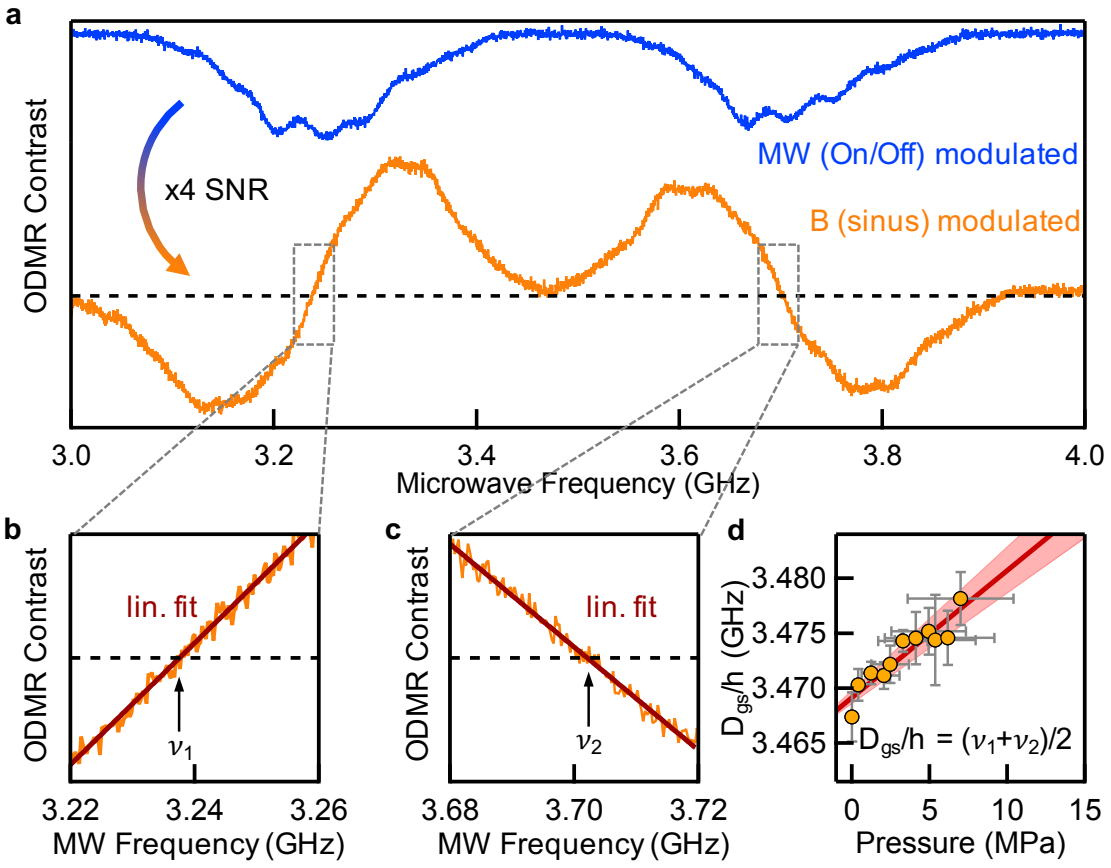

Figure 7.8: Pressure dependence of the zero-field splitting parameter D_{gs}/h. **a** ODMR spectra of V_B^- with microwave modulation (on/off) (blue) and sinusoidal magnetic field modulation (orange). The partially resolved hyperfine peaks are blurred due to an intentional overmodulation of the spectrum that allows a linear fit in the vicinity of the zero-crossings for a precise determination of the resonant transitions ν_1 (**b**) and ν_2 (**c**) and therefore the parameter D_{gs}/h. **d** D_{gs}/h as a function of pressure, follows a slope of $(1.16 \pm 0.15)\ Hz/Pa$ which is close to the expected value $(0.91 \pm 0.20)\ Hz/Pa$ according Equation 7.15.

To verify the above considerations, pressure-dependent experiments are performed. Pressure is applied in the c-direction of the hBN lattice by stacking weights on the sample (see Figure 7.7b).

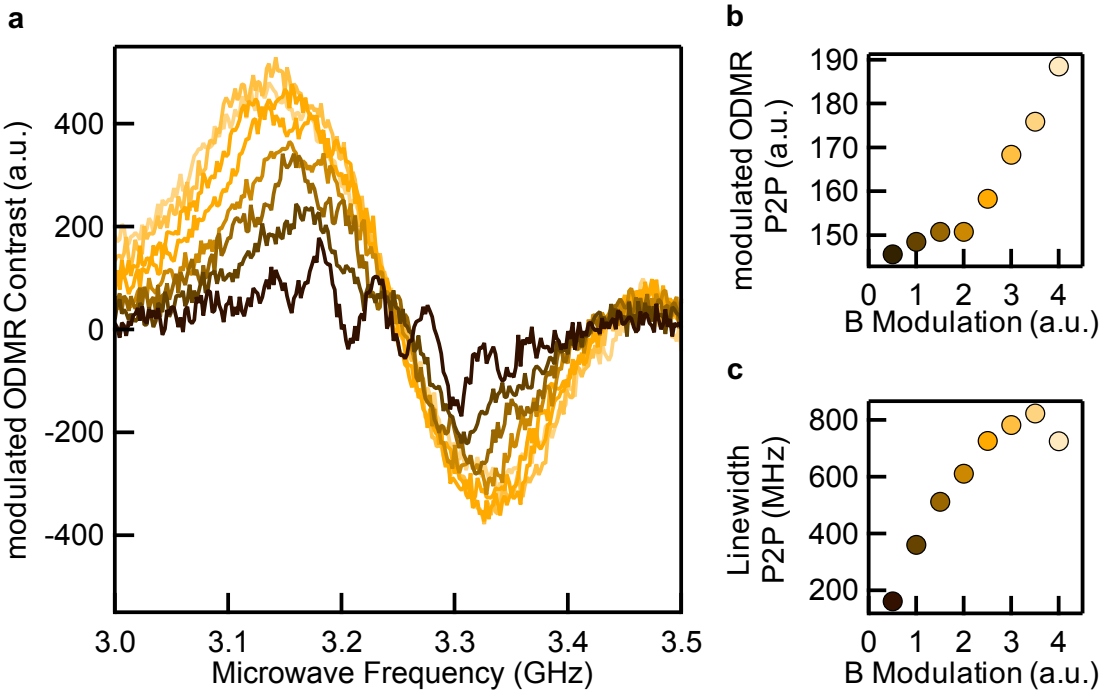

Figure 7.9: Influence of the magnetic field modulation on the ODMR spectra. **a** A magnetic field modulation leads to the first derivative of the standard cw ODMR signal. **b** The peak-to-peak amplitude can be enhanced by increasing the magnetic field modulation. **c** The overmodulation results in line broadening of the signal.

To improve the sensitivity, sinusoidal modulation are applied to the static B-field instead of amplitude modulation (on/off) of the microwave while sweeping the frequency. The results are shown in Figure 7.8. The sine-wave modulation of the B-field yields the first derivative of the spectrum (see Figure 7.9 for the modulation behavior of the spectrum), which increases the signal-to-noise ratio by a factor of four (Figure 7.8, orange). For an accurate determination of the resonant transitions ν_1 and ν_2 and their shift with the applied pressure, the spectra were linearly fitted near the zero crossings, as shown in zoomed-in Figure 7.8b and c. The resulting pressure dependence of the parameter $^{D_{gs}}/_{h}$ is shown in Figure 7.8d. The experimentally determined slope of (1.16 ± 0.15) $^{Hz}/_{Pa}$ is close to the theoretically expected slope (0.91 ± 0.20) $^{Hz}/_{Pa}$ according to Equation 7.15. As shown in Figure 7.10, the method can also be potentially used to study local and temperature-induced strains in the sample by measuring the off-axis ZFS parameter E_{gs}. However, the sample in this work reveals no changes in E_{gs} neither at different temperatures nor at different position in the crystal.

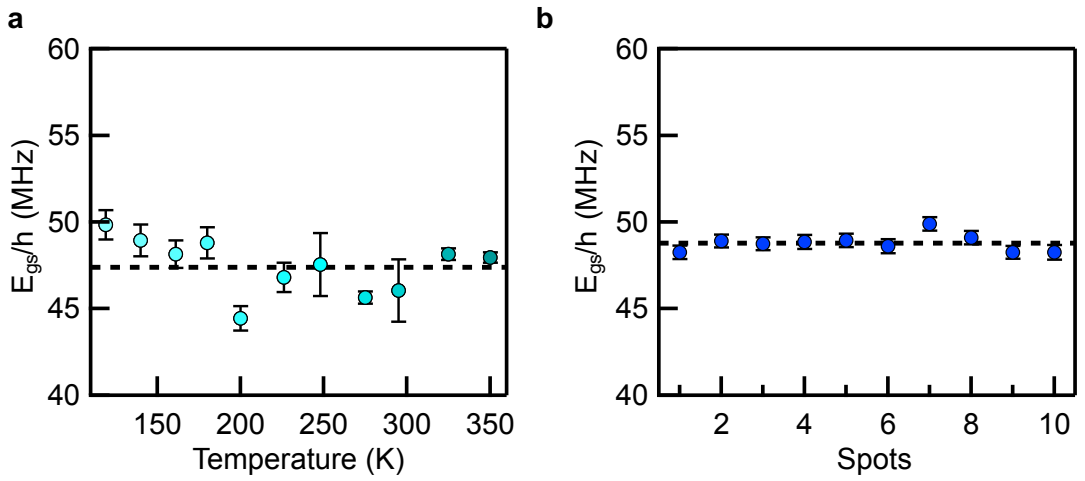

Figure 7.10: Off-axial zero-field splitting term E_{gs}/h. b E_{gs}/h measured at different sites on the sample. The E_{gs}/h values are scattered around 49 MHz, but without a clear trend. **b** E_{gs}/h measured at different temperatures (110 – 350 K).

7.4 Magnetic Field Sensing

As shown in Figure 7.2a, the two resonant transitions $\nu_{1,2}$ are equally separated with respect to ν_0 over the entire temperature range between 5 K and 350 K. It should be pointed out that the magnetic field sensing is based on the g-factor, which is independent of the lattice parameters. In Figure 7.11, the principle suitability of a V_B^- center in hBN for magnetic field sensing is demonstrated, where the resonant microwave transitions ν_1 and ν_2 are shown over a broad range (0 – 3500 mT) and exemplarily simulated for two distant temperatures, $T = 295$ K (dark blue) and $T = 5$ K (light blue). For a magnetic field applied in the c-direction of the hBN lattice, the behavior can be described with Equation 7.1. Due to the non-zero off-axis E_{gs}, the Zeeman splitting term $g\mu_B B$ leads to a linear regime only for $B > 3$ mT, when the applied magnetic field is large enough to separate the two otherwise partially overlapping $\nu_{1,2}$ transitions.

To extend the magnetic field range of the measurements beyond the confocal ODMR setup limit of ≈ 20 mT, continuous wave electron paramagnetic resonance (cw EPR) and electron spin-echo detected (ESE) EPR is applied (Figure 7.11b). The advantage is that the cw EPR measurements are performed at a microwave frequency of 9.4 GHz (X-band) (light green diamonds) and the ESE EPR measurements at a microwave frequency of 94 GHz (W-band) (dark green diamonds) which allow extending the magnetic field range to 3500 mT. The multifrequency spin resonance approach enables us to determine the g-factor with extremely high accuracy as $g = 2.0046 \pm 0.0021$.

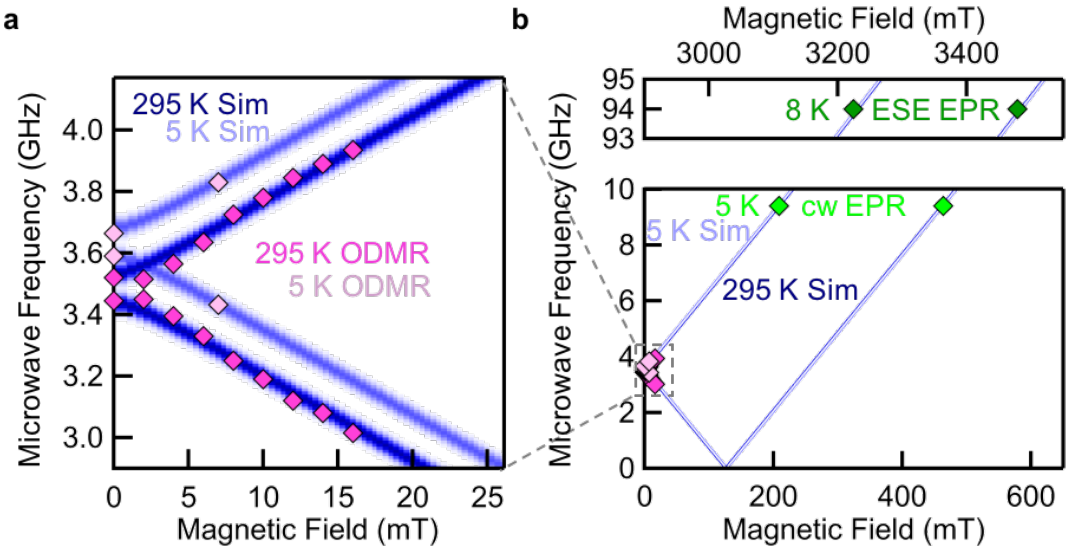

Figure 7.11: Experimental (diamonds) and simulated (dark and light blue traces) resonant frequencies of V_B^- for different temperatures and magnetic fields. **a** ODMR measurements (pink diamonds) at $B < 20$ mT. **b** A cw EPR measurement at $T = 5$ K and microwave frequency of 9.4 GHz (light green) and electron spin-echo detected EPR measurements at $T = 8$ K and 94 GHz (dark green). Note the axes are shifted for better visibility and comparability.

7.5 Sensor Resolution: Discussion and Comparison

As mentioned, one of the crucial parameters for high-sensitivity sensing is the distance between the sensor and the object to be sensed. In this regard, sensors based on the hBN V_B^- center are particularly appealing as - based on the presented model of lattice constant variations - the required hardware ideally consists of only three hBN layers, with the intermediate one hosting a V_B^- center. This corresponds to a minimum distance of the defect to the surface in the sub-nanometer range of ≈ 0.33 nm. A further thickness reduction, e.g. to a single monolayer, would indeed eliminate the interlayer contribution $c(T)$, but make the sensing effect completely dependent on the interaction of the V_B^- wave function with the parameters of the adjacent material. For single layers, $D_{gs,295\,\mathrm{K}}$ would differ from the theoretical calculation[49], and a calibration would be required to determine the set of parameters ($D_{gs,295\,\mathrm{K}}$, θ_a, θ_c) specific for the adjacent material. To substantiate this hypothesis, however, further measurements and calculations must be carried out.

In the following, the properties of the hereby proposed sensor based on V_B^- centers in hBN is benchmarked against other defect-based sensors in silicon carbide and diamond. For this purpose, the general sensitivity is derived, which includes the re-

spective coupling coefficient $\Gamma_{T,\sigma,B}$ representing the sensitivity of the ODMR frequency shift due to the corresponding external influence, and the general resolution in relative change of frequency in relation to acquisition time and noise level [142]. An overview of all calculated coupling coefficients and resolutions is summarized in Table 7.1.

	Γ_{hBN}	Γ_{diamond}	Γ_{SiC}	$\delta^{295\text{ K}}_{\text{hBN}}$	$\delta^{295\text{ K}}_{\text{diamond}}$	$\delta^{295\text{ K}}_{\text{SiC}}$	$\delta^{50\text{ K}}_{\text{hBN}}$
B	$28.0\,\text{kHz}/\mu\text{T}$	$28.0\,\text{kHz}/\mu\text{T}$	$28.0\,\text{kHz}/\mu\text{T}$	$85.1\,\mu\text{T}/\sqrt{\text{Hz}}$	$3\,\text{nT}/\sqrt{\text{Hz}}$	$10\,\mu\text{T}/\sqrt{\text{Hz}}$	$4.33\,\mu\text{T}/\sqrt{\text{Hz}}$
T	$-623\,\text{kHz}/\text{K}$	$-74\,\text{kHz}/K$	$-1.1\,\text{MHz}/\text{K}$	$3.82\,\text{K}/\sqrt{\text{Hz}}$	$0.76\,\text{mK}/\sqrt{\text{Hz}}$	$1\,\text{K}/\sqrt{\text{Hz}}$	$0.19\,\text{K}/\sqrt{\text{Hz}}$
σ_x	$-0.136\,\text{Hz}/\text{Pa}$			$17.5\,\text{MPa}/\sqrt{\text{Hz}}$			$0.891\,\text{MPa}/\sqrt{\text{Hz}}$
σ_y	$-0.212\,\text{Hz}/\text{Pa}$			$11.2\,\text{MPa}/\sqrt{\text{Hz}}$			$0.572\,\text{MPa}/\sqrt{\text{Hz}}$
σ_z	$-0.91\,\text{Hz}/\text{Pa}$			$2.62\,\text{MPa}/\sqrt{\text{Hz}}$			$0.133\,\text{MPa}/\sqrt{\text{Hz}}$

Table 7.1: Three spin hosting systems in comparison: coupling coefficient Γ and general resolution δ at room (T = 295 K) and cryogenic (T = 50 K) temperatures calculated for magnetic field B, temperature T and pressure σ. Also shown are the reference values for spin defects in diamond [144,152,153] and SiC [142], respectively (see main text).

In order to facilitate comparison with other color centers in 3D materials, first a linear regime (50 − 350 K) is considered in the analysis. In this range, a proportionality between ΔD_{gs} and T is given by the factor $\Gamma_T = {}^{\Delta D_{gs}}/_{\Delta T} = -623$ kHz/K. This value is almost one order of magnitude (> 8-fold) larger than the corresponding factor for NV^- centers in diamond (-74 kHz/K) [154]. This remarkable difference is in particular due to the larger relative change of the lattice parameters as a function of temperature in hBN, while θ is of the same order of magnitude. For NV^- centers, a value of $\theta_{NV} = -14.41$ GHz is reported [149], which is comparable to $\theta_c \approx -24$ GHz for V_B^- in hBN. Note that θ_a can be neglected here, since on the one hand the relative change of the lattice parameter a is negligible and on the other hand it counteracts the effect due to the expansion of the in-plane distance while cooling the sample. Interestingly, for temperatures below ≈ 50 K, the quantity D_{gs} remains almost constant in NV^- centers in diamond [155], which limits their operating range. Conversely, ${}^{D_{gs}}/_h$ in V_B^- centers maintain a measurable temperature dependence well-below 50 K, down to a few K (see Figure 7.3a). A ${}^{dD_{gs}}/_{dT}(T = 10\text{ K}) = -87$ kHz/K is estimated for hBN, while ${}^{dD_{gs}}/_{dT}(T = 10\text{ K})$ in the NV-diamond is in the range of $-7 \cdot 10^{-2}$ kHz/K [155], i.e. three orders of magnitude smaller. This is particularly intriguing for applications that require monitoring temperature changes, with high spatial resolution, in cryogenic conditions. The general resolution $\delta_T^{295\text{ K}}$ obtained at room temperature is approximately 3.82 $\text{K}/\sqrt{\text{Hz}}$ which is of the same order of magnitude as defect-based temperature sensors in SiC (1 $\text{K}/\sqrt{\text{Hz}}$) using the same cw ODMR set-up [142]. It should be noted, however, that at cryogenic temperatures the resolution of the V_B^- center is enhanced by a factor of ≈ 20 ($\delta_T^{50\text{ K}} = 0.19\ \text{K}/\sqrt{\text{Hz}}$), as both the ODMR contrast ${}^{\Delta\text{PL}}/_{\text{PL}}$ and the PL intensity increase, which significantly reduces the required measurement time. Despite the smaller coupling coefficient, a temperature

sensor based on NV's in diamond is still more sensitive (0.76 $^{mK}/\sqrt{Hz}$) [153], mainly due to stronger PL emission, higher ODMR contrast and an optimized pulsed measurement protocol that exceeds the sensitivity of standard cw ODMR measurements performed here. Analogously, the magnetic field resolution of the V_B^- can be quantified at room temperature as $\delta_B^{295\ K} = 85.1\ ^{\mu T}/\sqrt{Hz}$ ($\delta_B^{50\ K} = 4.33\ ^{\mu T}/\sqrt{Hz}$ at $T = 50$ K). This is comparable to V_{Si} in SiC (10 $^{\mu T}/\sqrt{Hz}$) [142] but lower than for NVs in diamond (3 $^{nT}/\sqrt{Hz}$) [156]. However, spin defects in 3D materials can lose their superior properties if they are close to the surface of the crystalline host [144], which also leads to an inevitable limitation of the minimum achievable sensor-to-object distance. This can significantly hinder the effectiveness of the spin defects-based sensors in 3D materials, highlighting the potential advantages of the V_B^- center as a nanometer scale sensor.
Finally, an estimate of the minimum detectable magnetic field is performed, which is based on the spin-projection noise analysis [152]. Accordingly:

$$\delta B \cong \frac{1}{g\mu_B R\sqrt{\eta}\sqrt{N t T_2^*}} \tag{7.16}$$

where g is the electronic Landé factor and μ_B is the Bohr magneton, so that $g\mu_B \approx 28\ ^{MHz}/_{mT}$, the ODMR contrast for V_B^- center is $R = 0.1$ %, η is the collection efficiency, N is the number of active spins and $t = 1s$ is taken as measurement time. Since the V_B^- density and the voxel size of about 10 μm diameter is known, a number $N \approx 2.6 \cdot 10^9$ of simultaneously addressed spins is estimated, and from the previously measured Rabi oscillations [22] (see Chapter 6.2) the dephasing time $T_2^* = 100$ ns is derived. The value for η is limited by both the efficiency of the detection setup and the optical properties of the spin-hosting sample, and is therefore important. On the one hand, the photon extraction efficiency of V_B^- defects in hBN is very high (near-unity for hBN monolayers) compared to, e.g. that of spin systems such as color centers in diamond. This is a consequence of the 2D nature of hBN which renders it less prone to phenomena such as total internal reflection or scattering. On the other hand, a crystal is present (even if the refractive index is lower than diamonds) and in the optical detection system a lens with low numerical aperture NA=0.3 is used. This leads to a consideration of a conservatively low - but realistic - value of $\eta \approx 1$ %. Note however, that higher values of η are feasible using objectives with higher NA and/or nanophotonic structures (e.g. solid immersion lenses). With the selected parameters a $\delta B \approx 20\ ^{nT}/\sqrt{Hz}$ is estimated. Note that the spectral linewidth is deliberately considered to be constrained by the reciprocal T_2^* time and not by longer spin-echo T_2 or dynamically decoupled spin-coherence times.

7.6 Conclusion

In this chapter, spin properties of V_B^- lattice defects in van der Waals hBN crystals have been analysed in terms of their sensitivity to external perturbations and their advantages and disadvantages for possible applications as a nanoscale quantum sensor have been evaluated. The advantages include the simple intrinsic nature of the defect basically consisting of a missing boron atom, but also the potentially accessible very small distance between the sensor and the object to be sensed. In particular, the focused laid on the influence of temperature on the ground-state zero-field splitting, which can be directly measured by cw ODMR and is explained by the temperature-dependent lattice compression/expansion. It has been shown that externally applied pressure induces lattice deformations and therefore can be mapped onto the defect ODMR spectrum of the V_B^-. However, temperature and pressure measurements need to be performed isobar or isothermal, respectively. Nevertheless, V_B^- can be used for simultaneous magnetic field measurements with high sensitivity, due to the invariability of its g-factor with respect to temperature and pressure. By comparing three spin defect hosting solid systems, diamond, SiC and hBN, it has been discussed that the V_B^- defect has comparable and, in some cases, even superior properties compared to 3D hosts. The coupling coefficient between zero-field splitting and temperature in the temperature range 50–350 K is eight times larger than the corresponding factor for NV^- centers in diamond. Moreover, hBN is particularly interesting for temperature sensing under cryogenic conditions, i.e. at temperatures down to a few K, since V_B^- centers exhibit a measurable temperature dependence of ZFS there, while it is nearly constant for NV^- centers in diamond. For completeness, a temperature sensor based on NV centers in diamond is still more sensitive, mainly due to stronger PL emission, higher ODMR contrast and an optimized pulsed measurement protocol that exceeds the sensitivity of cw ODMR measurements. Regarding temperature sensing, it has been demonstrated that heating effects due to laser excitation and absorbed microwave power are important, but they can be controlled. The resolution of V_B^- to external magnetic fields is comparable to that of silicon vacancies in SiC, but lower than that of NV centers in diamond. However, it can be expected that the favorable optical properties of this 2D system, recent demonstration of coherent control of V_B^- spins in hBN together with the overcoming of inhomogeneous ODMR line broadening by multifrequency spectroscopy [22] will stimulate the development of advanced pulse protocols [72] and lead to a further increase in the resolution of this sensor. In addition, during preparation of this chapter, a relevant work on V_B^- in hBN was published by [157] reporting its high temperature stability up to 600 K. Finally, the unique feature of hBN is its non-disturbing chemi-

cal and crystallographic compatibility with many different 2D materials, which gains a new fundamental functionality with the embedded spin centers and allows sensing in heterostructures with high resolution serving as a boundary itself.

Appendix: Calculation of polynomial coefficients for temperature measurements

In the main text a relationship between the ZFS $D_{gs}(\eta_a, \eta_c)$ and the relative changes η_a η_c of the temperature-dependent lattice parameters $a(T)$ and $c(T)$ are derived. In the following, this will be extended and an expression derived to compute $D_{gs}(T)$ directly. First, the temperature-dependent lattice parameters $a(T)$ and $c(T)$ are required. The mathematical description in terms of a third-order polynomial is used as described in [35].

$$a(T) = \sum_k A_k^a T^k \, (k = 0,1,2,3) \tag{7.17}$$

$$c(T) = \sum_k A_k^c T^k \, (k = 0,1,2,3) \tag{7.18}$$

A_k^a and A_k^c are the polynomial coefficients given in Table 3 of [35] and k is an integer. The relative changes of the lattice parameters with respect to room temperature are:

$$\eta_a(T) = \frac{a(T) - a(295\,\mathrm{K})}{a(295\,\mathrm{K})} = \frac{a(T)}{a(295\,\mathrm{K})} - 1 \tag{7.19}$$

$$\eta_c(T) = \frac{c(T) - c(295\,\mathrm{K})}{c(295\,\mathrm{K})} = \frac{c(T)}{c(295\,\mathrm{K})} - 1 \tag{7.20}$$

Inserting the polynomials of Equation 7.17 (7.18) into Equation 7.19 (7.20) results in

$$\eta_a(T) = \frac{A_0^a}{a(295\,\mathrm{K})} - 1 + \frac{A_1^a}{a(295\,\mathrm{K})} T + \frac{A_2^a}{a(295\,\mathrm{K})} T^2 + \frac{A_3^a}{a(295\,\mathrm{K})} T^3 \tag{7.21}$$

$$\eta_c(T) = \frac{A_0^c}{c(295\,\mathrm{K})} - 1 + \frac{A_1^c}{c(295\,\mathrm{K})} T + \frac{A_2^c}{c(295\,\mathrm{K})} T^2 + \frac{A_3^c}{c(295\,\mathrm{K})} T^3 \tag{7.22}$$

These expressions are grouped in polynomials with coefficients $A_k^{\eta_{a,c}}$:

$$\eta_a(T) = \sum_k A_k^{\eta_a} T^k \text{ and } \eta_c(T) = \sum_k A_k^{\eta_c} T^k \tag{7.23}$$

$$A_0^{\eta_a} = \frac{A_0^a}{a(295\,\mathrm{K})} - 1 \text{ and } A_0^{\eta_c} = \frac{A_0^c}{c(295\,\mathrm{K})} - 1 \text{ for } k = 0 \tag{7.24}$$

$$A_0^{\eta_a} = \frac{A_k^a}{a\,(295\text{ K})} \text{ and } A_0^{\eta_c} = \frac{A_k^c}{c\,(295\text{ K})} \text{ for } k = 1,2,3 \tag{7.25}$$

Next, $\eta_a(T)$ and $\eta_c(T)$ will be implemented into Equation 7.2 of the main text:

$$D_{gs}(\eta_a,\eta_c) = D_{gs,295\text{ K}} + \theta_a \eta_a h + \theta_c \eta_c h \tag{7.26}$$

Finally, this results in a polynomial for the ZFS $D_{gs}(T)$ with coefficients A_k^D that are directly calculated from the polynomial coefficients A_k^a and A_k^c for the temperature-dependent lattice compression[35] together with reference parameters at $T = 295$ K: $a\,(295\text{ K}) = 2.5047$ Å, $c\,(295\text{ K}) = 6.6532$ Å, $D_{gs,295\text{ K}}/h = 3.48$ GHz.

$$D_{gs}(T) = h\sum_k A_k^D T^k \tag{7.27}$$

$$A_0^D = D_{gs,295\text{ K}}/h + \theta_a\left(\frac{A_0^a}{a\,(295\text{ K})} - 1\right) + \theta_c\left(\frac{A_0^c}{c\,(295\text{ K})} - 1\right) \text{ for } k = 0 \tag{7.28}$$

$$A_k^D = \theta_a \frac{A_k^a}{a\,(295\text{ K})} + \theta_c \frac{A_k^c}{c\,(295\text{ K})} \text{ for } k = 1,2,3 \tag{7.29}$$

Since A_k^a and A_k^c are sectionally defined for different temperature ranges, the same sections are obtained for the coefficients A_k^D. The results are shown in Table 7.2.

Temperature range (K)	A_0^D (GHz)	A_1^D (MHz/K)	A_2^D (kHz/K^2)	A_3^D (Hz/K^3)
5-128	3.6367	0	-4.4308	11.468
128-189	3.6109	0.22839	-3.8805	5.522
189-350	3.6664	-0.55659	-0.2383	0

Table 7.2: Calculated polynomial coefficients A_k^D for Equation 7.27. The three different temperature regions arise from the sectionally defined polynomial for the temperature-dependent lattice parameters a and c[35].

8 Outlook: Defect Engineering

ABSTRACT: Optically accessible spin defects in solid-state materials are optimal candidates for applications in quantum information and sensing. One of the most limiting factors for their application is the coherence time of the respective system. For spin defects like V_{Si} in SiC or NV^- in diamond it is well-known that the defect creation (including the resulting defect density) has an influence on the T_2 time. Here, an improvement of the coherence properties of V_B^- is exemplary demonstrated using ion-treated hexagonal boron nitride flakes.

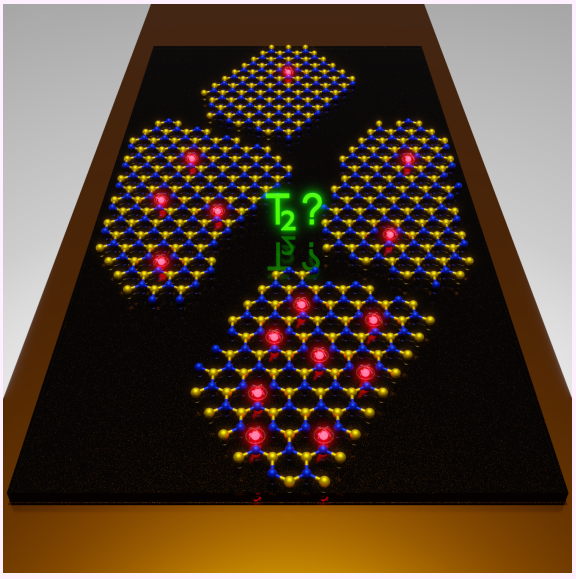

In the following section, defect engineering will be motivated, as it was already the case for the more established materials such as diamond and SiC[71]. The coherence time $T_2 \approx 2\ \mu s$ of the system is long compared to systems such as quantum dots[8], but short with respect to other defects in other (but 3D) materials. This is partially due to the magnetic environment, but probably also, as shown in Figure 6.9, due to the high defect density, resulting in the interferences between the defects as well. In SiC, for example, the correlation

$$T_2 = \frac{T_2^{(pristine)}}{1 + T_2^{(pristine)} \kappa N_V} \tag{8.1}$$

can be observed assuming a linear dependence of the spin dephasing rate and the defect concentration[71] . The T_2 time collapses strongly for high defect densities N_V and deviates significantly from the T_2 time of an unirradiated system (quasi single defect in the crystal). A similar dependence can be expected for hBN especially since also for NV^- diamond a drop of the dephasing time for higher defect densities can be observed[158].

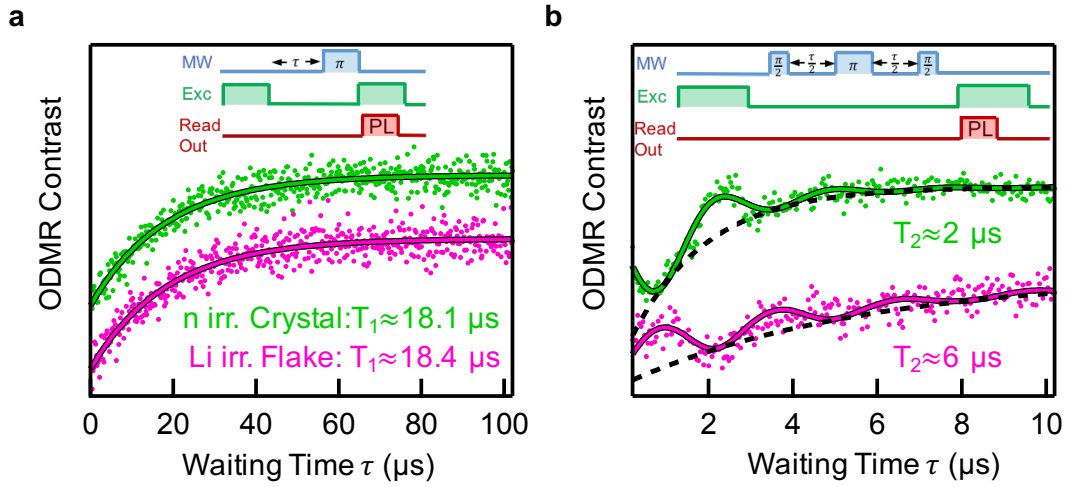

Figure 8.1: Comparison of a neutron irradiated hBN single crystal (green) and a lithium irradiated hBN flake (pink). **a** Spin-lattice relaxation dynamics of V_B^- spin centers at room temperature. The T_1 time is almost identical ($\approx 18\ \mu s$) for both samples. **b** Spin-spin relaxation dynamics of V_B^- spin centers at room temperature. The T_2 time of the lithium irradiated sample is approximately 3 times larger than for the neutron irradiated sample.

The majority of the results in this work are based on the highly neutron irradiated single crystal of hBN. In addition to this sample, cw ODMR has also been demonstrated on lithium irradiated flakes (see Chapter 5.5). Since the PL of this sample was significantly lower than those of the single crystal, it can be assumed that this is caused, partly, by a lower defect density. The sample consists of only a few layers of hBN, thus, quantitative EPR measurements for determining defect density as performed for the crystal

are not possible. In Figure 8.1 T_1 and T_2 measurements are shown for both the neutron irradiated sample (green) and the lithium (pink) irradiated sample.
The spin-lattice relaxation time is about $T_1 \approx 18\ \mu$s for both samples. This almost constant behaviour is also observable for SiC[71]. The coherence time for the lithium irradiated sample, however, is a factor of 3 higher than the coherence time of the neutron irradiated sample and reaches $T_2 \approx 6\ \mu$s. A more detailed systematic analysis with samples of known defect density would be desirable here to confirm the trend and allow the maximum T_2 time $T_2^{(pristine)}$ to be determined based on Equation 8.1. It would be interesting to know whether the coherence of a boron vacancy is limited by other defects or by the magnetic environment of surrounding nuclear spins. Nevertheless, it is worth emphasizing that even the T_2 time of 2 μs is already sufficient to use V_B^- for first applications. Many applications of NV^- diamond are theoretically transferable to hBN. These include simple magnetic field/temperature measurements, direct investigations in/on biological samples or more complex pulse sequences for NMR measurements[10]. It is important to highlight that hBN is considered as an insulator in heterostructures and in general as an encapsulating material for 2D materials and thus can contribute to study many novel 2D phenomena using V_B^-.
Besides this advantage, hBN may eventually replace NV^- diamond in terms of sensing on the (sub)nanometer scale, since it is expected that the defect does not change its properties close to the surface, in contrast to NV^- diamond[13]. In addition to D and A being maintained constant[49], initial depth-dependent T_1 and T_2 measurements by other groups have already shown that the relaxation times remain unchanged[159]. The goal here is to move on to single defects to investigate the sub-nanometer resolutions as in NV^- diamond. Previous disadvantages of hBN such as the lower PL or the smaller ODMR contrast can be overcome by plasmonic structures and optical cavities[76,159]. Optical cavities such as bullseye cavities, for example, can selectively increase the PL band of the defect by a suitable resonance frequency. Plasmonic structures like additional gold layers to hBN can further enhance the optical rates and thus increase the ODMR contrast. Xingyu Gao et al. has recently demonstrated an ODMR contrast of 46 % for the negatively charged boron vacancy at room temperature, which surpasses even the previous record of NV^- diamond[159].

9 Summary

In this work, an optically addressable spin defect in a Van der Waals material (hexagonal boron nitride) was detected for the very first time. The 2D character of the material hBN is of particular importance, as it is used as the standard material for the encapsulation of other 2D materials and thus makes a wide variety of applications of the newly discovered spin defect conceivable.

In the first experimental chapter, the evidence of this intrinsic defect is provided and the photoluminescence band (maximum at 850 nm) is assigned to the defect. It can be shown that this defect is the negatively charged boron vacancy (V_B^-). It possesses a triplet ground state which degeneracy is lifted by a zero field splitting of ${}^{D_{gs}}/_{h} = 3.48$ GHz ($D_{gs} > 0$) and ${}^{E_{gs}}/_{h} = 50$ MHz, respectively. The defect can be intialized and read out by an optical excitation (e.g. 532 nm) which is based on a spin polarization of the $m_S = 0$ state. This effect can be detected already at room temperature. Furthermore, spin Hamiltonian parameters such as the g-factor ($g = 2.00$) and hyperfine splittings from the neighboring nitrogen atoms ($I = 1$) can be observed and determined. The latter is characterized by seven equidistant side peaks with a spacing of $A = 47$ MHz, which can be observed in ODMR (small magnetic field, room temperature) as well as EPR (large magnetic field, $T = 5$ K) independent of the measurement method. The symmetry of the defect belongs to the D_{3h} group and can be confirmed by angle-dependent EPR measurements. Finally, it is demonstrated that the defect is not only produced in strongly neutron irradiated hBN crystals, but can also be implanted in hBN flakes by irradiation with ions such as gallium and lithium, revealing the intrinsic nature of the defect.

In the second experimental chapter, a coherent control of the spin defect is demonstrated by means of pulsed magnetic resonance experiments - and that already at room temperature. At first, Rabi oscillations are realized by irradiating microwave pulses of variable length, which allows to manipulate the spin system quasi arbitrarily on the Bloch sphere. The limiting spin-lattice relaxation can be determined to be $T_1 = 18$ μs. The phonon influence can be studied by temperature-dependent measurements of the T_1 time, yielding a maximum spin-lattice relaxation of $T_1 = 12.5$ ms observed at low temperatures ($T = 20$ K) by freezing of phonons. For most quantum applications,

the coherence of the system is relevant, which is quantified by the spin-spin relaxation T_2. This is determined to be $T_2 \approx 2\ \mu$s independent of the ambient temperature (50 – 300 K). Here, a modulation of the signal due to the surrounding nuclear spins can be observed, which can be attributed to the nuclear Zeeman effect and quadrupole splitting by 3-pulse ESEEM measurements. Finally, a multi-frequency ODMR method is applied to the system to decouple the spin state from its inhomogeneous nuclear environment. Here, the observable ODMR linewidth can be significantly reduced (some 10 kHz), which is considered as an estimation for an upper limit of the relaxation times.
In the third experimental section, first applications of the defect as a potential sensor in 2D materials and van der Waals hetero structures are discussed. By means of ODMR, it is shown that an optical readout of the spin state allows measurements of temperature, external pressure on the crystal, and magnetic fields. A shift in the zero-field splitting D_{gs} can be observed, for example, upon variation of the temperature. This shift can be attributed to a change in the lattice parameters based on a linear model. This shift can equally be realized by external pressures, making V_B^- in hBN an ideal pressure sensor. Exemplarily, this effect is experimentally confirmed in the c direction, coinciding excellently with the calculated predictions. Finally, the splitting due to the Zeeman effect is examined quantitatively to motivate V_B^- as a magnetic field sensor for a broad magnetic field range (3 – 3500 mT).
Finally, a short outlook illustrates how one of the few disadvantages of the boron vacancy - its comparably low coherence - can be improved. By optimizing the defect creation, a significant increase of T_2 is conceivable, which would enable even broader fields of application for the boron vacancy.

Zusammenfassung

Im Rahmen dieser Arbeit konnte zum allerersten Mal ein optisch addressierbarer Spin Defekt in einem Van-der-Waals Material (hexagonales Bornitrid) nachgewiesen werden. Hervorzuheben ist hierbei der 2D Charakter des Materials hBN, welches als das Standardmaterial zur Verkapselung anderer 2D Materialien verwendet wird und somit unterschiedlichste Anwendungen des neu entdeckten Spindefektes denkbar macht.
Im ersten Ergebniskapitel wird der Nachweis dieses intrinsischen Defektes erbracht und dessen Photolumineszenzband (Maximum bei 850 nm) zugeordnet. Es kann gezeigt werden, dass es sich bei diesem Defekt um die negativ geladene Borfehlstelle (V_B^-) handelt. Diese besitzt einen Triplett Grundzustand, dessen Entartung durch eine Nullfeldaufspaltung von ${}^{D_{gs}}/_{h}$ = 3.48 GHz ($D_{gs} > 0$) bzw. ${}^{E_{gs}}/_{h}$ = 50 MHz aufgehoben ist. Der Defekt kann durch eine optische Anregung (z.B. 532 nm) intialisiert und ausgelesen werden, was auf einer Spinpolarisation des $m_S = 0$ Zustandes beruht. Dieser Effekt kann bereits bei Raumtemperatur nachgewiesen werden. Des Weiteren können Spin Hamiltonian Parameter wie der g-Faktor ($g = 2.00$) und Hyperfeinaufspaltungen von den benachbarten Stickstoffatomen ($I = 1$) beobachtet und bestimmt werden. Letzteres zeichnet sich durch sieben äquidistante Seitenpeaks mit einem Abstand von $A = 47$ MHz ab, was unabhängig von der Messmethode sowohl bei ODMR (kleines Magnetfeld, Raumtemperatur) als auch bei EPR (großes Magnetfeld, $T = 5$ K) beobachtet werden kann. Die Symmetrie des Defektes zählt zur D_{3h}-Gruppe und kann mittels winkelabhängigen EPR Messungen bestätigt werden. Zuletzt wird gezeigt, dass der Defekt nicht nur in stark Neutron bestrahlten hBN Kristallen erzeugt, sondern auch durch Bestrahlung mit Ionen wie Gallium und Lithium in hBN Flocken implantiert werden kann, was die intrisische Natur des Defektes belegt.
Im zweiten Ergebniskapitel wird mittels gepulster Magnetresonanz Experimenten eine kohärente Kontrolle des Spin Defektes nachgewiesen - und das bereits bei Raumtemperatur. Zuerst können Rabi-Oszillationen durch Einstrahlen von Mikrowellenpulse variabler länger demonstriert werden, was nun als Grundlage dient um das Spin-System quasi beliebig auf der Bloch-Sphäre manipulieren zu können. Die limitierende Spin-Gitter-Relaxation kann zu $T_1 = 18$ μs bestimmt werden. Der Phononeneinfluss kann durch temperaturabhänge Messungen der T_1 Zeit untersucht werden, sodass bei tiefen Temperaturen ($T = 20$ K) durch Ausfrieren von Phononen eine maximale Spin-Gitter-Relaxation von $T_1 = 12.5$ ms beobachtet werden kann. Für die meisten Quantenanwendungen ist die Kohärenz des Systems relevant, welche durch die Spin-Spin-Relaxation T_2 quantifiziert wird. Diese kann zu $T_2 \approx 2$ μs unabhängig von der Umgebungstemperatur (50 − 300 K) bestimmt werden. Hierbei kann eine Modulation des Signals aufgrund

der umliegenden Kernspins beobachtet werden, welche durch 3-Puls ESEEM Messungen auf den Kern-Zeeman Effekt und Quadrupolsplitting zurückgeführt werden kann. Zuletzt wird eine Multifrequenz-ODMR Methode auf das System angewendet um den Spin-Zustand von seiner inhomogenen Kernumgebung zu entkoppeltn. Hierbei kann die beobachtbare ODMR Linienbreite deutlich reduziert werden (einige 10 kHz), was als Abschätzung für ein oberes Limit der Relaxationszeiten gilt.
Im dritten Ergebnisteil werden erste Anwendungen des Defektes als potentieller Sensor in 2D Materialen und Van-der-Waals Hetero Strukturen diskutiert. Es wird gezeigt, dass mittels ODMR ein optisches Auslesen des Spin-Zustandes Messungen der Temperatur, externen Druckes auf den Kristall und Magnetfeldern ermöglicht. So kann bei Variation der Temperatur eine Verschiebung der Nullfeldaufspaltung D_{gs} beobachtet werden. Dies kann mittels eines linearen Modells auf eine Änderung der Gitterparameter zurück geführt werden. Diese Änderung kann ebenso durch äußere Drücke realiert werden, was V_B^- in hBN zu einem idealen Drucksensor macht. Exemplarisch wird dieser Effekt in c-Richtung experimentell bestätigt, was sich hervorragend mit den berechneten Vorhersagen deckt. Zuletzt wird die Aufspaltung aufgrund des Zeeman Effektes quantitativ untersucht um V_B^- als Magnetfeldsensor für einen breiten Magnetfeldbereich (3 – 3500 mT) zu motivieren.
Zum Schluss wird in einem kurzen Ausblick gezeigt, inwiefern einer der wenigen Nachteile der Borfehlstelle -die vergleichsweise niedrige Kohärenz- verbessert werden kann. Durch eine Optimierung der Defektherstellung, ist eine deutliche Steigerung von T_2 denkbar, was der Borfehlstelle noch breitere Anwendungsfelder ermöglicht.

Bibliography

[1] F. Arute, K. Arya, R. Babbush, D. Bacon, J. C. Bardin, R. Barends, R. Biswas, S. Boixo, F. G. Brandao, D. A. Buell, B. Burkett, Y. Chen, Z. Chen, B. Chiaro, R. Collins, W. Courtney, A. Dunsworth, E. Farhi, B. Foxen, A. Fowler, C. Gidney, M. Giustina, R. Graff, K. Guerin, S. Habegger, M. P. Harrigan, M. J. Hartmann, A. Ho, M. Hoffmann, T. Huang, T. S. Humble, S. V. Isakov, E. Jeffrey, Z. Jiang, D. Kafri, K. Kechedzhi, J. Kelly, P. V. Klimov, S. Knysh, A. Korotkov, F. Kostritsa, D. Landhuis, M. Lindmark, E. Lucero, D. Lyakh, S. Mandrà, J. R. McClean, M. McEwen, A. Megrant, X. Mi, K. Michielsen, M. Mohseni, J. Mutus, O. Naaman, M. Neeley, C. Neill, M. Y. Niu, E. Ostby, A. Petukhov, J. C. Platt, C. Quintana, E. G. Rieffel, P. Roushan, N. C. Rubin, D. Sank, K. J. Satzinger, V. Smelyanskiy, K. J. Sung, M. D. Trevithick, A. Vainsencher, B. Villalonga, T. White, Z. J. Yao, P. Yeh, A. Zalcman, H. Neven and J. M. Martinis. Quantum supremacy using a programmable superconducting processor. *Nature*, **574**, 7779, 505 (2019). ISSN 14764687. doi: 10.1038/s41586-019-1666-5.

[2] P. Krantz, M. Kjaergaard, F. Yan, T. P. Orlando, S. Gustavsson and W. D. Oliver. A quantum engineer's guide to superconducting qubits. *Applied Physics Reviews*, **6**, 2 (2019). ISSN 19319401. doi: 10.1063/1.5089550.

[3] A. Gruber, A. Dräbenstedt, C. Tietz, L. Fleury, J. Wrachtrup and C. Von Borczyskowski. Scanning confocal optical microscopy and magnetic resonance on single defect centers. *Science*, **276**, 5321, 2012 (1997). ISSN 00368075. doi: 10.1126/science.276.5321.2012.

[4] D. D. Awschalom, R. Hanson, J. Wrachtrup and B. B. Zhou. Quantum technologies with optically interfaced solid-state spins. *Nature Photonics*, **12**, 9, 516 (2018). ISSN 17494893. doi: 10.1038/s41566-018-0232-2.

[5] M. S. Grinolds, M. Warner, K. De Greve, Y. Dovzhenko, L. Thiel, R. L. Walsworth, S. Hong, P. Maletinsky and A. Yacoby. Subnanometre resolution in three-dimensional magnetic resonance imaging of individual dark spins. *Nature Nanotechnology*, **9**, 4, 279 (2014). ISSN 17483395. doi: 10.1038/nnano.2014.30.

[6] G. Kucsko, P. C. Maurer, N. Y. Yao, M. Kubo, H. J. Noh, P. K. Lo, H. Park and M. D. Lukin. Nanometre-scale thermometry in a living cell. *Nature*, **500**, 7460, 54 (2013). ISSN 00280836. doi: 10.1038/nature12373.

[7] R. Schirhagl, K. Chang, M. Loretz and C. L. Degen. Nitrogen-vacancy centers in diamond: Nanoscale sensors for physics and biology. *Annual Review of Physical Chemistry*, **65**, 83 (2014). ISSN 0066426X. doi: 10.1146/annurev-physchem-040513-103659.

[8] G. Moody, C. McDonald, A. Feldman, T. Harvey, R. P. Mirin and K. L. Silverman. Electronic Enhancement of the Exciton Coherence Time in Charged Quantum Dots. *Physical Review Letters*, **116**, 3, 1 (2016). ISSN 10797114. doi: 10.1103/PhysRevLett.116.037402.

[9] I. Lovchinsky, J. D. Sanchez-Yamagishi, E. K. Urbach, S. Choi, S. Fang, T. I. Andersen, K. Watanabe, T. Taniguchi, A. Bylinskii, E. Kaxiras, P. Kim, H. Park and M. D. Lukin. Magnetic resonance spectroscopy of an atomically thin material using a single-spin qubit. *Science*, **355**, 6324, 503 (2017). ISSN 10959203. doi: 10.1126/science.aal2538.

[10] I. Lovchinsky, A. O. Sushkov, E. Urbach, N. P. de Leon, S. Choi, K. D. Greve, R. Evans, R. Gertner, E. Bersin, C. Müller, L. McGuinness, F. Jelezko, R. L. Walsworth, H. Park and M. D. Lukin. Nuclear magnetic resonance detection and spectroscopy of single proteins using quantum logic. *Science*, **351**, 6275, 836 (2016). ISSN 10959203. doi: 10.1126/science.aad8022.

[11] M. Kost, J. Cai and M. B. Plenio. Resolving single molecule structures with Nitrogen-vacancy centers in diamond. *Scientific Reports*, **5**, 11007 (2015). ISSN 20452322. doi: 10.1038/srep11007.

[12] Y. C. Chen, P. S. Salter, S. Knauer, L. Weng, A. C. Frangeskou, C. J. Stephen, S. N. Ishmael, P. R. Dolan, S. Johnson, B. L. Green, G. W. Morley, M. E. Newton, J. G. Rarity, M. J. Booth and J. M. Smith. Laser writing of coherent colour centres in diamond. *Nature Photonics*, **11**, 2, 77 (2017). ISSN 17494893. doi: 10.1038/nphoton.2016.234.

[13] S. Ishizu, K. Sasaki, D. Misonou, T. Teraji, K. M. Itoh and E. Abe. Spin coherence and depths of single nitrogen-vacancy centers created by ion implantation into diamond via screening masks. *Journal of Applied Physics*, **127**, 24 (2020). ISSN 10897550. doi: 10.1063/5.0012187.

[14] E. P. Randviir, D. A. Brownson and C. E. Banks. A decade of graphene research: Production, applications and outlook. *Materials Today*, **17**, 9, 426 (2014). ISSN 13697021. doi: 10.1016/j.mattod.2014.06.001.

[15] J. Wang, F. Ma and M. Sun. Graphene, hexagonal boron nitride, and their heterostructures: properties and applications. *RSC Advances*, **7**, 27, 16801 (2017). ISSN 20462069. doi: 10.1039/c7ra00260b.

[16] F. Reis, G. Li, L. Dudy, M. Bauernfeind, S. Glass, W. Hanke and R. Thomale. Bismuthene on a SiC substrate : A candidate for a high-temperature quantum spin Hall material. *Science*, **357**, 6348, 287 (2017). ISSN 10959203. doi: 10.1126/science.aai8142.

[17] L. He, X. Kou and K. L. Wang. Review of 3D topological insulator thin-film growth by molecular beam epitaxy and potential applications. *Physica Status Solidi - Rapid Research Letters*, **7**, 1-2, 50 (2013). ISSN 18626254. doi: 10.1002/pssr.201307003.

[18] S. Tongay, J. Zhou, C. Ataca, K. Lo, T. S. Matthews, J. Li, C. Grossman and J. Wu. Thermally Driven Crossover from Indirect toward Direct Bandgap in 2D Semiconductors: $MoSe_2$ versus MoS_2. *Nano Letters*, **12**, 8 (2012). ISSN 15205215. doi: 10.1021/nl302584w.

[19] N. Petrone, T. Chari, I. Meric, L. Wang, K. L. Shepard and J. Hone. Flexible Graphene Field-Effect Transistors Encapsulated in Hexagonal Boron Nitride. *ACS Nano*, **9**, 9, 8953 (2015). ISSN 1936086X. doi: 10.1021/acsnano.5b02816.

[20] Q. Cao, F. Grote, M. Humann and S. Eigler. Emerging field of few-layered intercalated 2D materials. *Nanoscale Advances*, **3**, 4, 963 (2021). ISSN 25160230. doi: 10.1039/d0na00987c.

[21] A. Gottscholl, M. Kianinia, V. Soltamov, S. Orlinskii, G. Mamin, C. Bradac, C. Kasper, K. Krambrock, A. Sperlich, M. Toth, I. Aharonovich and V. Dyakonov. Initialization and read-out of intrinsic spin defects in a van der Waals crystal at room temperature. *Nature Materials*, **19**, 5, 540 (2020). ISSN 14764660. doi: 10.1038/s41563-020-0619-6.

[22] A. Gottscholl, M. Diez, V. Soltamov, C. Kasper, A. Sperlich, M. Kianinia, C. Bradac, I. Aharonovich and V. Dyakonov. Room temperature coherent control of spin defects in hexagonal boron nitride. *Science Advances*, **7**, 14, 1 (2021). ISSN 23752548. doi: 10.1126/sciadv.abf3630.

[23] A. Gottscholl, M. Diez, V. Soltamov, C. Kasper, D. Krauße, A. Sperlich, M. Kianinia, C. Bradac, I. Aharonovich and V. Dyakonov. Spin defects in hBN as promising temperature, pressure and magnetic field quantum sensors. *Nature Communications*, **12**, 1, 6 (2021). ISSN 20411723. doi: 10.1038/s41467-021-24725-1.

[24] T. A. Chen, C. P. Chuu, C. C. Tseng, C. K. Wen, H. S. Wong, S. Pan, R. Li, T. A. Chao, W. C. Chueh, Y. Zhang, Q. Fu, B. I. Yakobson, W. H. Chang and L. J. Li. Wafer-scale single-crystal hexagonal boron nitride monolayers on Cu (111). *Nature*, **579**, 7798, 219 (2020). ISSN 14764687. doi: 10.1038/s41586-020-2009-2.

[25] C. R. Hsing, C. Cheng, J. P. Chou, C. M. Chang and C. M. Wei. Van der Waals interaction in a boron nitride bilayer. *New Journal of Physics*, **16**, 111 (2014). ISSN 13672630. doi: 10.1088/1367-2630/16/11/113015.

[26] L. Cao, S. Emami and K. Lafdi. Large-scale exfoliation of hexagonal boron nitride nanosheets in liquid phase. *Materials Express*, **4**, 2, 165 (2014). ISSN 21585857. doi: 10.1166/mex.2014.1155.

[27] K. Watanabe, T. Taniguchi and H. Kanda. Direct-bandgap properties and evidence for ultraviolet lasing of hexagonal boron nitride single crystal. *Nature Materials*, **3**, 6, 404 (2004). ISSN 14761122. doi: 10.1038/nmat1134.

[28] Y. Hattori, T. Taniguchi, K. Watanabe and K. Nagashio. Layer-by-layer dielectric breakdown of hexagonal boron nitride. *ACS Nano*, **9**, 1, 916 (2015). ISSN 1936086X. doi: 10.1021/nn506645q.

[29] A. Katzir, J. T. Suss, A. Zunger and A. Halperin. Point defects in hexagonal boron nitride. I. EPR, thermoluminescence, and thermally-stimulated-current measurements. *Physical Review B*, **11**, 6, 2370 (1975). ISSN 01631829. doi: 10.1103/PhysRevB.11.2370.

[30] S. Y. Lee, T. Y. Jeong, S. Jung and K. J. Yee. Refractive Index Dispersion of Hexagonal Boron Nitride in the Visible and Near-Infrared. *Physica Status Solidi (B) Basic Research*, **256**, 6, 1 (2019). ISSN 15213951. doi: 10.1002/pssb.201800417.

[31] G. H. Lee, X. Cui, Y. D. Kim, G. Arefe, X. Zhang, C. H. Lee, F. Ye, K. Watanabe, T. Taniguchi, P. Kim and J. Hone. Highly Stable, Dual-Gated MoS2 Transistors Encapsulated by Hexagonal Boron Nitride with Gate-Controllable Contact, Resistance, and Threshold Voltage. *ACS Nano*, **9**, 7, 7019 (2015). ISSN 1936086X. doi: 10.1021/acsnano.5b01341.

[32] Z. Lin, A. Mcnamara, Y. Liu, K. sik Moon and C. P. Wong. Exfoliated hexagonal boron nitride-based polymer nanocomposite with enhanced thermal conductivity for electronic encapsulation. *Composites Science and Technology*, **90**, 123 (2014). ISSN 02663538. doi: 10.1016/j.compscitech.2013.10.018.

[33] J. Dauber, A. A. Sagade, M. Oellers, K. Watanabe, T. Taniguchi, D. Neumaier and C. Stampfer. Ultra-sensitive Hall sensors based on graphene encapsulated in hexagonal boron nitride. *Applied Physics Letters*, **106**, 19, 1 (2015). ISSN 00036951. doi: 10.1063/1.4919897.

[34] M. Seitz, P. Gant, A. Castellanos-Gomez and F. Prins. Long-term stabilization of two-dimensional perovskites by encapsulation with hexagonal boron nitride. *Nanomaterials*, **9**, 8 (2019). ISSN 20794991. doi: 10.3390/nano9081120.

[35] W. Paszkowicz, J. B. Pelka, M. Knapp, T. Szyszko and S. Podsiadlo. Lattice parameters and anisotropic thermal expansion of hexagonal boron nitride in the 10-297.5 K temperature range. *Applied Physics A: Materials Science and Processing*, **75**, 3, 431 (2002). ISSN 09478396. doi: 10.1007/s003390100999.

[36] I. Jo, M. T. Pettes, J. Kim, K. Watanabe, T. Taniguchi, Z. Yao and L. Shi. Thermal conductivity and phonon transport in suspended few-layer hexagonal boron nitride. *Nano Letters*, **13**, 2, 550 (2013). ISSN 15306984. doi: 10.1021/nl304060g.

[37] L. Song, L. Ci, H. Lu, P. B. Sorokin, C. Jin, J. Ni, A. G. Kvashnin, D. G. Kvashnin, J. Lou, B. I. Yakobson and P. M. Ajayan. Large scale growth and characterization of atomic hexagonal boron nitride layers. *Nano Letters*, **10**, 8, 3209 (2010). ISSN 15306984. doi: 10.1021/nl1022139.

[38] C. Zhi, Y. Bando, C. Tang, H. Kuwahara and D. Golberg. Large-scale fabrication of boron nitride nanosheets and their utilization in polymeric composites with improved thermal and mechanical properties. *Advanced Materials*, **21**, 28, 2889 (2009). ISSN 09359648. doi: 10.1002/adma.200900323.

[39] R. V. Gorbachev, I. Riaz, R. R. Nair, R. Jalil, L. Britnell, B. D. Belle, E. W. Hill, K. S. Novoselov, K. Watanabe, T. Taniguchi, A. K. Geim and P. Blake. Hunting for monolayer boron nitride: Optical and raman signatures. *Small*, **7**, 4, 465 (2011). ISSN 16136810. doi: 10.1002/smll.201001628.

[40] A. K. Geim and I. V. Grigorieva. Van der Waals heterostructures. *Nature*, **499**, 7459, 419 (2013). ISSN 00280836. doi: 10.1038/nature12385.

[41] M. Pozzo, D. Alfè, P. Lacovig, P. Hofmann, S. Lizzit and A. Baraldi. Thermal expansion of supported and freestanding graphene: Lattice constant versus interatomic distance. *Physical Review Letters*, **106**, 13, 1 (2011). ISSN 00319007. doi: 10.1103/PhysRevLett.106.135501.

[42] M. Li, J. Shi, L. Liu, P. Yu, N. Xi and Y. Wang. Experimental study and modeling of atomic-scale friction in zigzag and armchair lattice orientations of MoS_2. *Science and Technology of Advanced Materials*, **17**, 1, 189 (2016). ISSN 18785514. doi: 10.1080/14686996.2016.1165584.

[43] G.-h. Lee, Y.-j. Yu, X. Cui, N. Petrone, C.-h. Lee, S. Choi, D.-y. Lee, C. Lee, W. J. Yoo, K. Watanabe, T. Taniguchi, C. Nuckolls, P. Kim and J. Hone. Flexible and Transparent MoS_2 Field-Effect Transistors on Hexagonal Boron Nitride-Graphene Heterostructures. *ACS Nano*, 7931–7936 (2013). ISSN 15205215. doi: 10.1021/nn402954e.

[44] S. A. Tawfik, S. Ali, M. Fronzi, M. Kianinia, T. T. Tran, C. Stampfl, I. Aharonovich, M. Toth and M. J. Ford. First-principles investigation of quantum emission from hBN defects. *Nanoscale*, **9**, 36, 13575 (2017). ISSN 20403372. doi: 10.1039/c7nr04270a.

[45] M. Abdi, J. P. Chou, A. Gali and M. B. Plenio. Color Centers in Hexagonal Boron Nitride Monolayers: A Group Theory and Ab Initio Analysis. *ACS Photonics*, **5**, 5, 1967 (2018). ISSN 23304022. doi: 10.1021/acsphotonics.7b01442.

[46] J. Zhang, R. Sun, D. Ruan, M. Zhang, Y. Li, K. Zhang, F. Cheng, Z. Wang and Z. M. Wang. Point defects in two-dimensional hexagonal boron nitride: A perspective. *Journal of Applied Physics*, **128**, 10 (2020). ISSN 10897550. doi: 10.1063/5.0021093.

[47] N. Mendelson, D. Chugh, J. R. Reimers, T. S. Cheng, A. Gottscholl, H. Long, C. J. Mellor, A. Zettl, V. Dyakonov, P. H. Beton, S. V. Novikov, C. Jagadish, H. H. Tan, M. J. Ford, M. Toth, C. Bradac and I. Aharonovich. Identifying carbon as the source of visible single-photon emission from hexagonal boron nitride. *Nature Materials*, **20**, 3, 321 (2021). ISSN 14764660. doi: 10.1038/s41563-020-00850-y.

[48] Q. Wang, Q. Zhang, X. Zhao, X. Luo, C. P. Y. Wong, J. Wang, D. Wan, T. Venkatesan, S. J. Pennycook, K. P. Loh, G. Eda and A. T. Wee. Photoluminescence Upconversion by Defects in Hexagonal Boron Nitride. *Nano Letters*, **18**, 11, 6898 (2018). ISSN 15306992. doi: 10.1021/acs.nanolett.8b02804.

[49] V. Ivády, G. Barcza, G. Thiering, S. Li, H. Hamdi, J. P. Chou, Ö. Legeza and A. Gali. Ab initio theory of the negatively charged boron vacancy qubit in hexagonal boron nitride. *npj Computational Materials*, **6**, 1, 1 (2020). ISSN 20573960. doi: 10.1038/s41524-020-0305-x.

[50] M. Mostafanejad. Basics of the spin Hamiltonian formalism. *International Journal of Quantum Chemistry*, **114**, 22, 1495 (2014). ISSN 1097461X. doi: 10.1002/qua.24721.

[51] D. Goldfarb and S. Stoll. *EPR spectroscopy: fundamentals and methods*. John Wiley & Sons (2018). ISBN 9781119162995.

[52] C. Karunakaran and M. Balamurugan. *Spin Resonance Spectroscopy: Principles and applications: Electron Paramagnetic Resonance Spectroscopy*. Elsevier (2013). ISBN 9780128136096. doi: 10.1016/B978-0-12-813608-9.00004-6.

[53] D. M. Murphy. *EPR (Electron Paramagnetic Resonance) Spectroscopy of Polycrystalline Oxide Systems*, chapter 1, 1–50. John Wiley and Sons, Ltd (2008). ISBN 9783527626113. doi: 10.1002/9783527626113.ch1.

[54] The NIST Reference on Constants, Units, and Uncertainty. Fundamental Physical Constants: electron g factor. https://physics.nist.gov/cgi-bin/cuu/Value?gem. Accessed: 2021-08-26.

[55] J. Stankowski, L. Piekara-Sady and W. Kempiński. EPR of a fullerene-molecule-derived paramagnetic center as a mesoscopic conducting object. *Applied Magnetic Resonance*, **19**, 3-4, 539 (2000). ISSN 09379347. doi: 10.1007/BF03162398.

[56] E. Soerman, N. T. Son, W. M. Chen, O. Kordina and E. Janzén. Silicon vacancy-related defect in 4H and 6H SiC. *Physical Review B - Condensed Matter and Materials Physics*, **61**, 4 (2000). ISSN 01631829. doi: 10.1103/PhysRevB.61.2613.

[57] S. B. Orlinski, J. Schmidt, E. N. Mokhov and P. G. Baranov. Silicon and carbon vacancies in neutron-irradiated SiC: A high-field electron paramagnetic resonance study. *Physical Review B - Condensed Matter and Materials Physics*, **67**, 12, 8 (2003). ISSN 1550235X. doi: 10.1103/PhysRevB.67.125207.

[58] J. A. Weil and J. R. Bolton. *Electron paramagnetic resonance: elementary theory and practical applications*. John Wiley & Sons (2007). ISBN 9780471754961. doi: 10.1002/0470084987.

[59] The NIST Reference on Constants, Units, and Uncertainty. Fundamental Physical Constants: proton gyromagnetic ratio. https://physics.nist.gov/cgi-bin/cuu/Value?gammap. Accessed: 2021-08-26.

[60] L. D. Rollmann and S. I. Chan. *Quadrupole effects in electron paramagnetic resonance spectra of polycrystalline copper and cobalt complexes*. Springer (1969). ISBN 9781468483239. doi: 10.1007/978-1-4684-8323-9_12.

[61] M. Brustolon and E. Giamello. *Electron Paramagnetic Resonance: A Practitioners Toolkit*. John Wiley & Sons (2009). ISBN 9780470432235. doi: 10.1002/9780470432235.

[62] G. R. Eaton, S. S. Eaton, D. P. Barr and R. T. Weber. *Quantitative Epr*. Springer Science & Business Media (2010). ISBN 9783211929483. doi: 10.1007/978-3-211-92948-3.

[63] E. Goovaerts. Optically detected magnetic resonance (odmr). *eMagRes*, **6**, 343 (2017). ISSN 20556101. doi: 10.1002/9780470034590.emrstm1524.

[64] A. O. Levchenko, V. V. Vasil'Ev, S. A. Zibrov, A. S. Zibrov, A. V. Sivak and I. V. Fedotov. Inhomogeneous broadening of optically detected magnetic resonance of the ensembles of nitrogen-vacancy centers in diamond by interstitial carbon atoms. *Applied Physics Letters*, **106**, 10, 1 (2015). ISSN 00036951. doi: 10.1063/1.4913428.

[65] D. Simin, F. Fuchs, H. Kraus, A. Sperlich, P. G. Baranov, G. V. Astakhov and V. Dyakonov. High-precision angle-resolved magnetometry with uniaxial quantum centers in silicon carbide. *Physical Review Applied*, **4**, 1, 1 (2015). ISSN 23317019. doi: 10.1103/PhysRevApplied.4.014009.

[66] T. L. James. Nuclear Magnetic Resonance in Biochemistry. *Elsevier* (1975). doi: 10.1016/B978-0-12-380950-6.X5001-4.

[67] D. Simin, H. Kraus, A. Sperlich, T. Ohshima, G. V. Astakhov and V. Dyakonov. Locking of electron spin coherence above 20 ms in natural silicon carbide. *Physical Review B*, **95**, 16, 2 (2017). ISSN 24699969. doi: 10.1103/PhysRevB.95.161201.

[68] J. H. Lee, J. J. Song, M. A. F. Scarparo and M. D. Levenson. Coherent population oscillations and hole burning observed in $Sm^{+2} : CaF_2$ using polarization spectroscopy. *Optics Letters*, **5**, 5, 196 (1980). ISSN 01469592. doi: 10.1364/ol.5.000196.

[69] L. W. Hillman, R. W. Boyd, J. Krasinski and C. R. Stroud. Observation of a spectral hole due to population oscillations in a homogeneously broadened optical absorption line. *Optics Communications*, **45**, 6, 416 (1983). ISSN 00304018. doi: 10.1016/0030-4018(83)90303-6.

[70] M. Mrozek, A. M. Wojciechowski, D. S. Rudnicki, J. Zachorowski, P. Kehayias, D. Budker and W. Gawlik. Coherent population oscillations with nitrogen-vacancy color centers in diamond. *Physical Review B*, **94**, 3, 1 (2016). ISSN 24699969. doi: 10.1103/PhysRevB.94.035204.

[71] C. Kasper, D. Klenkert, Z. Shang, D. Simin, A. Gottscholl, A. Sperlich, H. Kraus, C. Schneider, S. Zhou, M. Trupke, W. Kada, T. Ohshima, V. Dyakonov and G. V. Astakhov. Influence of Irradiation on Defect Spin Coherence in Silicon Carbide. *Physical Review Applied*, **13**, 4, 1 (2020). ISSN 23317019. doi: 10.1103/PhysRevApplied.13.044054.

[72] V. A. Soltamov, C. Kasper, A. V. Poshakinskiy, A. N. Anisimov, E. N. Mokhov, A. Sperlich, S. A. Tarasenko, P. G. Baranov, G. V. Astakhov and V. Dyakonov. Excitation and coherent control of spin qudit modes in silicon carbide at room temperature. *Nature Communications*, **10**, 1 (2019). ISSN 20411723. doi: 10.1038/s41467-019-09429-x.

[73] hq graphene. http://www.hqgraphene.com/h-BN-CAN1.php. Accessed: 2021-08-26.

[74] Graphene Supermarket. https://graphene-supermarket.com/Boron-Nitride-BN/. Accessed: 2021-08-26.

[75] F. Murzakhanov, B. Yavkin, G. Mamin, S. Orlinskii, I. Mumdzhi, I. Gracheva, B. Gabbasov, V. Smirnov, A.N.and Davydov and V. Soltamov. Creation of Negatively Charged Boron Vacancies in Hexagonal Boron Nitride Crystal by Electron Irradiation and Mechanism of Inhomogeneous Broadening of Boron Vacancy-Related Spin Resonance Lines. *Nanomaterials*, **11**, 6 (2021). ISSN 20794991. doi: 10.3390/nano11061373.

[76] J. E. Fröch, L. Spencer, M. Kianinia, D. Totonjian, M. Nguyen, , A. Gottscholl, V. Dyakonov, M. Toth, S. Kim and I. Aharonovich. Coupling spin defects in hexagonal boron nitride to monolithic bullseye cavities. *Nano Letters*, **21**, 15 (2021). ISSN 15306992. doi: 10.1021/acs.nanolett.1c01843.

[77] M. Kianinia, S. White, J. E. Fröch, C. Bradac and I. Aharonovich. Generation of Spin Defects in Hexagonal Boron Nitride. *ACS Photonics*, **7**, 8, 2147 (2020). ISSN 23304022. doi: 10.1021/acsphotonics.0c00614.

[78] X. Gao, S. Pandey, M. Kianinia, J. Ahn, P. Ju, I. Aharonovich, N. Shivaram and T. Li. Femtosecond Laser Writing of Spin Defects in Hexagonal Boron Nitride. *ACS Photonics*, **8**, 4, 994 (2021). ISSN 23304022. doi: 10.1021/acsphotonics.0c01847.

[79] X. Qian, J. Liu, L. Fu and J. Li. Quantum spin Hall effect in two-dimensional transition metal dichalcogenides. *Science*, **346**, 6215, 1344 (2014). ISSN 10959203. doi: 10.1126/science.1256815.

[80] B. Urbaszek and A. Srivastava. Materials in flatland twist and shine. *Nature*, **567**, 7746, 39 (2019). ISSN 14764687. doi: 10.1038/d41586-019-00704-x.

[81] J. D. Caldwell, I. Aharonovich, G. Cassabois, J. H. Edgar, B. Gil and D. N. Basov. Photonics with hexagonal boron nitride. *Nature Reviews Materials*, **4**, 8, 552 (2019). ISSN 20588437. doi: 10.1038/s41578-019-0124-1.

[82] M. Toth and I. Aharonovich. Single Photon Sources in Atomically Thin Materials. *Annual Review of Physical Chemistry*, **70**, 123 (2019). ISSN 0066426X. doi: 10.1146/annurev-physchem-042018-052628.

[83] T. T. Tran, K. Bray, M. J. Ford, M. Toth and I. Aharonovich. Quantum emission from hexagonal boron nitride monolayers. *Nature Nanotechnology*, **11**, 1, 37 (2016). ISSN 17483395. doi: 10.1038/nnano.2015.242.

[84] T. T. Tran, C. Elbadawi, D. Totonjian, C. J. Lobo, G. Grosso, H. Moon, D. R. Englund, M. J. Ford, I. Aharonovich and M. Toth. Robust multicolor single photon emission from point defects in hexagonal boron nitride. *ACS Nano*, **10**, 8, 7331–7338 (2016). ISSN 1936086X. doi: 10.1021/acsnano.6b03602.

[85] N. R. Jungwirth, B. Calderon, Y. Ji, M. G. Spencer, M. E. Flatté and G. D. Fuchs. Temperature Dependence of Wavelength Selectable Zero-Phonon Emission from Single Defects in Hexagonal Boron Nitride. *Nano Letters*, **16**, 10, 6052 (2016). ISSN 15306992. doi: 10.1021/acs.nanolett.6b01987.

[86] Z. Shotan, H. Jayakumar, C. R. Considine, M. Mackoit, H. Fedder, J. Wrachtrup, A. Alkauskas, M. W. Doherty, V. M. Menon and C. A. Meriles. Photoinduced Modification of Single-Photon Emitters in Hexagonal Boron Nitride. *ACS Photonics*, **3**, 12, 2490 (2016). ISSN 23304022. doi: 10.1021/acsphotonics.6b00736.

[87] M. Kianinia, S. Abbas, B. Regan, T. T. Tran and M. Ford. Robust Solid State Quantum System Operating at 800 K. *ACS Photonics*, **4**, 4, 768–773 (2017). ISSN 23304022. doi: 10.1021/acsphotonics.7b00086.

[88] T. Vogl, G. Campbell, B. C. Buchler, Y. Lu and P. K. Lam. Fabrication and Deterministic Transfer of High-Quality Quantum Emitters in Hexagonal Boron Nitride. *ACS Photonics*, **5**, 6, 2305 (2018). ISSN 23304022. doi: 10.1021/acsphotonics.8b00127.

[89] N. V. Proscia, Z. Shotan, H. Jayakumar, P. Reddy, M. Dollar, A. Alkauskas, M. Doherty, C. A. Meriles and V. M. Menon. Near-deterministic activation of room temperature quantum emitters in hexagonal boron nitride. *Optica*, **5**, 9 (2017). ISSN 23318422. doi: 10.1364/optica.5.001128.

[90] X. Li, G. D. Shepard, A. Cupo, N. Camporeale, K. Shayan, Y. Luo, V. Meunier and S. Strauf. Nonmagnetic Quantum Emitters in Boron Nitride with Ultranarrow and Sideband-Free Emission Spectra. *ACS Nano*, **11**, 7, 6652 (2017). ISSN 1936086X. doi: 10.1021/acsnano.7b00638.

[91] A. L. Exarhos, D. A. Hopper, R. R. Grote, A. Alkauskas and L. C. Bassett. Optical Signatures of Quantum Emitters in Suspended Hexagonal Boron Nitride. *ACS Nano*, **11**, 3, 3328 (2017). ISSN 1936086X. doi: 10.1021/acsnano.7b00665.

[92] M. Atatüre, D. Englund, N. Vamivakas, S. Y. Lee and J. Wrachtrup. Material platforms for spin-based photonic quantum technologies. *Nature Reviews Materials*, **3**, 5, 38 (2018). ISSN 20588437. doi: 10.1038/s41578-018-0008-9.

[93] W. B. Gao, A. Imamoglu, H. Bernien and R. Hanson. Coherent manipulation, measurement and entanglement of individual solid-state spins using optical fields. *Nature Photonics*, **9**, 6, 363 (2015). ISSN 17494893. doi: 10.1038/nphoton.2015.58.

[94] S. T. YIlmaz, P. Fallahi and A. Imamoğlu. Quantum-dot-Spin single-photon interface. *Physical Review Letters*, **105**, 3, 1 (2010). ISSN 00319007. doi: 10.1103/PhysRevLett.105.033601.

[95] N. Kalb, A. A. Reiserer, P. C. Humphreys, J. J. Bakermans, S. J. Kamerling, N. H. Nickerson, S. C. Benjamin, D. J. Twitchen, M. Markham and R. Hanson. Entanglement distillation between solid-state quantum network nodes. *Science*, **356**, 6341, 928 (2017). ISSN 10959203. doi: 10.1126/science.aan0070.

[96] H. J. Mamin, M. Kim, M. H. Sherwood, C. T. Rettner, K. Ohno, D. D. Awschalom and D. Rugar. Nanoscale Nuclear Magnetic Resonance with a Nitrogen-Vacancy Spin Sensor. *Science*, **339**, 6119, 557 (2013). ISSN 10959203. doi: 10.1126/science.1231540.

[97] N. Aslam, M. Pfender, P. Neumann, R. Reuter, A. Zappe, F. F. De Oliveira, A. Denisenko, H. Sumiya, S. Onoda, J. Isoya and J. Wrachtrup. Nanoscale nuclear magnetic resonance with chemical resolution. *Science*, **357**, 6346, 67 (2017). ISSN 10959203. doi: 10.1126/science.aam8697.

[98] M. W. Doherty, N. B. Manson, P. Delaney, F. Jelezko, J. Wrachtrup and L. C. Hollenberg. The nitrogen-vacancy colour centre in diamond. *Physics Reports*, **528**, 1, 1 (2013). ISSN 03701573. doi: 10.1016/j.physrep.2013.02.001.

[99] A. L. Exarhos, D. A. Hopper, R. N. Patel, M. W. Doherty and L. C. Bassett. Magnetic-field-dependent quantum emission in hexagonal boron nitride at room temperature. *Nature Communications*, **10**, 1, 1 (2019). ISSN 20411723. doi: 10.1038/s41467-018-08185-8.

[100] J. R. Toledo, D. B. De Jesus, M. Kianinia, A. S. Leal, C. Fantini, L. A. Cury, G. A. Sáfar, I. Aharonovich and K. Krambrock. Electron paramagnetic resonance signature of point defects in neutron-irradiated hexagonal boron nitride. *Physical Review B*, **98**, 15, 1 (2018). ISSN 24699969. doi: 10.1103/PhysRevB.98.155203.

[101] B. Huang, H. Xiang, J. Yu and S. H. Wei. Effective control of the charge and magnetic states of transition-metal atoms on single-layer boron nitride. *Physical Review Letters*, **108**, 20, 1 (2012). ISSN 00319007. doi: 10.1103/PhysRevLett.108.206802.

[102] L. Weston, D. Wickramaratne, M. Mackoit, A. Alkauskas and C. G. Van De Walle. Native point defects and impurities in hexagonal boron nitride. *Physical Review B*, **97**, 21, 1 (2018). ISSN 24699969. doi: 10.1103/PhysRevB.97.214104.

[103] J. Feng, H. Deschout, S. Caneva, S. Hofmann, I. Lončarić, P. Lazić and A. Radenovic. Imaging of Optically Active Defects with Nanometer Resolution. *Nano Letters*, **18**, 3, 1739 (2018). ISSN 15306992. doi: 10.1021/acs.nanolett.7b04819.

[104] A. Dietrich, M. Burk, E. S. Steiger, L. Antoniuk, T. T. Tran, M. Nguyen, I. Aharonovich, F. Jelezko and A. Kubanek. Narrowband quantum emitters over large spectral range with Fourier-limited linewidth in hexagonal boron nitride.

Physical Review B, **98**, 081414(R), 2 (2017). ISSN 24699969. doi: 10.1103/PhysRevB.98.081414.

[105] M. Abdi, M. J. Hwang, M. Aghtar and M. B. Plenio. Spin-Mechanical Scheme with Color Centers in Hexagonal Boron Nitride Membranes. *Physical Review Letters*, **119**, 23, 1 (2017). ISSN 10797114. doi: 10.1103/PhysRevLett.119.233602.

[106] P. K. Shandilya, J. E. Fröch, M. Mitchell, D. P. Lake, S. Kim, M. Toth, B. Behera, C. Healey, I. Aharonovich and P. E. Barclay. Hexagonal Boron Nitride Cavity Optomechanics. *Nano Letters* (2019). ISSN 15306992. doi: 10.1021/acs.nanolett.8b04956.

[107] M. Ye, H. Seo and G. Galli. Spin coherence in two-dimensional materials. *npj Computational Materials*, **5**, 1, 1 (2019). ISSN 20573960. doi: 10.1038/s41524-019-0182-3.

[108] K. S. Novoselov, A. Mishchenko, A. Carvalho and A. H. Castro Neto. 2D materials and van der Waals heterostructures. *Science*, **353**, 6298 (2016). ISSN 10959203. doi: 10.1126/science.aac9439.

[109] W. Ma, P. Alonso-González, S. Li, A. Y. Nikitin, J. Yuan, J. Martín-Sánchez, J. Taboada-Gutiérrez, I. Amenabar, P. Li, S. Vélez, C. Tollan, Z. Dai, Y. Zhang, S. Sriram, K. Kalantar-Zadeh, S. T. Lee, R. Hillenbrand and Q. Bao. In-plane anisotropic and ultra-low-loss polaritons in a natural van der Waals crystal. *Nature*, **562**, 7728, 557 (2018). ISSN 14764687. doi: 10.1038/s41586-018-0618-9.

[110] L. A. Jauregui, A. Y. Joe, K. Pistunova, D. S. Wild, A. A. High, Y. Zhou, G. Scuri, K. de Greve, A. Sushko, C. H. Yu, T. Taniguchi, K. Watanabe, D. J. Needleman, M. D. Lukin, H. Park and P. Kim. Electrical control of interlayer exciton dynamics in atomically thin heterostructures. *Science*, **366**, 6467, 870 (2019). ISSN 10959203. doi: 10.1126/science.aaw4194.

[111] C. Gong, L. Li, Z. Li, H. Ji, A. Stern, Y. Xia, T. Cao, W. Bao, C. Wang, Y. Wang, Z. Q. Qiu, R. J. Cava, S. G. Louie, J. Xia and X. Zhang. Discovery of intrinsic ferromagnetism in two-dimensional van der Waals crystals. *Nature*, **546**, 7657, 265 (2017). ISSN 14764687. doi: 10.1038/nature22060.

[112] B. Huang, G. Clark, E. Navarro-Moratalla, D. R. Klein, R. Cheng, K. L. Seyler, D. Zhong, E. Schmidgall, M. A. McGuire, D. H. Cobden, W. Yao, D. Xiao, P. Jarillo-Herrero and X. Xu. Layer-dependent ferromagnetism in a van der Waals crystal

down to the monolayer limit. *Nature*, **546**, 7657, 270 (2017). ISSN 14764687. doi: 10.1038/nature22391.

[113] H. Li, S. Ruan and Y. J. Zeng. Intrinsic Van Der Waals Magnetic Materials from Bulk to the 2D Limit: New Frontiers of Spintronics. *Advanced Materials*, **31**, 27, 1 (2019). ISSN 15214095. doi: 10.1002/adma.201900065.

[114] S. Liu, K. Yang, W. Liu, E. Zhang, Z. Li, X. Zhang, Z. Liao, W. Zhang, J. Sun, Y. Yang, H. Gao, C. Huang, L. Ai, P. K. J. Wong, A. T. S. Wee, A. T. N'Diaye, S. A. Morton, X. Kou, J. Zou, Y. Xu, H. Wu and F. Xiu. Two-dimensional ferromagnetic superlattices. *National Science Review*, **7**, 4, 745 (2020). ISSN 2053714X. doi: 10.1093/NSR/NWZ205.

[115] F. Jelezko, T. Gaebel, I. Popa, A. Gruber and J. Wrachtrup. Observation of Coherent Oscillations in a Single Electron Spin. *Physical Review Letters*, **92**, 7, 1 (2004). ISSN 10797114. doi: 10.1103/PhysRevLett.92.076401.

[116] B. C. Rose, D. Huang, Z. H. Zhang, P. Stevenson, A. M. Tyryshkin, S. Sangtawesin, S. Srinivasan, L. Loudin, M. L. Markham, A. M. Edmonds, D. J. Twitchen, S. A. Lyon and N. P. De Leon. Observation of an environmentally insensitive solid-state spin defect in diamond. *Science*, **361**, 6397, 60 (2018). ISSN 10959203. doi: 10.1126/science.aao0290.

[117] W. F. Koehl, B. B. Buckley, F. J. Heremans, G. Calusine and D. D. Awschalom. Room temperature coherent control of defect spin qubits in silicon carbide. *Nature*, **479**, 7371, 84 (2011). ISSN 00280836. doi: 10.1038/nature10562.

[118] R. Kolesov, K. Xia, R. Reuter, M. Jamali, R. Stöhr, T. Inal, P. Siyushev and J. Wrachtrup. Mapping Spin coherence of a single rare-earth ion in a crystal onto a single photon polarization state. *Physical Review Letters*, **111**, 12, 1 (2013). ISSN 00319007. doi: 10.1103/PhysRevLett.111.120502.

[119] J. M. Kindem, A. Ruskuc, J. G. Bartholomew, J. Rochman, Y. Q. Huan and A. Faraon. Control and single-shot readout of an ion embedded in a nanophotonic cavity. *Nature*, **580**, 7802, 201 (2020). ISSN 14764687. doi: 10.1038/s41586-020-2160-9.

[120] A. Jarmola, V. M. Acosta, K. Jensen, S. Chemerisov and D. Budker. Temperature- and magnetic-field-dependent longitudinal spin relaxation in nitrogen-vacancy ensembles in diamond. *Physical Review Letters*, **108**, 19, 1 (2012). ISSN 00319007. doi: 10.1103/PhysRevLett.108.197601.

[121] K. H. Michel and B. Verberck. Phonon dispersions and piezoelectricity in bulk and multilayers of hexagonal boron nitride. *Physical Review B - Condensed Matter and Materials Physics*, **83**, 11, 1 (2011). ISSN 10980121. doi: 10.1103/PhysRevB.83.115328.

[122] S. Jung, M. Park, J. Park, T. Y. Jeong, H. J. Kim, K. Watanabe, T. Taniguchi, D. H. Ha, C. Hwang and Y. S. Kim. Vibrational Properties of h-BN and h-BN-Graphene Heterostructures Probed by Inelastic Electron Tunneling Spectroscopy. *Scientific Reports*, **5**, September, 1 (2015). ISSN 20452322. doi: 10.1038/srep16642.

[123] A. Norambuena, E. Muñoz, H. T. Dinani, A. Jarmola, P. Maletinsky, D. Budker and J. R. Maze. Spin-lattice relaxation of individual solid-state spins. *Physical Review B*, **97**, 9, 1 (2018). ISSN 24699969. doi: 10.1103/PhysRevB.97.094304.

[124] E. L. Hahn. Spin echoes. *Physical Review*, **80**, 4, 580 (1950). ISSN 0031899X. doi: 10.1103/PhysRev.80.580.

[125] R. J. Blume. Electron spin relaxation times in sodium-ammonia solutions. *Physical Review*, **109**, 6, 1867 (1958). ISSN 0031899X. doi: 10.1103/PhysRev.109.1867.

[126] A. Ponti and A. Schweiger. Echo phenomena in electron paramagnetic resonance spectroscopy. *Applied Magnetic Resonance*, **7**, 2-3, 363 (1994). ISSN 09379347. doi: 10.1007/BF03162620.

[127] W. G. Breiland, H. C. Brenner and C. B. Harris. Coherence in multilevel systems. I. Coherence in excited states and its application to optically detected magnetic resonance in phosphorescent triplet states. *The Journal of Chemical Physics*, **62**, 9, 3458 (1975). ISSN 00219606. doi: 10.1063/1.430981.

[128] W. G. Breiland, C. B. Harris and A. Pines. Optically detected electron spin echoes and free precession in molecular excited states. *Physical Review Letters*, **30**, 5, 158 (1973). ISSN 00319007. doi: 10.1103/PhysRevLett.30.158.

[129] W. B. Mims. Envelope modulation in spin-echo experiments. *Physical Review B*, **5**, 7, 2409 (1972). ISSN 01631829. doi: 10.1103/PhysRevB.5.2409.

[130] V. Weis, K. Möbius and T. Prisner. Optically Detected Electron Spin Echo Envelope Modulation on a Photoexcited Triplet State in Zero Magnetic Field - A Comparison between the Zero-Field and High-Field Limits. *Journal of Magnetic Resonance*, **131**, 1, 17 (1998). ISSN 10907807. doi: 10.1006/jmre.1997.1340.

[131] L. P. Yang, C. Burk, M. Widmann, S. Y. Lee, J. Wrachtrup and N. Zhao. Electron spin decoherence in silicon carbide nuclear spin bath. *Physical Review B - Condensed Matter and Materials Physics*, **90**, 24, 1 (2014). ISSN 1550235X. doi: 10.1103/PhysRevB.90.241203.

[132] S. Takahashi, R. Hanson, J. Van Tol, M. S. Sherwin and D. D. Awschalom. Quenching spin decoherence in diamond through spin bath polarization. *Physical Review Letters*, **101**, 4, 1 (2008). ISSN 00319007. doi: 10.1103/PhysRevLett.101.047601.

[133] J. Song, J. Lee and M. Levenson. Picosecond relaxation measurements by polarization spectroscopy in condensed phases. *Physical Review A*, **17**, 4, 1439 (1978). ISSN 24699934. doi: 10.1103/PhysRevA.17.1439.

[134] S. Meiboom and D. Gill. Modified spin-echo method for measuring nuclear relaxation times. *Review of Scientific Instruments*, **29**, 8, 688 (1958). ISSN 00346748. doi: 10.1063/1.1716296.

[135] L. Childress, M. V. Gurudev Dutt, J. M. Taylor, A. S. Zibrov, F. Jelezko, J. Wrachtrup, P. R. Hemmer and M. D. Lukin. Coherent dynamics of coupled electron and nuclear spin qubits in diamond. *Science*, **314**, 5797, 281 (2006). ISSN 00368075. doi: 10.1126/science.1131871.

[136] G. S. Uhrig. Keeping a quantum bit alive by optimized π-pulse sequences. *Physical Review Letters*, **98**, 10, 7 (2007). ISSN 00319007. doi: 10.1103/PhysRevLett.98.100504.

[137] S. T. Ochsenbein and D. R. Gamelin. Quantum oscillations in magnetically doped colloidal nanocrystals. *Nature Nanotechnology*, **6**, 2, 112 (2011). ISSN 17483395. doi: 10.1038/nnano.2010.252.

[138] L. Rondin, J. P. Tetienne, T. Hingant, J. F. Roch, P. Maletinsky and V. Jacques. Magnetometry with nitrogen-vacancy defects in diamond. *Reports on Progress in Physics*, **77**, 5 (2014). ISSN 00344885. doi: 10.1088/0034-4885/77/5/056503.

[139] X. Lu, X. Chen, S. Dubey, Q. Yao, W. Li, X. Wang, Q. Xiong and A. Srivastava. Optical initialization of a single spin-valley in charged WSe_2 quantum dots. *Nature Nanotechnology*, **14**, 5, 426 (2019). ISSN 17483395. doi: 10.1038/s41565-019-0394-1.

[140] D. Riedel, F. Fuchs, H. Kraus, S. Väth, A. Sperlich, V. Dyakonov, A. A. Soltamova, P. G. Baranov, V. A. Ilyin and G. V. Astakhov. Resonant addressing and manipulation of silicon vacancy qubits in silicon carbide. *Physical Review Letters*, **109**, 22, 1 (2012). ISSN 00319007. doi: 10.1103/PhysRevLett.109.226402.

[141] M. W. Doherty, V. V. Struzhkin, D. A. Simpson, L. P. McGuinness, Y. Meng, A. Stacey, T. J. Karle, R. J. Hemley, N. B. Manson, L. C. Hollenberg and S. Prawer. Electronic properties and metrology applications of the diamond NV - Center under pressure. *Physical Review Letters*, **112**, 4, 1 (2014). ISSN 00319007. doi: 10.1103/PhysRevLett.112.047601.

[142] H. Kraus, V. A. Soltamov, F. Fuchs, D. Simin, A. Sperlich, P. G. Baranov, G. V. Astakhov and V. Dyakonov. Magnetic field and temperature sensing with atomic-scale spin defects in silicon carbide. *Scientific Reports*, **4**, 1 (2014). ISSN 20452322. doi: 10.1038/srep05303.

[143] F. Dolde, H. Fedder, M. W. Doherty, T. Nöbauer, F. Rempp, G. Balasubramanian, T. Wolf, F. Reinhard, L. C. Hollenberg, F. Jelezko and J. Wrachtrup. Electric-field sensing using single diamond spins. *Nature Physics*, **7**, 6, 459 (2011). ISSN 17452481. doi: 10.1038/nphys1969.

[144] W. Zhang, J. Zhang, J. Wang, F. Feng, S. Lin, L. Lou, W. Zhu and G. Wang. Depth-dependent decoherence caused by surface and external spins for NV centers in diamond. *Physical Review B*, **96**, 23, 1 (2017). ISSN 24699969. doi: 10.1103/PhysRevB.96.235443.

[145] M. Hoese, P. Reddy, A. Dietrich, M. K. Koch, K. G. Fehler, M. W. Doherty and A. Kubanek. Mechanical decoupling of quantum emitters in hexagonal boron nitride from low-energy phonon modes. *Science Advances*, **6**, 40, 1 (2020). ISSN 23752548. doi: 10.1126/sciadv.aba6038.

[146] N. Chejanovsky, A. Mukherjee, J. Geng, Y. C. Chen, Y. Kim, A. Denisenko, A. Finkler, T. Taniguchi, K. Watanabe, D. B. R. Dasari, P. Auburger, A. Gali, J. H. Smet and J. Wrachtrup. Single-spin resonance in a van der Waals embedded paramagnetic defect. *Nature Materials*, **20** (2021). ISSN 14764660. doi: 10.1038/s41563-021-00979-4.

[147] C. Bradac, S. F. Lim, H. C. Chang and I. Aharonovich. Optical Nanoscale Thermometry: From Fundamental Mechanisms to Emerging Practical Applications. *Advanced Optical Materials*, **8**, 15, 1 (2020). ISSN 21951071. doi: 10.1002/adom.202000183.

[148] X. D. Chen, C. H. Dong, F. W. Sun, C. L. Zou, J. M. Cui, Z. F. Han and G. C. Guo. Temperature dependent energy level shifts of nitrogen-vacancy centers in diamond. *Applied Physics Letters*, **99**, 16, 1 (2011). ISSN 00036951. doi: 10.1063/1.3652910.

[149] V. Ivády, T. Simon, J. R. Maze, I. A. Abrikosov and A. Gali. Pressure and temperature dependence of the zero-field splitting in the ground state of NV centers in diamond: A first-principles study. *Physical Review B - Condensed Matter and Materials Physics*, **90**, 23, 1 (2014). ISSN 1550235X. doi: 10.1103/PhysRevB.90.235205.

[150] A. Bosak, J. Serrano, M. Krisch, K. Watanabe, T. Taniguchi and H. Kanda. Elasticity of hexagonal boron nitride: Inelastic x-ray scattering measurements. *Physical Review B - Condensed Matter and Materials Physics*, **73**, 4, 1 (2006). ISSN 10980121. doi: 10.1103/PhysRevB.73.041402.

[151] R. W. Lynch and H. G. Drickamer. Effect of high pressure on the lattice parameters of diamond, graphite, and hexagonal boron nitride. *The Journal of Chemical Physics*, **44**, 1, 181 (1966). ISSN 00219606. doi: 10.1063/1.1726442.

[152] V. M. Acosta, E. Bauch, M. P. Ledbetter, C. Santori, K. M. Fu, P. E. Barclay, R. G. Beausoleil, H. Linget, J. F. Roch, F. Treussart, S. Chemerisov, W. Gawlik and D. Budker. Diamonds with a high density of nitrogen-vacancy centers for magnetometry applications. *Physical Review B - Condensed Matter and Materials Physics*, **80**, 11, 1 (2009). ISSN 1550235X. doi: 10.1103/PhysRevB.80.115202.

[153] K. Hayashi, Y. Matsuzaki, T. Taniguchi, T. Shimo-Oka, I. Nakamura, S. Onoda, T. Ohshima, H. Morishita, M. Fujiwara, S. Saito and N. Mizuochi. Optimization of Temperature Sensitivity Using the Optically Detected Magnetic-Resonance Spectrum of a Nitrogen-Vacancy Center Ensemble. *Physical Review Applied*, **10**, 3, 1 (2018). ISSN 23317019. doi: 10.1103/PhysRevApplied.10.034009.

[154] V. M. Acosta, E. Bauch, M. P. Ledbetter, A. Waxman, L. S. Bouchard and D. Budker. Temperature dependence of the nitrogen-vacancy magnetic resonance in diamond. *Physical Review Letters*, **104**, 7, 1 (2010). ISSN 00319007. doi: 10.1103/PhysRevLett.104.070801.

[155] M. W. Doherty, V. M. Acosta, A. Jarmola, M. S. Barson, N. B. Manson, D. Budker and L. C. Hollenberg. Temperature shifts of the resonances of the NV-center in diamond. *Physical Review B - Condensed Matter and Materials Physics*, **90**, 4, 1 (2014). ISSN 1550235X. doi: 10.1103/PhysRevB.90.041201.

[156] N. Zhang, H. Yuan, C. Zhang, L. Xu, J. Zhang, G. Bian, P. Fan, H. Yuan and J. Fang. Microwave Field Uniformity Impact on DC Magnetic Sensing with NV Ensembles in Diamond. *IEEE Sensors Journal*, **19**, 2, 451 (2019). ISSN 1530437X. doi: 10.1109/JSEN.2018.2878220.

[157] W. Liu, Z. P. Li, Y. Z. Yang, S. Yu, Y. Meng, Z. C. Li, N. J. Guo, F. F. Yan, Q. Li, J. F. Wang, J. S. Xu, Y. T. Wang, J. S. Tang, C. F. Li and G. C. Guo. Temperature-dependent energy-level shift of spins defects in hexagonal boron nitride. *ACS Photonics*, **8**, 7 (2021). ISSN 23304022. doi: 10.1021/acsphotonics.1c00320.

[158] O. R. Rubinas, V. V. Soshenko, S. V. Bolshedvorskii, A. I. Zeleneev, A. S. Galkin, S. A. Tarelkin, S. Y. Troschiev, V. V. Vorobyov, V. N. Sorokin, A. A. Sukhanov, V. G. Vins, A. N. Smolyaninov and A. V. Akimov. Optimization of the coherence properties of diamond samples with an intermediate concentration of NV centers. *Results in Physics*, **21**, 103845 (2021). ISSN 22113797. doi: 10.1016/j.rinp.2021.103845.

[159] X. Gao, B. Jiang, A. E. Llacsahuanga Allcca, K. Shen, M. A. Sadi, A. B. Solanki, P. Ju, Z. Xu, P. Upadhyaya, Y. P. Chen et al. High-contrast plasmonic-enhanced shallow spin defects in hexagonal boron nitride for quantum sensing. *Nano Letters*, **21**, 18, 7708 (2021). ISSN 15306992. doi: 10.1021/acs.nanolett.1c02495.

10 Appendix

10.1 List of Publications

1. A. Gottscholl, M. Kianinia, V. Soltamov, S. Orlinskii, G. Mamin, C. Bradac, C. Kasper, K. Krambrock, A. Sperlich, M. Toth, I. Aharonovich and V. Dyakonov. Initialization and read-out of intrinsic spin defects in a van der Waals Crystal at room temperature. *Nature Materials*, **19**, 5, 540 (2020).
   doi: 10.1038/s41563-020-0619-6.

2. A. Gottscholl, M. Diez, V. Soltamov, C. Kasper, A. Sperlich, M. Kianinia, C. Bradac, I. Aharonovich and V. Dyakonov. Room temperature coherent control of spin defects in hexagonal boron nitride. *Science Advances*, **7** (14), eabf3630 (2021).
   doi: 10.1126/sciadv.abf3630.

3. A. Gottscholl, M. Diez, V. Soltamov, C. Kasper, D. Krauße, A. Sperlich, M. Kianinia, C. Bradac, I. Aharonovich and V. Dyakonov. Spin defects in hBN as promising temperature, pressure and magnetic field quantum sensors. *Nature Communications*, **12**, 4480 (2021).
   doi: 10.1038/s41467-021-24725-1.
   (Awarded as featured article of the editors *Quantum Highlight* webpage)

4. A. Gottscholl, M. Wagenhöfer, M. Klimmer, S. Scherbel, C. Kasper, V. Baianov, G. V. Astakhov, V. Dyakonov, A. Sperlich. Superradiance of Spin Defects in Silicon Carbide for Maser Applications. *Frontiers in Photonics*, **3**, 886354 (2022).
   doi: 10.3389/fphot.2022.886354.

5. N. Mendelson, D. Chugh, J. R. Reimers, T. S. Cheng, A. Gottscholl, H. Long, C. J. Mellor, A. Zettl, V. Dyakonov, P. H. Beton, S. V. Novikov, C. Jagadish, H. H. Tan, M. J. Ford, M. Toth, C. Bradac and I. Aharonovich. Identifying carbon as the source of visible single photon emission from hexgonal boron nitride. *Nature Materials*, **20**, 321-328 (2021).
   doi: 10.1038/s41563-020-00850-y.

6. S. Weissenseel, A. Gottscholl, R. Bönnighausen, V. Dyakonov and A. Sperlich. Long-lived spin-polarized intermolecular exciplex states in thermally activated delayed fluorescence-based organic light-emitting diodes. *Science Advances*, **7**, eabj9961 (2021).
doi: 10.1126/sciadv.abj9961.

7. C. Kasper, D. Klenkert, Z. Shang, D. Simin, A. Gottscholl, A. Sperlich, H. Kraus, C. Schneider, S. Zhou, M. Trupke, W. Kada, T. Oshima, V. Dyakonov and G. V. Asthakhov. Influence of Irradiation on Defect Spin Coherence in Silicon Carbide. *Physical Review Applied*, **13** (4), 044054 (2021).
doi: 10.1103/PhysRevApplied.13.044054.

8. J. E. Fröch, L. P. Spencer, M. Kianinia, D. D. Totonjian, M. Nguyen, A. Gottscholl, V. Dyakonov, M. Toth, S. Kim, and I. Aharonovich. Coupling Spin Defects in Hexagonal Boron Nitride to Monolithic Bullseye Cavities. *Nano Letters*, **21** (15), 6549-6555 (2021).
doi: 10.1021/acs.nanolett.1c01843.

9. Y. Tieshan, N. Mendelson, C. Li, A. Gottscholl, J. Scott, M. Kianinia, V. Dyakonov, M. Toth, and I. Aharonovich. Spin defects in hexagonal boron nitride for strain sensing on nanopillar arrays. *Nanoscale*, **14** (13), 5239-5244 (2022).
doi: 10.1039/D1NR07919K.

10. F. F. Murzakhanov, G. V. Mamin, S. B. Orlinskii, U. Gerstmann, W. G. Schmidt, T. Biktagirov, I. Aharonovich, A. Gottscholl, A. Sperlich, V. Dyakonov, and V. A. Soltamov. Electron–Nuclear Coherent Coupling and Nuclear Spin Readout through Optically Polarized V_B^- Spin States in hBN. *Nano Letters*, **22** (7), 2718-2724 (2022).
doi: 10.1021/acs.nanolett.1c04610.

10.2 Danksagung

Zum Schluss will ich noch einer Vielzahl an Personen danken, die zum Gelingen der Arbeit beigetragen haben. Ein herzliches Dankeschön gilt:

- Prof. Dr. Vladimir Dyakonov, der mir die Arbeit überhaupt erst ermöglicht hat und meine Ergebnisse stets kritisch hinterfragte.
- PD habil. Dr. Andreas Sperlich, der bei Fragen immer ein offenes Ohr für mich hatte, vor allem wenn es um technische Problemstellungen ging.
- Prof. Dr. Igor Aharonovich für die großartige Kooperation insbesondere das Bereitstellen der hier verwendeten hBN Proben.
- Der gesamten Color Center Gruppe: allen voran Christian Kasper, der mir eine reibungslose Übernahme des ZfODMR Setups ermöglicht hat, Viktor Soltamov, der mich mit seinem theoretischen Wissen hinsichtlich Spin Hamiltonians und EPR unterstützte, meinen hBN Masteranden Matthias Diez und Dominik Krauße für die Unterstützung im Labor und außerdem meinen SiC Masteranden Selina Scherbel, Manuel Klimmer und Maximilian Wagenhöfer. Auch wenn ich diese Arbeit nur über meine hBN Projekte schrieb, so bin ich sehr stolz auf euch, dass wir letztendlich doch noch den Maser zum Laufen gebracht haben.
- André Thiem-Riebe und Valentin Baianov, die mir stets mit deren technischem Know-how zur Seite standen.
- Jeannine Grüne für die morgendlichen Gespräche beim ersten Kaffee.
- Meinen Bürokollegen Stefanie Dietz, Sebastian Weißenseel und Felix Brust: Steffi unter anderem für die entspannten Yogastunden (und höchst aufregende Rhönradstunde), Sebbo mitunter für die Hole Burning Diskussionen und vor allem Felix für die unvergesslichen Unterhaltungen rund um die Uhr.
- Meiner epischen WG bestehend aus Luisa, Lea und Fanny, die am Ende eines langen Arbeitstages für viel Abwechslung Zuhause sorgten und mich stets mit lauter kreativen Ideen überraschten.
- Meiner Calisthenics-Gruppe bestehend aus Simon, Christian, Lorenz, Den(n)is, Viktor und Gabriel, die mir den nötigen Ausgleich zum Labor-/Büroalltag boten.
- Meinen Freunden Dominik und Simon, die mein Leben schon seit meiner Kindheit prägen und mich dabei seit der Planung unseres ersten Mondspaziergangs von unserer Karton/Kissen-Rakete für die Physik begeistern konnten.
- Und zu guter Letzt meiner Familie: meinen Schwestern Stephanie, Magdalena und Veronika und vor allem meinen Eltern, die meine Leidenschaft zur Physik schon von klein auf förderten und denen ich einfach Alles zu verdanken habe.
  Vielen Dank!

Acknowledgement

This work was funded by the German Research Foundation DFG (DFG-AS 310/5-1, DFG-FOR 1809, DFG-DY 18/13-1), the ct.qmat Exzellenzcluster and the Bavarian state (Landesstelle).